

**RESEARCH  
IN  
APPLIED GEOPHYSICS**

**No. 33**

**1985**

**Development and Application of a  
Short-Baseline Electromagnetic  
Exploration Technique for  
the Ocean Floor**

**Peter A. Wolfgram**

**GEOPHYSICS LABORATORY  
DEPARTMENT OF PHYSICS  
UNIVERSITY OF TORONTO**

Development and Application  
of a  
Short Baseline Electromagnetic Exploration Technique  
for the  
Ocean Floor

by



Peter A.A. Wolfgram

Geophysics Laboratory  
Department of Physics  
University of Toronto.....

A thesis submitted in conformity with  
the requirements of the degree of  
Doctor of Philosophy  
in the University of Toronto

1985

# ABSTRACT

Hydrothermal springs on mid-oceanic ridge crests and on seamounts create polymetallic sulphide deposits that are thought to be models for many ancient ore-deposits now found on land. For the first time, possible subsurface extensions of these sulphide deposits and the properties of the upper few tens of meters seafloor basalt have been investigated with a geophysical method.

An electromagnetic technique has been developed to determine the electrical resistivity structure beneath the seafloor. A self-contained generator at the seafloor feeds a commutated electric current to two electrodes at either end of a vertical, long, insulated wire. The receiver is a remote induction coil magnetometer. Both instruments are self-contained and microprocessor-controlled, recording transmitted and received waveforms in random access memory. They are deployed from the ship to the seafloor where a deep submersible adjusts their separation to prearranged values at prearranged times. Both instruments are subsequently recovered and interrogated. The data are measurements of two horizontal components of the magnetic field as a function of transmitter-receiver horizontal separation and transmitter frequency.

The acronym MINI-MOSES was chosen for the method because - similar to the MOSES method previously developed but over smaller spatial dimensions - its geometry is carefully arranged to remove many of the adverse effects of the relatively conductive sea water. In particular, accurate estimates of sea floor resistivity are possible because the data are proportional to the transmitted current from the source into the crustal material.

A sea test of the method in 2.2 km deep water was conducted near an active hydrothermal sulphide zone on the Northern Juan de Fuca seafloor ridge. The survey results are consistent with 20  $\Omega$ m electrical resistivity or 12% porosity for the upper few tens of meters of basalt. Any sub-bottom metallic sulphide deposit at the site was found to be smaller than economic deposits on land. The technique should now be applied to a deposit located in an inactive hydrothermal area, or off the ridge-axis, or on a seamount. Detailed geological information from such a survey could provide a better understanding of many ancient deposits found on land.

## ACKNOWLEDGMENTS

The first place in this list of acknowledgments is due to my wife Renate who kept up spirits through too many evenings when I was working late. Alone in a foreign country without relatives she went through weeks of caring for our newborn daughter Christine while I was 3000 km away on yet another seafloor-experiment. I cannot thank her enough for all the support that she gave to me during these difficult years.

My supervisor Dr. R. Nigel Edwards provided additional financial support that helped to compensate for my special situation as a married foreign student and he carefully guided my research work into the right direction. Dr. G.F. West and Dr. Edwards were always there to help with problems along the way.

During the development of the instrumentation Dr. G.F. West explained to me design and debugging of the important circuitry and Jeremy B.G. Hughes, Rejan Desbiens and Dr. Edwards helped me to build it. Norman Sanford and his crew of the Physics Department Electronics Workshop produced the computer module and the software to Dr. Edwards' and my specifications. Precisely machined computer boxes for the packages and the hardware required for the pressure tests

are products of the Physics Department Machine Shop. The MOSES group (Dr. R.N. Edwards, Dr. L.K. Law, Dr. D.C. Nobes, M.N. Bone and myself) gratefully acknowledges the pressure tests run at the Defense Research Establishment Atlantic in Dartmouth, Nova Scotia.

Many suggestions were made by Dr. Lawrie K. Law. He, Mike N. Bone and Don Bowker managed most of the organization and the "real" work during all sea experiments. I thank Dr. David C. Nobes for useful hints and for reprogramming "his" ocean bottom magnetometers for the early OBT-test surveys.

The able seamanship, hospitality and tremendous support from Captain R.W. MacKenzie and crew of the CCS Vector during earlier experiments, from Captain P. Howland and crew of the USS Atlantis II, and Captain K. Palfry and crew of the USS Wecoma during the MINI-MOSES experiment are gratefully remembered by all of the MOSES group. Chief pilot Dudley Foster and pilot Skip Glesson of the ALVIN made helpful suggestions for the preparation of the experiment and then perfectly mastered a difficult new kind of ocean bottom operation. Dr. Margaret Leinen and Dr. Ross McDuff allowed us big fractions of their bottom time in ALVIN when they ably conducted our experiment. Dr. John R. Delaney and Dr. Paul Johnson, co-chief scientists on that Atlantis II cruise, and Dr. Jill Karsten showed great interest in our

experiment and provided preliminaray cruise reports, a preliminary geological map, location maps and slides from the bottom photography.

Greg Stopelli from the University of Toronto Computing Service Microcomputer Group was very helpful in transferring the survey data from a floppy disk through a complicated computer network into my directory in the Department of Physics VAX 11 - VMS network where all the data processing was performed. All of the xy-type graphs were produced with David Boerner's very efficient interactive TPLLOT package. Stephen Cheesman assisted in modifying and running his thin plate modeling program for the MINI-MOSES configuration.

Many discussions with my fellow-students, in particular Scott Holladay and Ben Polzer, helped to clear up difficult problems along the way.

Dr. P. Weidelt spent many hours during my short visits to lead me in the right direction for the development of an integral equation technique for two-dimensional electromagnetic modeling.

Helen Rousso typed this thesis and all its equations with incredible speed and accuracy into a VAX 11-file using the MASS 11 word processing software.

Since the start of my Ph.D. program I have received financial support from (in chronological order): Deutscher Akademischer Austauschdienst (DAAD, West German Government), Gertrud Davies Fellowship (University College, University of Toronto), Imperial Oil of Canada Research Grant to Dr. R.N. Edwards, University of Toronto Open Fellowship, World University Service of Canada (WUSC, Canadian Department of External Affairs).



## CONTENTS

|   |    |
|---|----|
| Abstract  | 2  |
| Acknowledgments   | 4  |
| Table of contents   | 8  |
| <br>  |    |
| 1. Introduction   | 10 |
| 1.1 The targets   | 12 |
| 1.2 Possible geophysical techniques                                     | 14 |
| 1.3 The vertical source method  | 18 |
| 1.4 Outline of this thesis  | 22 |
| <br>  |    |
| 2. Theory   | 24 |
| 2.1 The alternating vertical electric bipole<br>over a layered seafloor | 25 |
| 2.2 The effect of an inclined source-bipole                             | 37 |
| 2.3 Induced polarization and two-dimensional<br>effects                 | 44 |
| <br>  |    |
| 3. Instrumentation  | 46 |
| 3.1 The ocean bottom transmitter (OBT)                                  | 48 |
| 3.2 The ocean bottom induction coil<br>magnetometer (OBC)               | 60 |
| 3.2.1 Inductance and sensitivity of the<br>sensor coils                 | 62 |
| 3.2.2 Calibration of the OBC  | 71 |

|       |  |      |
|-------|--|------|
| 3.3   | Signal to noise ratio  | 81   |
| 4.    | Survey and results   | 92   |
| 4.1   | Geological setting   | 93   |
| 4.2   | Experimental procedure   | 97   |
| 4.3   | Data processing  | 104  |
| 4.4   | Results and interpretation   | 119  |
| 5.    | Conclusions and suggestions for future work  | 132  |
| 5.1   | Summary  | 132  |
| 5.2   | Suggestions for future work  | 135  |
| 5.2.1 | Theory   | 135  |
| 5.2.2 | Instrumentation  | 136  |
| 5.2.3 | Surveys  | 138  |
| 6.    | References   | 140  |
|       | Appendices:  | 146  |
| A     | Fourier transform and power spectrum   | A-1  |
| B     | An integral equation technique for simulating<br>electromagnetic induction in two dimensions | B-1  |
| B.1   | Vector integral equation for the electric<br>field   | B-1  |
| B.2   | The elements of the Green dyadic   | B-5  |
| B.3   | Electric and magnetic field  | B-15 |

## 1. INTRODUCTION

Most of the world's copper and zinc resources are contained in metallic sulphide deposits. A large portion of them have been attributed to magmatic-hydrothermal processes at mid-oceanic spreading centers and subducting plate boundaries (figure 1-1). The Kuroko ores of Japan and the pyritic ores of Cyprus have long been explained with submarine volcanism (Peters, 1978, chapter 4; Lydon, 1984). The advent of the deep ocean submersible has led to the chance discovery of a number of polymetallic sulphide deposits in the vicinity of hydrothermal venting (figure 1-2) on the ocean floor (CYAMEX, 1979; RISE, 1980; Hekinian, 1984). The sizes of individual deposits are largely unknown, although one estimate by Malahoff (1982) ranged up to several million tons - the typical size of Cyprus orebodies. The seafloor deposits might not become economic for many decades, but a study of them might well provide the geologist with a better understanding of the mineralogy (Oudin et al., 1981), the depositional environment (RISE, 1981), and the causative hydrothermal processes (Cathles, 1980; Strens and Cann, 1982) of ancient deposits now located on land.

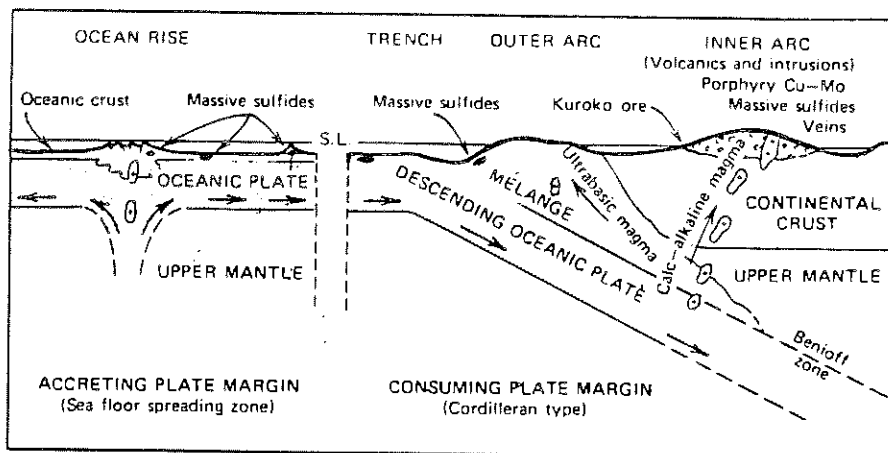
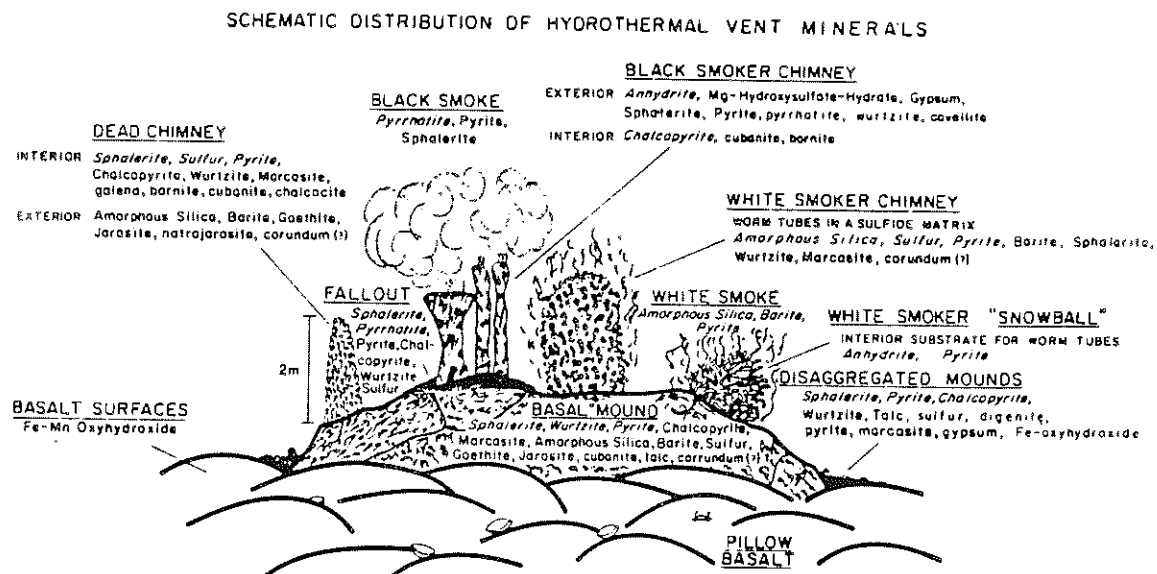


**Figure 1-1:** Plate tectonic setting of base-metal deposits (from Peters, 1978, p.124).



A composite sketch illustrating the variety of structures observed at the different RISE vent sites and the mineral distributions associated with these structures. Note that anhydrite and Mg-hydroxysulfate-hydrate are found only in active, black smokers, and pyrrhotite occurs mainly in black smoke or in black fallout sediment. Note also that Mn-oxyhydroxides precipitate on basalt surfaces slightly away from vents. Main phases are italicized; minor phases are capitalized; accessory phases are printed in lower case.

**Figure 1-2:** from Haymon and Kastner (1981).

## 1.1 THE TARGETS

Polymetallic sulphide deposits at the centers of mid-oceanic ridge crests measure up to tens of meters across their surface (Hekinian et al., 1980) whereas those located in the marginal fault system (Malahoff, 1982) and on seamounts (Hekinian, 1984) may be up to hundreds of meters in size. High temperature hydrothermal leaching of seafloor basalts (Mottl and Holland, 1978; Mottl et al., 1979) provides the building material for the sulphide deposits. Major constituents are the non-magnetic minerals pyrite ( $\text{FeS}_2$ ), sphalerite ( $\text{ZnS}$ ) and chalcopyrite ( $\text{CuFeS}_2$ ) with very little of the magnetic pyrrhothite present (Haymon and Kastner, 1981). The densities of these minerals range from 3.5 to 5.2  $\text{g/cm}^3$  (Telford et al., 1976, table 2.6). Pyrite and chalcopyrite from land deposits are good electrical conductors averaging 0.3  $\Omega\text{m}$  and 0.004  $\Omega\text{m}$ , respectively, whereas sphalerite is relatively resistive with an average of 100  $\Omega\text{m}$  (Telford et al., 1976, table 5.2).

The bulk resistivity depends on the texture of the deposit as well as on the relative abundances of the conductive minerals. In particular, seawater with 0.31  $\Omega\text{m}$  (Bullard and Parker, 1970) filling the interstitial space may modify the bulk electrical parameters. The electrical resistivity of the hydrothermal fluids filling the pores in

the sulphide deposits might be reduced by an order of magnitude due to temperatures of up to 420°C. An increased salinity may further decrease the electrical resistivity. The porosity of samples from active vents was visually estimated to 10-30% whereas inactive vents would lie around 5-15% and older deposits tend to seal off with an oxide crust (J.M. Franklin, private communication). Crawford et al. (1984) estimated 25-50% in situ fluid content for polymetallic sulphides on the East Pacific Rise at 21°N.

The deposits are embedded in seawater-saturated basalts. Drillhole results (Hyndman et al., 1983) indicate densities around 2.8 g/cm<sup>3</sup>, porosities around 12 % and electrical resistivities of tens of ohm-meters below the top few hundred meters of geologically young seafloor basalts. (No reliable information exists for shallower depth because of the drillhole casings.)

The depth extent and shape of the seafloor deposits is unknown. Their composition has been inferred from surface samples, but it may be different at depth because of the different depositional environment (Rona, 1976; Hekinian et al., 1980). The lateral (and depth) variations in basalt effective porosity ("water/rock mass ratio", Seyfried and Mottl, 1982) which set the conditions for the hydrothermal alteration, are largely unknown.

## 1.2 POSSIBLE GEOPHYSICAL TECHNIQUES

Geophysical techniques can provide information on changes in physical parameters at depth. Gravity measurements (RISE, 1980) have been used to delineate the magma chamber that drives the hydrothermal circulation and they could be used to investigate the sulphide deposits, which are probably denser than their host rocks. Small deposits will certainly be overlooked because the associated gravity anomaly would be small. Further, levelling on the seafloor within a submersible is a difficult procedure and severely limits the accuracy of gravity measurements (RISE, 1980). Magnetic field measurements might delineate the extent of the hydrothermal alteration zone through the associated decrease in magnetization (Dr. Paul Johnson, private communication). They do not seem generally suitable for investigating sulphide deposits because these contain little magnetic minerals. Electromagnetic methods, on the other hand, respond to bulk electrical resistivity, which in turn is determined by the concentration and composition of the sulphides and by the water content or porosity of the basalts. The resistivity contrast between sulphides and the host basalts is presumably high so that the subsurface extensions of the deposits may be outlined. Therefore, as on land, electromagnetic methods seem to be the most promising techniques for investigating depth extent, shape,

and composition of the polymetallic sulphide deposits and also the porosity of the basalts that host the deposits.

The sulphide targets are relatively small (tens to hundreds of meters) compared to the water depth (2000 m). The instrumentation thus must be located on the seafloor because surface methods cannot resolve features located at distances 10 to 100 times the target dimensions.

Electromagnetic seafloor methods use ionospheric magnetic field variations below a few cycles per hour as sources (Cox, 1981). They have been used to investigate the electrical conductivity of oceanic lithosphere down to hundreds of kilometers (e.g. reviewed by Cox, 1981; Law, 1984). An electromagnetic method for the much shallower sulphide targets requires higher frequencies. The seafloor at mid-oceanic ridge-crests is shielded from frequencies above about 10 cycles per hour by at least 2 km of conductive seawater. This excludes the use of passive frequency-sounding methods for the sulphide targets while on the other hand providing a very low noise environment for active source methods. Apart from narrow-band hydrodynamically-generated fields limited to a few processes, the ambient noise level is at the nV/m (electric field) or pT (magnetic induction) level (Chave and Cox, 1982).



Inductive sources that generally require large loops pose logistic problems whereas grounded electrical sources are favoured by low resistance coupling to the conductive seawater.

Conventional electrical techniques on land normally use horizontal electric bipoles to transmit electric current into the ground and pairs of non polarizing electrodes to measure electric fields in the vicinity. Young and Cox (1981) demonstrated their feasibility for measuring seafloor conductivity. Francis (in press) very recently used the French deep submersible CYANA to deploy a Wenner-array on the seafloor in order to measure the resistivity of both sulphides and basalts. The voltage measured in his configuration is

$$U = \frac{I}{2\pi d} \left[ \frac{1}{\rho_1} + \frac{1}{\rho_0} \right]^{-1} \quad (1)$$

where  $I$  is the transmitted current,  $d$  is the Wenner spacing,  $\rho_0$  is the water resistivity and  $\rho_1$  is the seafloor resistivity. The dashed line in figure 1-3 shows that very conductive sulphides on the seafloor would be well resolved. It also shows that this measurement becomes insensitive to the seafloor resistivity if the latter increases much beyond the water resistivity. Another disadvantage is that the rugged topography in the vicinity

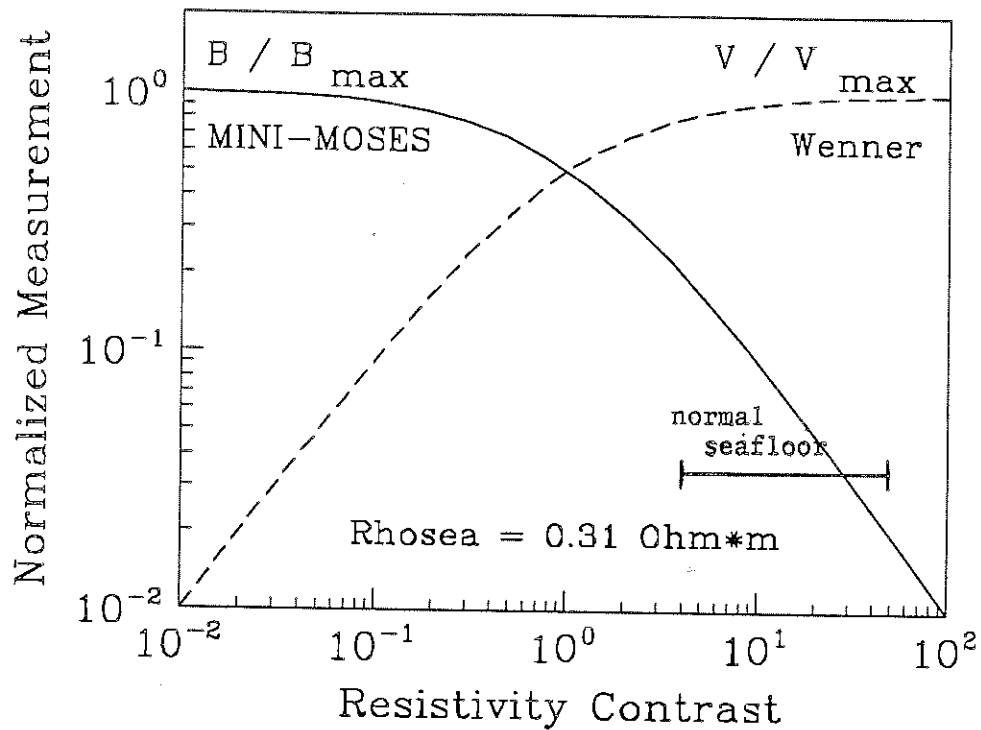


Figure 1-3: Comparison between the MINI-MOSES technique and the Wenner electrical sounding. The measurements are magnetic induction and electric voltage, respectively, for fixed geometry. They are plotted versus the seafloor resistivity normalized with the sea water resistivity ("resistivity contrast"). The Wenner sounding becomes insensitive to seafloor resistivity if the latter is large compared to the seawater resistivity whereas MINI-MOSES cannot resolve very small seafloor resistivities.

of the sulphide deposits will seriously distort the measured electric field.

### 1.3 THE VERTICAL SOURCE METHOD

A vertical electric bipole on the seafloor, transmitting current into the seafloor, produces the azimuthal magnetic field (see chapter 2):

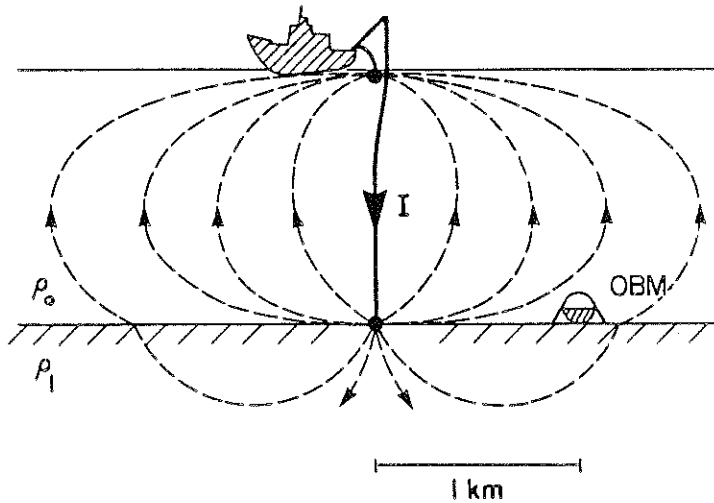
$$H_{\phi} = \frac{I}{2\pi r} \left( \frac{a}{\sqrt{r^2+a^2}} - \frac{b}{\sqrt{r^2+b^2}} \right) \rho_0 \left[ \rho_1 + \rho_0 \right]^{-1} \quad (2)$$

where  $r, a, b$  define the geometry and  $I, \rho_0$  and  $\rho_1$  are as in (1). The solid line in figure 1-3 shows that this measurement  $H_{\phi}$  becomes very sensitive to the seafloor resistivity if the latter is higher than the water resistivity. It also shows that the conductivity of extremely conductive sulphides would not be well resolved. Topographic effects should be small because the measured magnetic field is an integral quantity that depends on a volume of current density underneath the receiver.

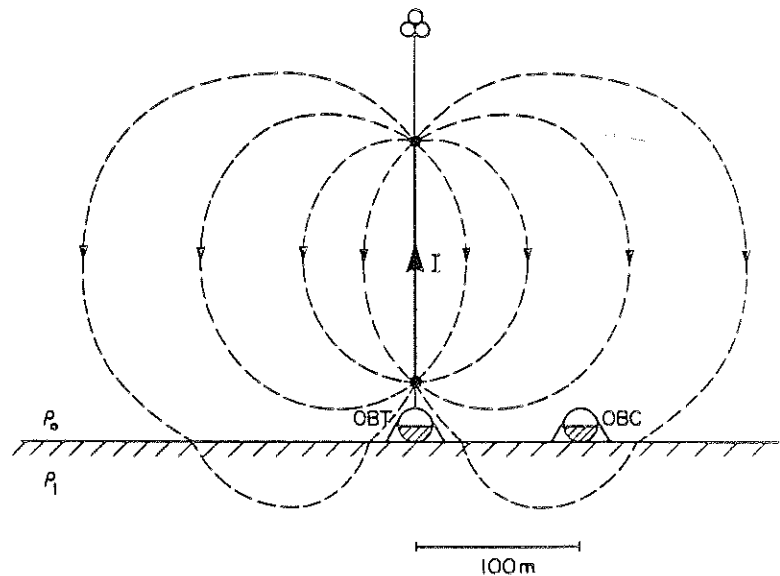
A combination of horizontal electric sounding and the vertical source / horizontal magnetic field measurement

would obviously be the most comprehensive approach. The horizontal electric sounding is feasible as Francis (in press) has shown. I attempt to show in this thesis the feasibility of the vertical bipole technique for seafloor sulphide exploration.

The vertical electric bipole method - proposed by Edwards et al. (1981) and tested by Nobes (1984) and by Edwards et al. (1985) - has been assigned the acronym MOSES for magnetometric off-shore electrical sounding. It is schematized in figure 1-4a. An electric current  $I$  generated on the ship is fed into an insulated wire with grounding electrodes at the sea surface and at the seafloor. The remote high-sensitivity ocean bottom magnetometer (OBM) measures the azimuthal magnetic field at a distance  $r$  from the source bipole. This magnetic field is proportional to the net electric current that passes into the seafloor through the circular area  $\pi r^2$  centered around the source bipole. Although very sensitive to the seafloor resistivity, the magnetic field is rather small (nanotesla level) which led Nobes (1984) and Edwards et al. (1985) to use newly developed high-sensitivity flux-gate magnetometers for their tests of the vertical source method. An inexpensive practical alternative at the higher frequencies used in this experiment, is the induction coil, the sensitivity of which is only limited by weight and volume.



MOSES



MINI - MOSES

**Figure 1-4:** a) upper: in the MOSES method a shipboard transmitter drives a current  $I$  into two electrodes at the end of an insulated vertical wire. Some of the current enters the lower medium and returns around the ocean bottom magnetometer (OBM) to produce a magnetic field proportional to the resistivity contrast  $\rho_1/\rho_0$ . b) lower: the MINI-MOSES instrumentation operates on a much smaller baseline with a remote low-power transmitter (OBT), its vertical bipole held upright with deep-sea floats, and with an induction coil magnetometer (OBC) as receiver.

Because of the low resistance coupling between electrodes and seawater, a low-power (battery-operated) electric current generator could feed several Amperes into a wire tens to hundreds of meters long. The magnetic induction produced by such a vertical bipole on the seafloor (similar to the MOSES bipole) can be estimated from eq.(2). For resistivity  $20 \Omega\text{m}$ , current 5 A, and bipole-length 100 m, the magnetic induction is 1 nT at 10 m distance from the bipole and 10 pT at 400 m. Resistivity information is obtained down to depths of about half the distance between bipole and receiver. It follows that the sulphide targets require picotesla sensitivity for magnetic induction measurements.

I attempt to prove in this thesis that a "MINI-MOSES" technique (figure 1-4b) is a feasible solution to the exploration problem outlined above. Transmitter-receiver separations would be on the order of the target size and therefore small compared to the MOSES technique. MINI-MOSES would feature a remote battery-powered ocean bottom transmitter (OBT) with its vertical electric bipole held upright by deep-sea floats. The magnetic field would be measured by an induction coil magnetometer (OBC). Both instruments need to be microprocessor-controlled so that they can operate remotely with enough flexibility for short-term survey planning. The transmitter and receiver would be

programmed onboard the ship and then deployed to the seafloor where a deep submersible adjusts their positions to prearranged distances at prearranged times. The instruments would be subsequently retrieved and the data recovered. The measurements of the magnetic field so obtained as a function of transmitter-receiver separation and transmitter frequency could then be inverted in terms of the distribution of the electrical resistivity below the seafloor.

#### 1.4 OUTLINE OF THIS THESIS

Chapter 2 of this thesis explains the principle of the method and provides the equations used in the data inversion. In section 2.1, the magnetic induction is derived that would be measured at some distance from an oscillating vertical electric bipole on the seafloor. The effect on the measurements of lifting the lower electrode off the seafloor will be estimated as well as how the sensitivity of the MINI-MOSES method to subsurface resistivity varies with depth below the seafloor. A non-vertical source bipole could distort the measurements - but the effects can be estimated as shown in section 2.2. An outlook into future theoretical developments in section 2.3 concludes this chapter.

The development of the instrumentation (chapter 3) comprised a major part of the research project. The ocean bottom transmitter (section 3.1) is unique in its design and application and much can be learned for future instruments of this kind. The square-cored induction coil magnetometer (section 3.2) offers advantages that reach beyond the application in the MINI-MOSES experiment.

Chapter 4 contains the test survey and its results. Logistic problems - quite different from those encountered in land geophysical surveys - had to be solved (section 4.2). The data processing (section 4.3) served to generate apparent resistivity and phase spectra for each transmitter-receiver separation. The inversion of the processed data in terms of seafloor electrical resistivity distribution and the subsequent interpretation reveal the limitations of a very small data set (section 4.4) but, on the other hand, also show the power of this method.

The summary in chapter 5 is followed by a list of the various lessons that we have learned from this effort that can be applied in future ventures.



## 2. THEORY

The magnetic field that would be measured with the MINI-MOSES technique over certain earth models can be predicted and compared to actual measurements. Section 2.1 deals with this practical aspect of theoretical solutions as well as with the better understanding of the method that they can provide. The effects on the measurement of lifting the lower electrode off the seafloor are estimated. The section concludes with a description of an existing automating inversion technique. In section 2.2 the effects of an inclined source-wire are presented and section 2.3 contains an outlook into future theoretical developments.

Edwards et al. (1981) derived the full electromagnetic solution for the MOSES configuration over a conducting seafloor halfspace and showed the effects of intermediate conductive and resistive layers. Their results were extended by Nobes (1984) to the horizontally isotropic case that can be described by a horizontal resistivity and a vertical resistivity. The measured resistivity of a lower halfspace of assumed uniform resistivity - calculated from measurements over an unknown lower medium - is known as "apparent resistivity"  $\rho_a$ . An approximate expression for the  $\rho_a$  was derived under the conditions that the transmitter-receiver separation is large compared with the

ocean depth (= bipole length) but small enough for the inductive losses in the lower halfspace to be negligible.

The water layer is very thick compared to the typical length scales of MINI-MOSES and can be treated as an upper conductive halfspace. This simplifies the theoretical treatment, in particular permitting an exact expression for the apparent resistivity.

## 2.1 THE ALTERNATING VERTICAL ELECTRIC BIPOLE OVER A LAYERED SEAFLOOR

For the following derivations, a cylindrical coordinate system  $(r, \phi, z)$  as in figure 2-1, and a harmonic time variation are assumed:

$$\underline{B}(\underline{r}, t) := \text{Re} \left( \underline{B}(r, \phi, z) e^{i\omega t} \right)$$

As a consequence of the radial symmetry of the problem only the tangential magnetic (TM) mode is excited by a vertical electric dipole (Chave, 1982). As a consequence, its magnetic induction can be represented by the vertical component  $\Pi$  of the magnetic Hertz vector:

$$\underline{B}(r, \phi, z) = \underline{\nabla} \times \left( \sigma \Pi \hat{z} \right) = - \frac{\partial(\sigma \Pi)}{\partial r} \hat{\phi} := B(r, z) \hat{\phi}$$

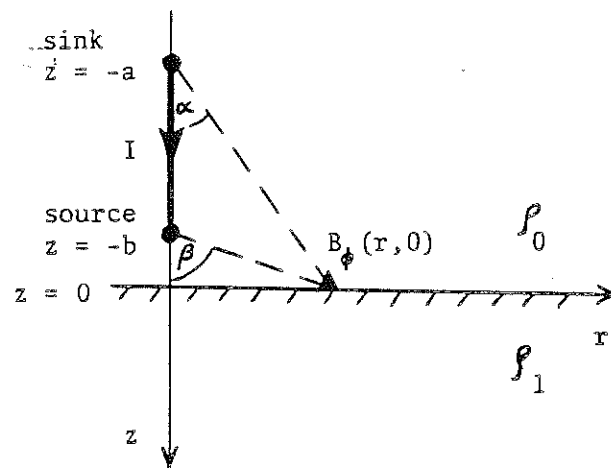


Figure 2-1: The geometry for the simulation of the time varying magnetic induction  $B$ .

where, in an unbounded medium,

$$\sigma\Pi = \mu_0 Idz' \frac{e^{-\alpha R}}{4\pi R}.$$

$R = [r^2 + (z-z')^2]^{1/2}$  is the distance between dipole and field point,  $(0,0,z')$  is the location of the dipole,  $Idz'$  is the electric dipole moment, and  $\alpha^2 = i\omega\mu_0\sigma$  is the propagation constant. Substituting  $\sigma\Pi$  into the expression for  $B$  results in

$$B(r,z) = - \frac{\partial(\sigma\Pi)}{\partial r} = \frac{\mu_0 Idz'}{4\pi} \frac{re^{-\alpha R}}{R^3} (\alpha R + 1).$$

On using Sommerfeld's integral and the relations between the Bessel functions  $J_0$  and  $J_1$ ,

$$B(r,z) = \frac{\mu_0 Idz'}{4\pi} \int_0^\infty \frac{\lambda}{\Theta} e^{-\Theta|z-z'|} J_1(\lambda r) \lambda d\lambda$$

where  $\Theta^2 = \alpha^2 + \lambda^2$ . After defining a Hankel-transform pair identical to the one in Edwards et al. (1981) the dipole field in wave number domain is

$$B(\lambda,z) = \frac{\mu_0 Idz'}{4\pi} \frac{\lambda}{\Theta} e^{-\Theta|z-z'|}.$$

This is a particular solution to the (Hankel-transformed) magnetic field Helmholtz equation that governs the behaviour of  $B$  in a conducting medium. Edwards et al. (1981) showed how the Hankel-transformed Helmholtz equation leads to

$$\frac{d^2 B}{dz^2} = \Theta^2 B \quad (1)$$

with the general solution composed of upward and downward diffusing exponentials.

I will now first derive the solution for the case of a single boundary - the seafloor - and discuss it. Afterwards I will present a more complicated model (layer over halfspace).

The radiation conditions for large positive and negative  $z$ , and the continuity of  $B$  and  $E_r = (\rho/\mu_0)dB/dz$  at  $z=0$  allow the calculation of the coefficients for the general solution in each halfspace resulting in the oceanic ( $z \leq 0$ ) dipole field:

$$B(\lambda, z) = \frac{\mu_0 I dz'}{4\pi} \left( e^{-\Theta_0 |z-z'|} - K_{01} e^{\Theta_0 (z-z')} \right) \frac{\lambda}{\Theta_0} \quad (2)$$

and the dipole field in the crustal halfspace ( $z \geq 0$ ):

$$B(\lambda, z) = \frac{\mu_0 I dz'}{4\pi} (1 - K_{01}) e^{-\Theta_0 (z-z')} \frac{\lambda}{\Theta_0} \quad (3)$$

where  $K_{ij} = (\rho_j \Theta_j - \rho_i \Theta_i) / (\rho_j \Theta_j + \rho_i \Theta_i)$  is the impedance reflection coefficient and subscript 0 denotes ocean, 1 denotes crust. The field at the seafloor ( $z=0$ ) integrated along a finite vertical source wire from a sink at  $z=-a$  to a source at  $z=-b$  is then

$$B(r) = \frac{\mu_0 I}{4\pi} \int_0^\infty (1 - K_{01}) \left( e^{-\Theta_0 b} - e^{-\Theta_0 a} \right) \frac{\lambda}{\Theta_0^2} J_1(\lambda r) \lambda d\lambda \quad (4)$$

where a and b are the grounding points as shown in figure 2-1. For the dc-case (zero frequency)  $\alpha=0$ ,  $\theta^2=\lambda^2$ , and  $K_{01}=(\rho_1-\rho_0)/(\rho_1+\rho_0)$  is the resistivity reflection coefficient. Then the inverse Hankel transform results in the closed expression:

$$B(r) = \frac{\mu_0 I}{4\pi r} (1-K_{01}) \left( \frac{a}{\sqrt{r^2+a^2}} - \frac{b}{\sqrt{r^2+b^2}} \right) . \quad (5)$$

This is the magnetic induction that would be measured with the MINI-MOSES technique as a function of transmitter-receiver separation  $r$  over a seafloor halfspace.

I will now take a closer look at this expression. After replacing  $B=\mu_0 H$  and  $a/(r^2+a^2)^{1/2}=\cos(\alpha)$  equation (5) becomes

$$H_\phi = \frac{I}{4\pi r} (\cos \alpha - \cos \beta) - \frac{K_{01} I}{4\pi r} (\cos \alpha - \cos \beta) .$$

The first term is the integral of Biot-Savart's law along the wire. The second term represents the field due to the current flow in the medium. It is proportional to  $K_{01}$  and therefore vanishes in the absence of any boundary: the current density of a point source or sink in an unbounded medium produces no magnetic field because otherwise  $\nabla \cdot \underline{J} = \nabla \cdot (\nabla \times \underline{H}) = 0$ . Taken together, the two terms can be rewritten so that equation (5) takes the form of Ampere's circuital law. Then, the right-hand side represents the net

current that crosses the circular area  $A=\pi r^2$  on the seafloor, centered around the origin (i.e. around the source-bipole):

$$2\pi r H_{\phi} = \frac{\Omega_{\alpha}}{4\pi} (1-K_{01})(-I) + \frac{\Omega_{\beta}}{4\pi} (1-K_{01})I$$

where  $\Omega_{\alpha}=2\pi(1-\cos\alpha)$  is the solid angle subtended by the current sink and the circular area A.  $\Omega_{\alpha}/4\pi$  is then the factor by which the current density is reduced due to the geometrical thinning away from the sink point. The measured magnetic field is zero for an insulating seafloor and a maximum for a perfectly conducting seafloor because it depends on the transmission coefficient  $(1-K_{01})$ . This makes the method very sensitive to the seafloor resistivity as has been pointed out by Edwards et al. (1981). It is also the principal feature that distinguishes vertical and horizontal source methods. The following analogy to electronic circuits should clarify this. I have calculated (and plotted in the introduction, figure 1-3) normalized measurements for each method: The (normalized) magnetic field of the MINI-MOSES technique

$$\frac{B}{B_{\max}} \propto \frac{1}{\rho_1 + \rho_0}$$

"sees" two resistors in series and is therefore sensitive to changes in the higher resistance. The (normalized) electric field of the Wenner array

$$\frac{U}{U_{\max}} \propto \frac{1}{1/\rho_1 + 1/\rho_0}$$

"sees" two resistors in parallel and is therefore sensitive to changes in the lower resistance.

An apparent resistivity formula follows directly from equation (5):

$$\frac{\rho_a}{\rho_0} = \frac{\mu_0 I}{2\pi r B} \left( \frac{a}{\sqrt{r^2 + a^2}} - \frac{b}{\sqrt{r^2 + b^2}} \right) - 1 . \quad (6)$$

This normalized apparent resistivity is useful for producing type-curves for field-interpretation; I will however use the un-normalized apparent resistivity because it is easier to understand and the seawater-resistivity of 0.31  $\Omega\text{m}$  was the same for all data in this thesis.

So far, the earth was assumed to be a lower halfspace of homogeneous electric resistivity. This was sufficient to outline the principle of the method. For the inversion of field data I will now extend the model to include a layer of thickness  $d$  and resistivity  $\rho_1$  over a halfspace of resistivity  $\rho_2$ . The magnetic induction  $B$  can be found in the same way as the simpler model treated above. The solution at the seafloor ( $z=0$ ) is:

$$B(r) = \frac{\mu_0 I}{4\pi} \int_0^{\infty} \frac{(1-K_{01})(1-K_{12}e^{-2\Theta_1 d})}{1 + K_{01}K_{12}e^{-2\Theta_1 d}} \frac{1}{\Theta_0^2} \left( e^{-\Theta_0 b} - e^{-\Theta_0 a} \right) J_1(\lambda r) \lambda d\lambda . \quad (7)$$



For the dc-case an expansion of the denominator, term-by-term integration and rearranging for stable computing results in

$$B(r) = \frac{\mu_0 I}{4\pi r} (1-K_{01}) \sum_{n=0}^{\infty} (K_{01}K_{12})^{2n} \left\{ f(2n) - K_{12} \left[ (1+K_{01})f(2n+1) - K_{01}K_{12}f(2n+2) \right] \right\} \quad (8)$$

where

$$f(m) = \frac{a+2md}{\sqrt{r^2+(a+2md)^2}} - \frac{b+2md}{\sqrt{r^2+(b+2md)^2}}$$

The height  $b$  of the lower electrode must be included in the calculations as is seen on figure 2-2a: The magnetic induction calculated for a 20  $\Omega$ m halfspace decreases by an order of magnitude when the height of the lower electrode equals the transmitter-receiver separation. The electrode height does not affect the apparent resistivity expression (6) except when induction becomes important as can be seen in figure 2-2b. The effect on the phase difference between transmitted current and received magnetic field (figure 2-2c) is small. Although the height of the lower electrode can be accounted for, inaccurate estimates of it will result in errors in the data interpretation. The effects will be more serious over a more resistive seafloor because channeling and induction in the seawater become relatively more important: the seawater "short-circuits" the transmitter when the lower electrode is lifted up from a

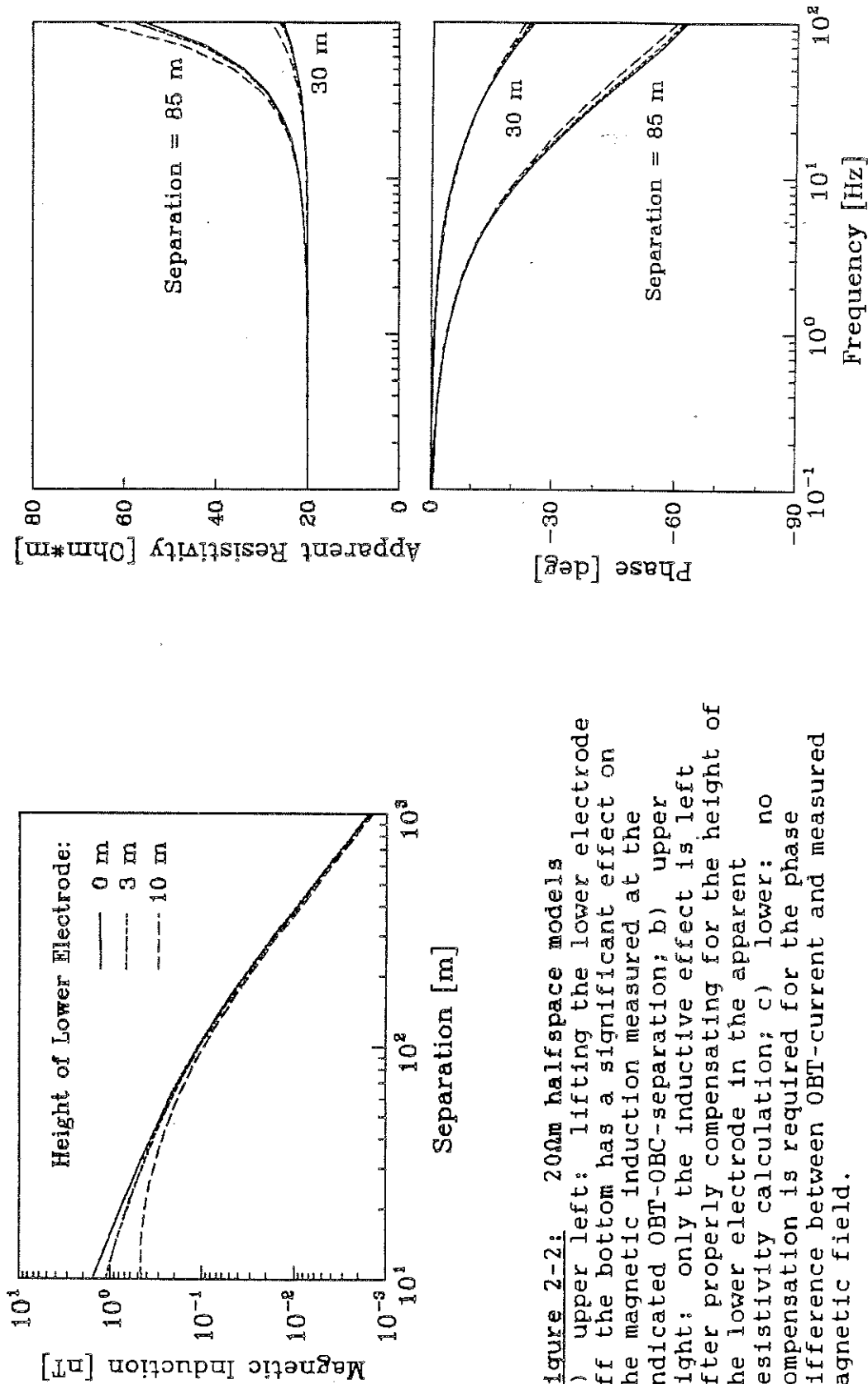


Figure 2-2: 200m halfspace models  
a) upper left: lifting the lower electrode off the bottom has a significant effect on the magnetic induction measured at the indicated OBT-OBC-separation; b) upper right: only the inductive effect is left after properly compensating for the height of the lower electrode in the apparent resistivity calculation; c) lower: no compensation is required for the phase difference between OBT-current and measured magnetic field.

relatively resistive seafloor. The level of the useful signal decreases rapidly.

The measured magnetic induction  $B(r,0)$  on the seafloor changes when any small change  $\delta\rho$  occurs in the seafloor resistivity  $\rho(z)$  over an interval  $\delta z$  at some depth  $z$ . The total change in  $B$  is:

$$\delta B(r,z=0) = \int_0^{\infty} F(r,z) \delta(\ln\rho) dz . \quad (9)$$

Edwards et al. (1984) derived the Frechet Kernel  $F(r,z)$  for the MOSES-configuration over a crustal halfspace when the transmitter-receiver separations are large compared with the ocean depth but small enough to prevent inductive losses in the seafloor halfspace. These conditions were required for a closed-expression dc-magnetic induction  $B$  and are not necessary for the MINI-MOSES configuration. The Frechet Kernel for MINI-MOSES over a halfspace in the radial wavenumber domain is:

$$F(\lambda,z) = \frac{(dB/dz)^2 + \lambda^2 B^2}{dB/dz} \Big|_{z=0^+} \quad (10)$$

where all functions are closed expressions and  $z=0^+$  means "just below the seafloor". A useful sensitivity function  $S(r,z)=F(r,z)/B(r,0)$  is obtained through normalization with the total  $B(r,0)$  produced by the finite source wire. Observing that  $\delta(\ln\rho)=\delta\rho/\rho$ , equation (9) becomes:

$$\frac{\delta B(r,0)}{B(r,0)} = \int_0^{\infty} S(r,z) \frac{\delta\rho}{\rho} dz \quad (11)$$

where the sensitivity function

$$S(r,z) = \frac{2r [r^2+(a+2z)^2]^{-3/2} - 2r [r^2+(b+2z)^2]^{-3/2}}{(a(r^2+a^2)^{-1/2} - b(r^2+b^2)^{-1/2}) / r} \quad (12)$$

$S(r,z)$  equals the fractional change  $\delta B(r,0)/B(r,0)$  if a unit fractional change  $\delta \rho(z)/\rho(z)$  over an interval  $\delta z$  at some depth  $z$  down the lower halfspace occurs. It is valid only for the MINI-MOSES configuration over a seafloor halfspace that is several times more resistive than the seawater. Edwards et al. (1984) showed for their configuration that a resistivity contrast of 1:10 results in a few percent error in  $S$ . Examples for sensitivity functions are plotted in chapter 4 (figure 4-12a). They indicate that most of the resistivity information comes from depths  $z$  around one half the transmitter-receiver separation  $r$ .

If the model differs from the resistive halfspace or if the sensitivity of phase-data is desired then a numerical approach appears easier: A thin layer of perturbed resistivity is inserted consecutively at each depth in the model and the numerical partial derivatives in the simulated data are calculated and assembled in a partial derivative matrix. Each row contains one (un-normalized) sensitivity function  $S_i(z)$  for the  $i$ 'th datum. The data could be the magnetic field amplitude or the phase at some transmitter-receiver separation and at some transmitter frequency.

Edwards (private communication) programmed an iterative inversion algorithm based on Jupp and Vozoff's (1975) analysis of the problem of: how to find the parameters of an a priori geophysical model (e.g. a horizontally stratified earth) from incomplete and inaccurate data. The algorithm uses the singular value decomposition of a (numerical) partial derivative matrix (Jacobian) to define an eigenparameter space and an eigendata space at each iteration. Because of the assumed linear relation between parameters and data, any eigenparameter has the same direction as its perturbation. The parameter correction vector for each iteration is then determined from the eigenparameters weighted by their importance. The sensitivity functions contained in the Jacobian are essential for the stability of this algorithm because the singular values from the decomposition of the Jacobian serve as a measure of the "importance" of certain parameter combinations (eigenparameters). I have adapted this algorithm for the inversion of MINI-MOSES data.

## 2.2 THE EFFECT OF AN INCLINED SOURCE-BIPOLE

A potentially serious source of error in the MINI-MOSES experiment is an inclination of the 'vertical' wire, from water currents. The error is estimated in this section.

The source wire is anchored to the transmitter package on the seafloor. Its top end can move freely in a horizontal water current. Three spherical floats are attached on a string to keep the wire upright. Each float has the radius 0.13 m and the buoyancy force  $F_b = 44\text{N}$ . For typical water currents of  $v = 0.01\text{--}0.5\text{ m/s}$  (ALVIN-crew, private communication) Reynold's number  $Re = \lambda v \rho / \eta$  is above  $10^3$  for the wire and above  $10^4$  for a float.  $\lambda$  is a typical dimension,  $\rho = 1000\text{ kg/m}^3$  is the density and  $\eta = 0.0018\text{ Pa}\cdot\text{s}$  is the dynamic viscosity (Mende and Simon, 1974) of water at  $0^\circ\text{C}$ . The flow is therefore not laminar. It exerts the force (Gerthsen et al., 1974)

$$F_d = \frac{1}{2} c A \rho v^2$$

on a body with the cross-sectional area  $A$  measured perpendicular to the flow. The drag coefficient  $c$  is  $c=0.47$  for a sphere with  $Re < 10^5$ , and  $c=1$  for a long circular cylinder with its axis perpendicular to the flow (Mende and Simon (1974)).

The shape of the wire can be found after dividing the wire up into small elements  $d\ell$  which are a distance  $\ell$  away from the top. The angle  $\alpha$  between the topmost wire element and the vertical is illustrated in figure 2-3a. It is determined by the resultant of the buoyancy force  $F_b$  and the drag force  $F_d$  at the floats. A small force  $d\mathbf{F}(\ell)$  at each wire element results from its weight  $F_g = dm \cdot g$  and the water drag  $F_d(\ell)$  as illustrated in figure 2-3b. The equilibrium of this  $d\mathbf{F}$  with the upward tension  $\mathbf{F}(\ell)$  and the downward tension  $-\mathbf{F}(\ell+d\ell)$  represents a recursion relation for  $\mathbf{F}$ . Knowing  $\mathbf{F}(\ell)$ , the angle  $\alpha(\ell) = \tan^{-1}(F_y(\ell)/F_z(\ell))$  of this wire element can be calculated and from it the position of the next wire element. The resulting shape of a 100 m long wire is shown in figure 2-4 for different water velocities. The horizontal displacement of the top end of the wire is approximately  $\Delta y = 280 \cdot v^2$  so that a water current of 0.06 m/s displaces the floats by 1 m in 100 m.

The magnetic field of the vertical wire in the sea [eq. 2(1)] may be separated into the contribution from the ungrounded wire and the contributions from the current source and sink in the presence of the electrical resistivity boundary at  $z = 0$ . The contribution from a dislocated current source is:

$$B_{\phi}^{+}(\underline{r}) = \frac{\mu_0 KI}{4\pi r^{+}} \left( \frac{b}{\sqrt{(r^{+})^2 + b^2}} - 1 \right) \quad (1)$$

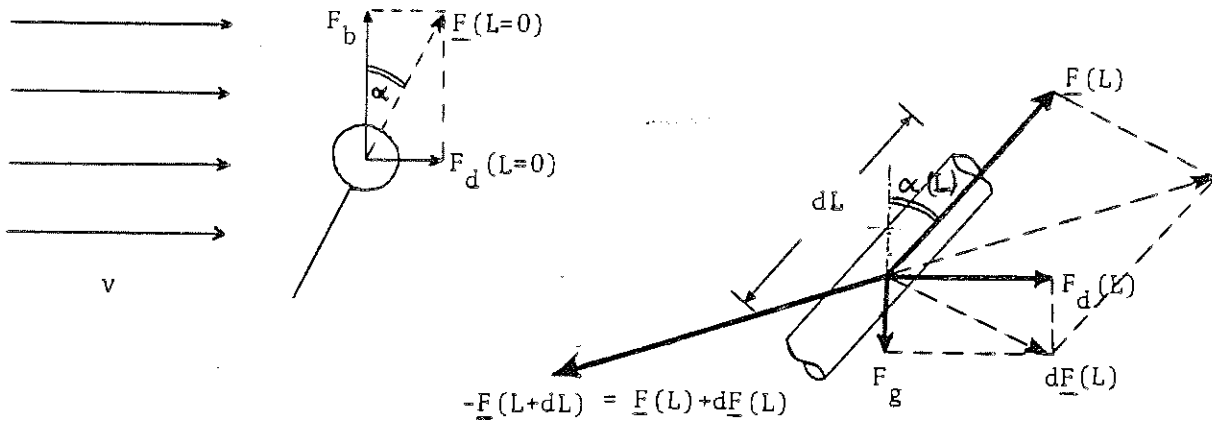


Figure 2-3: (a) left: the forces on the float at the upper end of the wire; (b) right: the forces on each wire element.  $F_b$  = buoyancy,  $F_d$  = drag,  $F_g$  = gravitation.

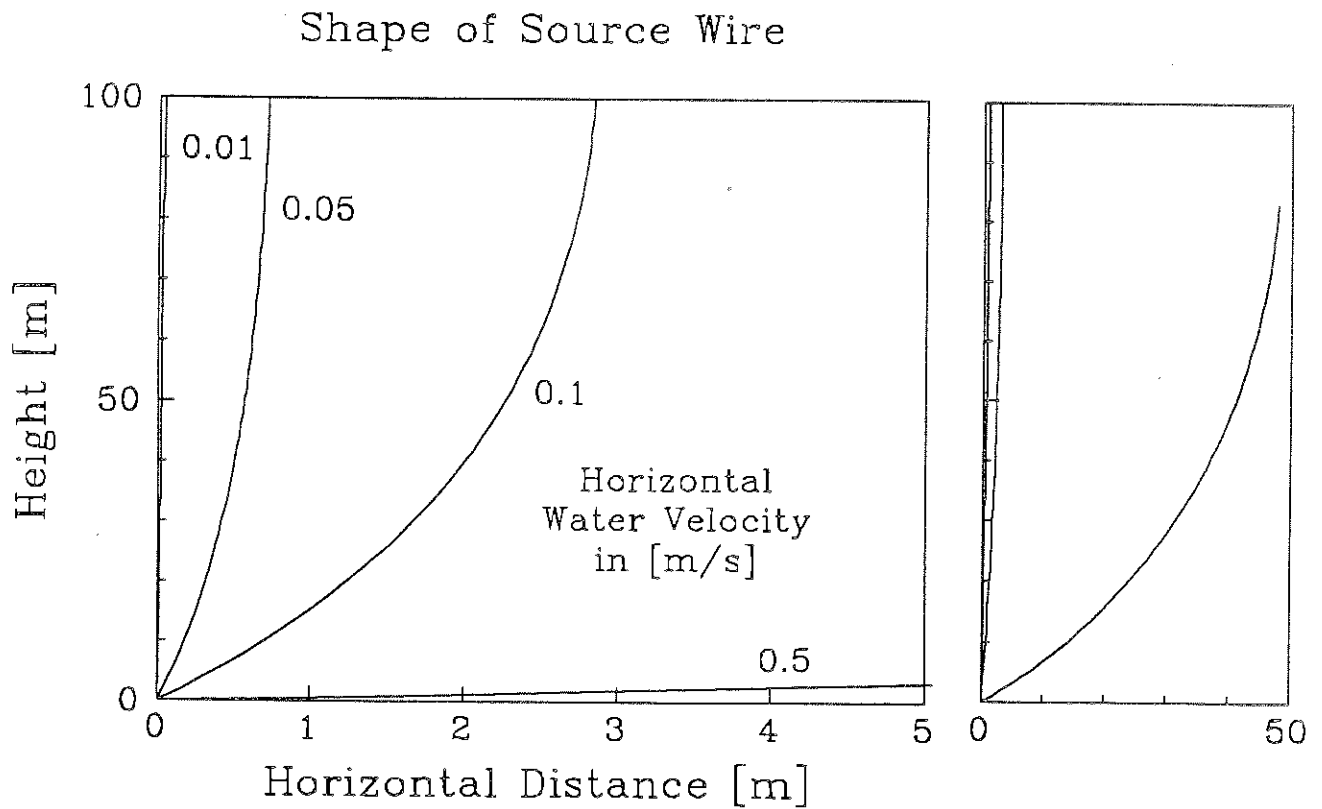


Figure 2-4: The resulting shape of the wire for typical water velocities with a horizontally exaggerated scale (left) and a 1:1 scale (right).



and from a dislocated current sink:

$$B_{\phi}^{-}(\underline{r}) = \frac{\mu_0 KI}{4\pi r^{-}} \left( 1 - \frac{a}{\sqrt{(r^{-})^2 + b^2}} \right) \quad (2)$$

where  $r^{+} = [(x-x^{+})^2 + (y-y^{+})^2]^{1/2}$ ,  $r^{-}$  ditto, and  $\phi^{+}, \phi^{-}$  indicate the corresponding azimuthal components in the dislocated cylindrical coordinate systems. The contribution from the ungrounded wire (Biot-Savart's law) is:

$$\underline{B}^w(\underline{r}) = \frac{\mu_0 I}{4\pi} \int_0^D \frac{-\hat{d}(s) \times \hat{r}(s)}{|\underline{r}(s)|^2} ds \quad (3)$$

where the hat indicates a unit vector and the symbols are defined in figure 2-5. A numerical evaluation of the line integral in (3) along an arbitrary source wire will be inaccurate when the step size approaches the distance between wire element and field point. This can be avoided if the wire is divided into a number of straight finite elements  $\underline{d}$  between  $\underline{r}_1$  and  $\underline{r}_2$ . Using the solution of (3) for a straight wire element ( $\underline{d}$  not a function of  $s$ ) which is obtained from (3), after some vector algebra:

$$\underline{B}^w = \frac{\mu_0 I}{4\pi} \left( \hat{r}_1 \times \hat{r}_2 \right) \frac{1}{|\underline{r}_1|} \frac{1 - \hat{r}_1 \cdot \hat{d} \frac{|\underline{r}_2| - |\underline{r}_1|}{|\underline{r}_2 - \underline{r}_1|}}{1 - (\hat{r}_1 \cdot \hat{d})^2} \quad (4)$$

Given the location of source and sink and the shape of the wire in between, then (1), (2), and (4) allow the calculation of  $\underline{B}$  in the presence of a seafloor halfspace.

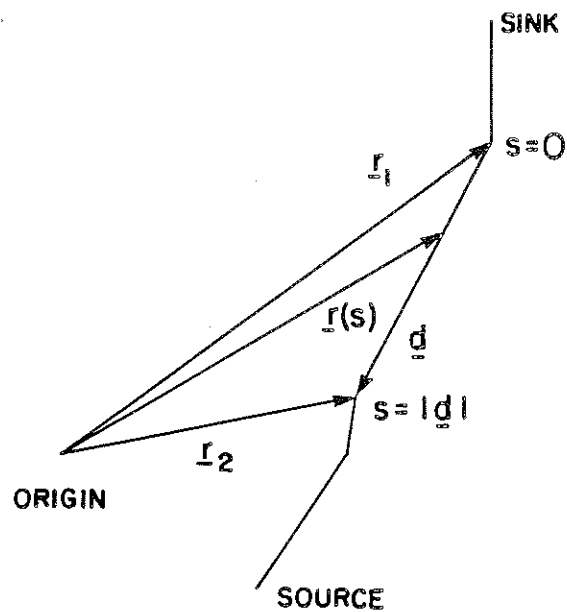
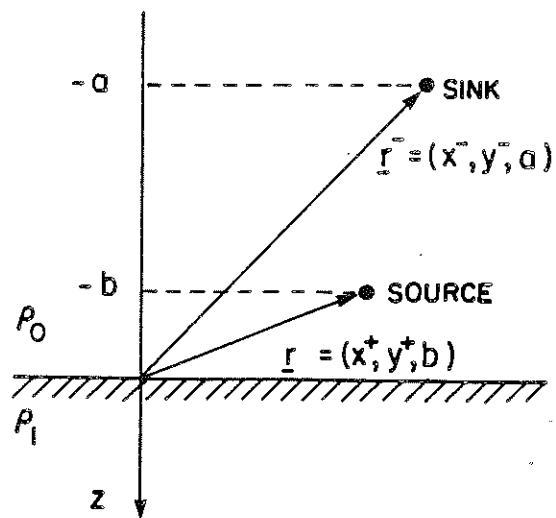


**Figure 2-5:** The geometry of the inclined source wire; a) upper: location of sink and source, b) lower: the straight wire element as part of a polygon connecting sink and source.

The results for a 20  $\Omega$ m halfspace underneath a 0.31  $\Omega$ m sea, and a source wire composed of one straight element only, are shown in figure 2-6. The magnetic induction vector  $\underline{B}$  is represented by arrows in the plane of the seafloor, their lengths were obtained after normalizing the amplitude  $|\underline{B}|$  with 0.03 nT and then scaling it logarithmically. In the upper graph  $\underline{B}$  is curling around a vertical source wire. The lower picture shows the difference left after subtracting the vertical-source  $\underline{B}$  from the  $\underline{B}$  produced by a source wire inclined by 1 m in 100 m. It is relatively large near the source but is decreasing faster with distance than the vertical source field. Edwards et al. (1981) upon studying the effect on the MOSES method of a wire bent into a circular arc with a maximum deviation of 1% of the length found that the field in the plane of the arc falls off faster than the field of a vertical MOSES source.

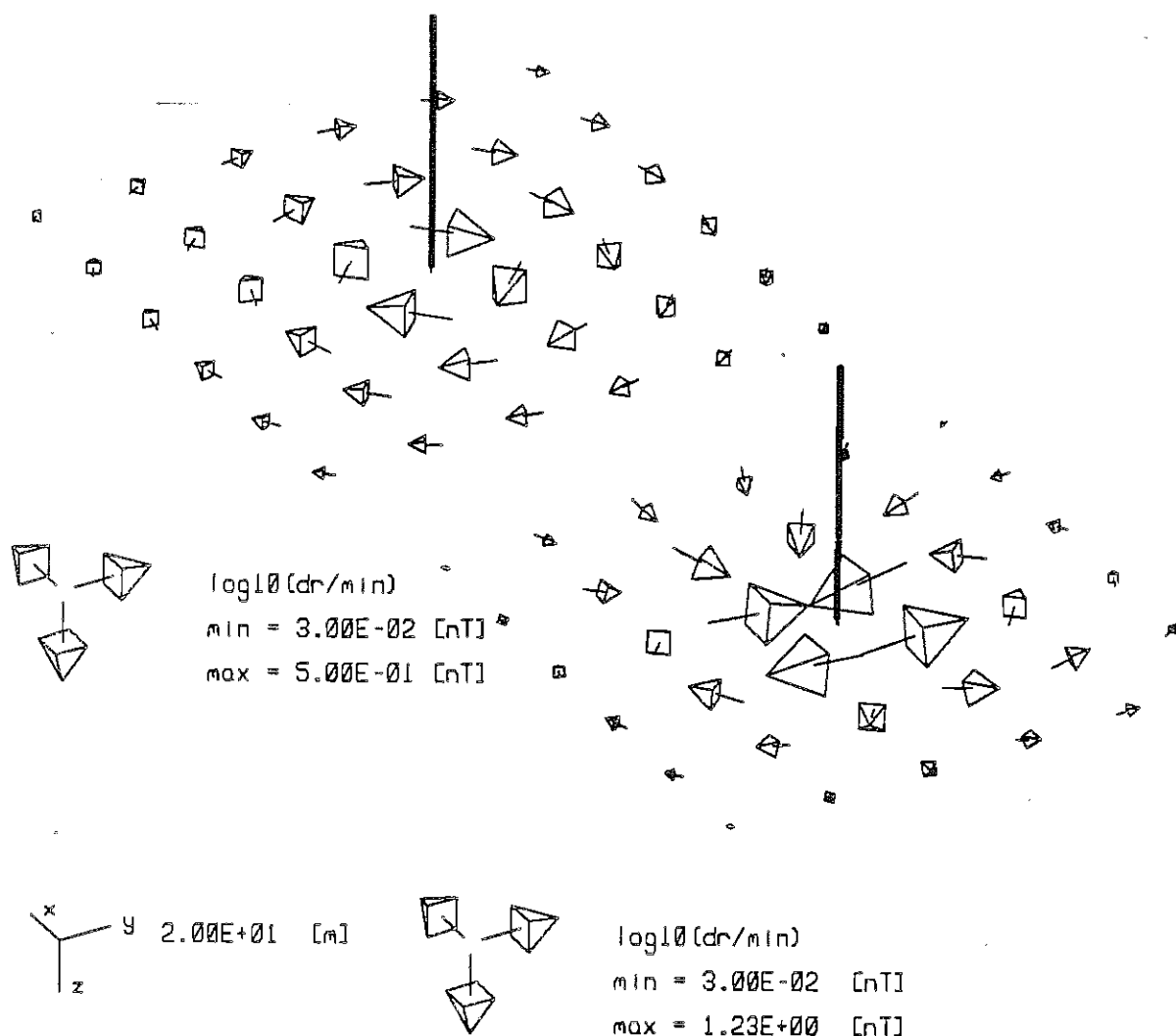


Figure 2-6: Perspective view of the magnetic induction vectors  $\underline{B}(x,y,0)$  for a  $20 \Omega\text{m}$  seafloor. Their amplitudes are logarithmically scaled after division by  $0.03 \text{ nT}$  for better viewing. (a) upper: field of a vertical source wire between  $(0,0-3\text{m})$  and  $(0,0-100\text{m})$ ; (b) lower: The difference  $\underline{B}_i - \underline{B}_y$  between  $(0,0,-3\text{m})$  and  $(0,1\text{m},-100\text{m})$  and the field of a vertical source. This difference falls off faster with distance than the field of the vertical source.

### 2.3 INDUCED POLARIZATION AND TWO-DIMENSIONAL EFFECTS

The data presented in a later chapter in this thesis were gathered near a seafloor metallic sulphide deposit. They may therefore include transient decays due to charge accumulation at the boundary between the metallic conductor and the saline water. This process is commonly referred to as induced polarization (IP). A compilation by Pelton et al. (1978) of frequency domain IP results from sulphide deposits on land indicates ground impedance decreases of several percent in the amplitude and rotations of up to 10 degrees in the phase, near deposits.

The skin depth for electromagnetic induction in a high grade sulphide ore ( $1 \Omega\text{m}$ , Telford et al., 1976, p. 453) is on the order of 150 m for a frequency of 10 Hz and thus falls within the range of MINI-MOSES. Electromagnetic Induction was therefore included in the simulation of the measured magnetic induction B on the seafloor in section 2.1. For future applications of the MINI-MOSES method it will be desirable to simulate induction in three-dimensional or at least two-dimensional conductivity structures. This was traditionally done by either solving a Helmholtz equation for the electric or magnetic field on a finite difference (or finite element) grid or by an integral equation approach. The only published solutions for the

two-dimensional problem use a finite element method (Stoyer and Greenfield, 1976) and a hybrid method (Lee and Morrison, 1985), to find the magnetic field of oscillating magnetic dipole sources by Fourier transforming the problem into the strike-direction wavenumber-domain.

In appendix B, I have outlined an integral equation solution to the two dimensional induction problem, which for the MINI-MOSES method has two advantages over a finite difference or finite element approach:

- (a) Once the Green functions for the conductivity structure are set up as a coefficient matrix in a linear system of equations then a moving source as in the MOSES or MINI-MOSES method will only change the right hand side of the equations. Little extra work is thus required for each source location.
- (b) After the digitization is done the electrical conductivity can be separated from the Green functions. Induced polarization can then simply be included as a frequency-dependent complex conductivity according to the Cole-Cole model (see for example Pelton et al., 1978).

### 3. INSTRUMENTATION

The experiment described later in this thesis was done with

- a) an electric current transmitter (OBT)
- b) an induction coil magnetometer (OBC)
- c) Pacific Geoscience Center (PGC) deployment / recovery packages
- d) an ocean bottom navigational system
- e) the deep submersible ALVIN for moving OBT and OBC about on the seafloor
- f) the USS ATLANTIS II for deployment and the USS WYCOMA for recovery.

The OBT and OBC were designed, constructed, and equipped with the Department of Physics, Electronics Workshop microprocessor module, by myself with much guidance and help from Dr. G.F. West and Dr. R. Nigel Edwards, and with help from the summer student Jeremy B.G. Hughes. The two instruments will be described in this chapter.

The deployment and recovery packages have been developed and used routinely by Dr. Lawrie K. Law of the Pacific Geoscience Centre, at Sidney, British Columbia. They consist of 2.5 cm thick, 56 cm inside diameter aluminum pressure spheres with an equatorial midring carrying electrical feed-throughs, and a radio-beacon and strobe-

light attached outside for recovery. An electromagnet powered from inside the pressure sphere holds on to a metal part of an anchor weight. When the power is switched off, the anchor is released and the now buoyant package floats up to the surface. The pressure spheres are spun from the heat treated, rolled aluminum alloy T-7075-T6 that has a room-temperature (20°C) electrical conductivity of  $1.92 \times 10^7$  S/m (ASM, 1983, p. 294). The pressure spheres were tested to 4.5 km water depth at the Defense Research Establishment Atlantic in Dartmouth, Nova Scotia prior to the ALVIN-experiment.

The positions of OBT and OBC were determined from the positions of the deep submersible ALVIN at the time of deployment. Continuous ranging between ALVIN and a sea bottom acoustic transponder net is used to update ALVIN's position as well as to improve the transponder positions by least squares analysis of ALVIN's movements. Positions are plotted onboard ALVIN. They are reproducible to within  $\pm$  10m according to the experienced chief pilot Dudley Foster.

All power in the OBT-package and in the OBC-package is supplied by Lithium batteries which are characterized by high energy density (in volume and weight), by negligible internal resistance and by a constant voltage under load through 3/4 of their life time.



### 3.1 THE OCEAN BOTTOM TRANSMITTER (OBT)

Since the first test of the MOSES system in Queen Charlotte Sound in 1982 I have been designing and testing a remote battery-powered transmitter for a MINI-MOSES type system. The proposed technique to investigate seafloor metallic sulphides called for a transmitted current waveform typical for induced polarization methods on land (figure 3-1a). Transient decays would be measured during the off-times. The Fourier transform (figures 3-1b,c) shows that most of the power is contained in the base frequency. The fourier transform was calculated according to appendix A. In contrast to the usual definition of a discrete Fourier transform I have chosen the digitization  $t_j = (j+1/2)*\Delta t$ , where  $\Delta t$  is the sampling interval. This is equivalent to sampling the time series at the centers of the digitizing intervals. The usual  $t_j = j*\Delta t$  would create an unwanted time shift of half a digitizing interval.

Electric current transmitters used in land geophysical surveys typically drive milliamperes to Amperes with kilowatt power because of the relatively high ground resistances. Carefully grounding the electrodes in dry areas is a major concern. In the ocean the electrodes are well coupled to the saltwater with a negligible resistance of the current path in the water. In the first MOSES

### Synthetic OBT Signal

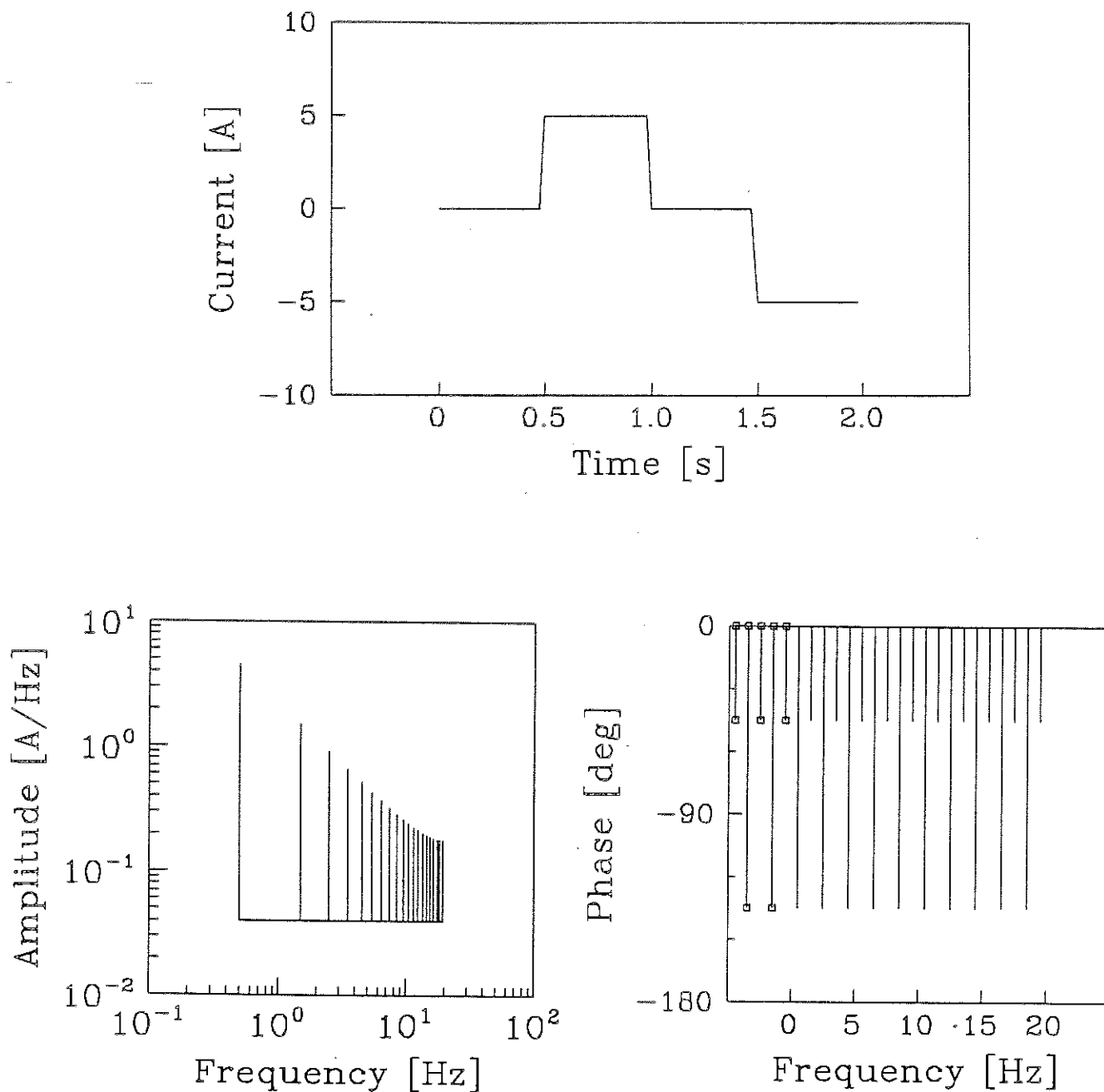


Figure 3-1: The signal from the ocean bottom transmitter (OBT).  
(a) upper: The periodic electric current in Amperes, (b) lower left: amplitude and (c) lower right: phase of its exponential Fourier transform shown for positive frequencies.

experiment (Nobes, 1984) the transmitter drove a current of 9 A through a  $2.5 \Omega$  wire. In the second MOSES survey (Edwards et al, 1985) more current was driven through the same wire because larger electrodes decreased the contact resistance. Improvements in the MOSES-transmitter were in part results of the development of the MINI-MOSES transmitter (OBT). The latter has 50-100 watt capability, is battery-powered and is self-contained in a PGC pressure sphere.

In the first version of the OBT, two 12V/12Ah Gell-Cell batteries with internal resistances of milliohms were alternately switched onto the load - one for the positive current, the other for the negative current. The load was a 15 m cable of  $0.16 \Omega$  resistance in series with two 12.5 cm long, 2.5 cm thick copper cylinder electrodes. In order to save power and to obtain a defined waveform the current was not limited by a resistor but it was regulated with a switchmode regulator circuit instead. Dr. G.F. West showed to me how to build each of the two current regulators: A power field-effect transistor (IRF 531) connects and disconnects the battery from the rest of the circuit every 10-30  $\mu$ s. This time constant is determined by an inductor in series with the load that causes a curved current rise-time by storing energy in its magnetic field. A high power,  $0.38 \Omega \pm 3\%$  resistor in series with the load senses the

current level. When the voltage drop across this sense resistor exceeds a preset level then a driver circuit switches off the field-effect transistor. The energy stored in the inductor's magnetic field is then fed through the load and an ultra fast Schottky power diode (1N 5831) that closes the circuit when the battery is disconnected. The current through the load and sense-resistor decays until at a preset level the field-effect transistor connects the battery back into the circuit.

The operation of the first OBT was controlled by a precision clock and a "hand-wired" logic circuit where the OBT functions: base-frequency, transmit/sleep time and release time were set in binary steps by mechanical switches. The instrument was tested in 1983 in Jervis Inlet, British Columbia, during the first successful MOSES-survey using the ocean bottom magnetometers (Nobes, 1984) as receivers. The periodic signal averaged over one hour is shown in figures 3-2a and 3-2b for two consecutive runs. The cause for the asymmetry in the waveforms was revealed during a battery test (figure 3-2c) with the electrodes immersed in a tank of 3 kg salt per 100 liter "seawater". Several effects were detected: a) one battery drained much faster than the other one because it was damaged (figure 3-2c), b) a strong chemical reaction occurred at the electrodes, and c) the available voltage was too small for

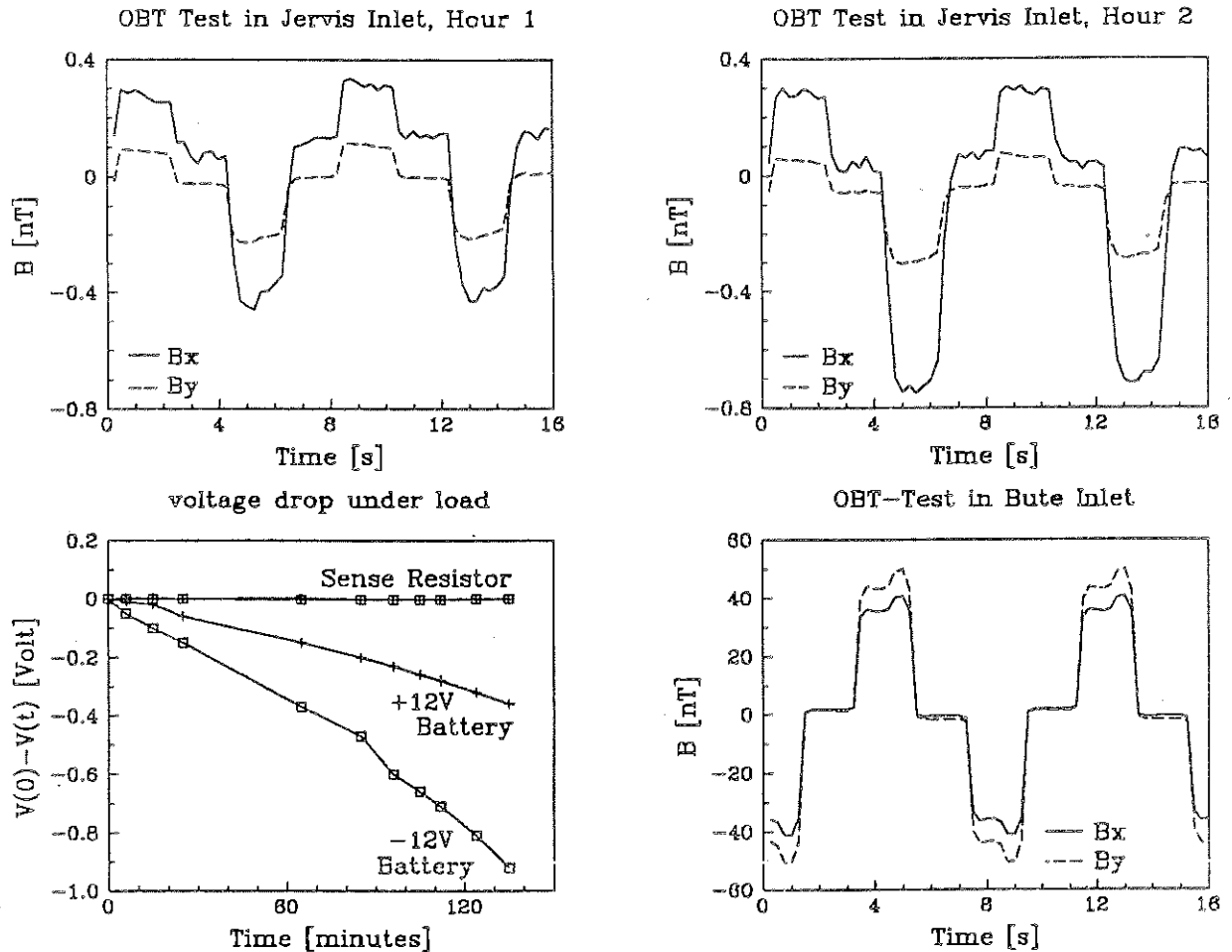


Figure 3-2: Results from early versions of the OBT: (a,b) upper: the two-battery-design of the first OBT together with a high load resistance resulted in an asymmetric waveform. (c) lower left: one of the two batteries discharged faster than the other, (d) lower right: the second version used a relay to reverse polarity which resulted in a symmetric waveform.

the current regulator. After experimenting with different types of electrodes it became apparent that the voltage drop across the load had been too high because

- a) electric charges at the boundary between metal and electrolyte opposed the applied voltage with up to 1.5 volt and
- b) the electrodes had been too small so that the dc contact resistance was too large. Stainless steel pipes, 45 cm long and 4.8 cm in diameter, offered a compromise between low contact resistance and weight, and they reduced the polarization effects considerably.

An expression for the contact resistance  $R$  of a perfectly conducting cylinder of length  $\ell$  and diameter  $a$  in an infinite medium of resistivity  $\rho$  was derived by Sunde (1968, p. 75) after integrating the electric potential over the surface of the cylinder and dividing it by the driving current:

$$R = \frac{\rho}{2\pi\ell} \left\{ \ln \left[ \frac{2\ell}{a} \left( 1 + \sqrt{1 + (a/2\ell)^2} \right) \right] + \frac{a}{2\ell} - \sqrt{1 - (a/2\ell)^2} \right\}$$

The contact resistance  $1.7 \, \Omega$  of the two small copper electrodes in series has been reduced to  $0.59 \, \Omega$  for the two large stainless steel electrodes in series and is now smaller than the other resistances in the transmitter circuit.

A second version of the OBT was equipped with the stainless steel electrodes at the ends of a 100 m, 1.05  $\Omega$  wire. Besides modifications in the regulator circuit the main improvement was a double-pole double-throw mechanical relay for reversing the polarity of the transmitted current during the off-times so that only one battery was required. The instrument was tested in February, 1984 in Bute Inlet, British Columbia, during the first successful MOSES-survey that gave convincing results (Edwards et al, 1985) again using the ocean bottom magnetometers as receivers. As seen on figure 3-2d the signal was symmetrical but there appears to be a problem with the current regulator that had to be dealt with in the next and final OBT version.

Early in 1984 it became apparent that a MINI-MOSES experiment requires more flexibility in operating the OBT which could only be provided by a microprocessor control. The final version used in the August/September 1984 experiment with ALVIN was therefore a modular package (figure 3-3) with a computer module controlling the operation of the transmitter module and recording the transmitted current waveform and electrode voltage. A release module provided the interface between a sonar receiver with its commercial circuitry for release on coded sonic command, and a time-release signal from the central processor unit. This allowed us to call the instrument back independently of a preset release time.

# THE OBT - PACKAGE

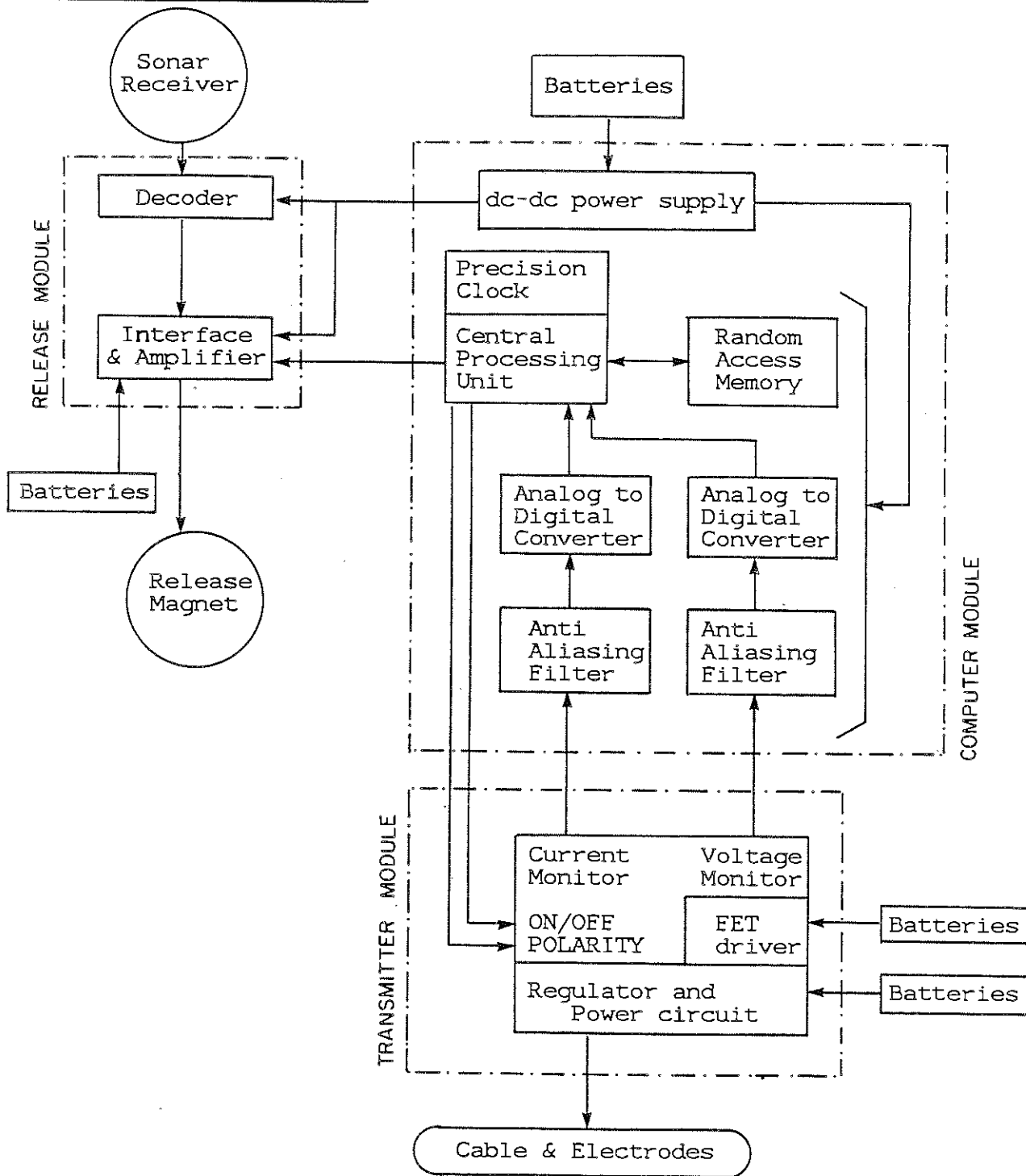


**Figure 3-3:** The modularized latest version of the ocean bottom transmitter. The modules are contained in a separate aluminum box each and so are the battery packs. The parts located outside the pressure sphere are indicated with rounded symbols.



The computer module is equipped with a clock-oscillator (VECTRON CO-236T; accuracy, temperature dependence, and yearly drift at the ppm-level) for stable phase relation with the remote receiver. (The receiver has an identical clock in its computer module.) The central processor unit turns the transmitter on and off and switches the polarity relay. Voltages from the current monitor and from the electrode voltage monitor are low-pass filtered to prevent aliasing in the analog-to-digital conversion. The digital signals are stacked, divided by the number of sweeps in a stack and the so obtained averages are stored in random access memory.

The transmitter module shown in figure 3-4 is interfaced to the computer module with a voltage divider that keeps the two monitor voltages within the common mode range of the two differential inputs to the computer module. The calibration is 2.59 A/V for the recorded current and 8.39 V/V for the recorded electrode voltage below 10 Hz where the anti-aliasing filters roll off. Figure 3-5 shows sample recordings from the ALVIN-cruise. The monitored current and voltage of the OBT are not reversing because they are tapped before the polarity relay. The flat top of 5.2 A in the current waveform indicates that the current regulator was performing well except for a spike later identified in the laboratory at the switch-on edge. The driving voltage 8.5 V



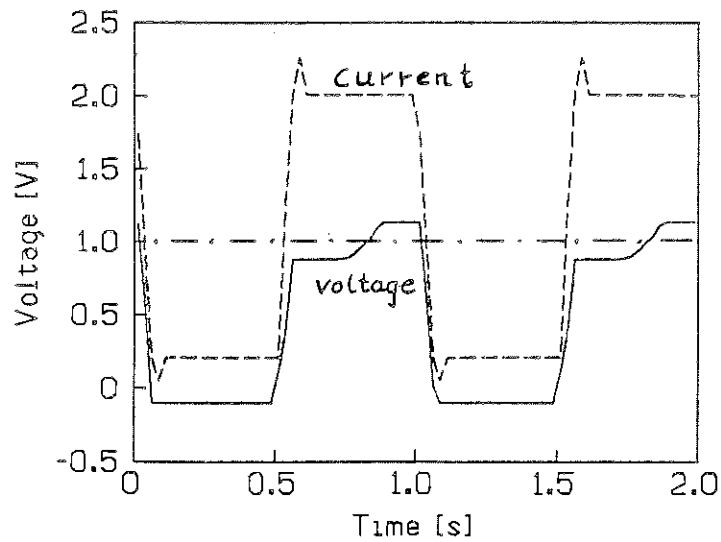
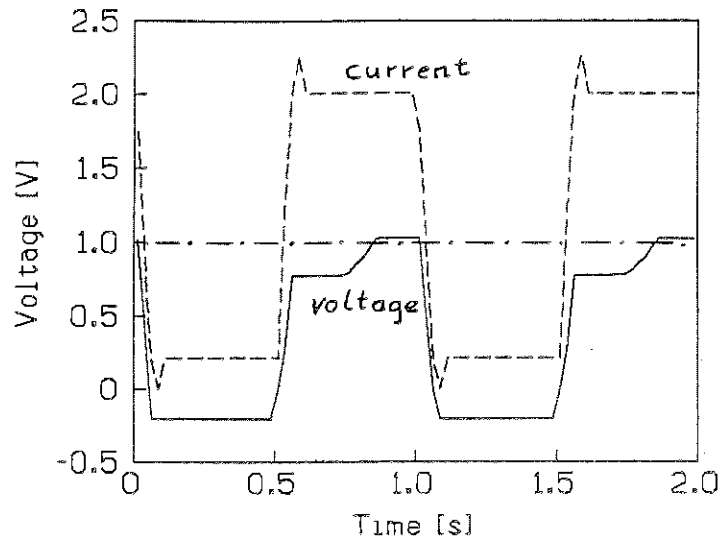


**Figure 3-5:** Un-calibrated monitor data from the ALVIN-cruise: (a) upper: Stack #19, (b) lower: Stack #32. The dot-dashed lines indicate the driving voltage required for non-polarized electrodes. Calibrations are 2.59 A/V for the current monitor and 8.39 V/V for the electrode voltage monitor.

necessary if no polarization occurs is shown as a dot-dashed line in figure 3-5. There appear to be not only late-time charges opposing the driving voltage (curve above the dot-dashed line) but also left-over charges from the previous cycle and the off-time that help to reduce the driving voltage. This could however be a misleading interpretation because the voltage monitor appears to have a zero offset that is different for different recordings.

The current monitor shows a current of 0.54 A during the off-times opposite in polarity to the previous on-time current. With a voltage drop of 0.38 V across the flyback diode this corresponds to 3.0 V at the electrodes if the source is electrode polarization. The voltage monitor indicates only -1.7 V in the upper and -0.9 V in the lower graph of figure 3-5. This inconsistency might be caused by leakage between the transmitter ground and the casing, pressure sphere, water and near electrode although grounds, casings and pressure sphere were carefully isolated from each other.

This OBT cannot be a final version and the following is recommended for future work:

- a) If the transmitter voltage and current would be properly monitored at the output terminals then these monitor records could be used to deconvolve the receiver

records. No current regulation would be required which would make the OBT simpler and more powerful.

- b) More care should be taken in isolating the instrument from the pressure case because this is the prerequisite for a reliable monitor.
- c) The bandwidth of the MINI-MOSES technique could be expanded towards higher frequencies in order to measure induced polarization responses. The mechanical relay in the OBT limits the transmitter frequency with its 50 ms switching time and would have to be replaced by a group of power field effect transistors or other fast switches. The electrodes may have to be calibrated for polarization effects at higher frequencies. The analog to digital converters and the software would have to be faster to keep up with kHz sampling rates.

### 3.2 THE OCEAN BOTTOM INDUCTION COIL MAGNETOMETER (OBC)

Paralleling the development of the latest OBT-version, in early 1984 a new receiver package (OBC) was designed and built for deployment on the August/September 1984 cruise. As shown in figure 3-6 it is modular with release module, computer module and software identical to the OBT-package.

# THE OBC - PACKAGE

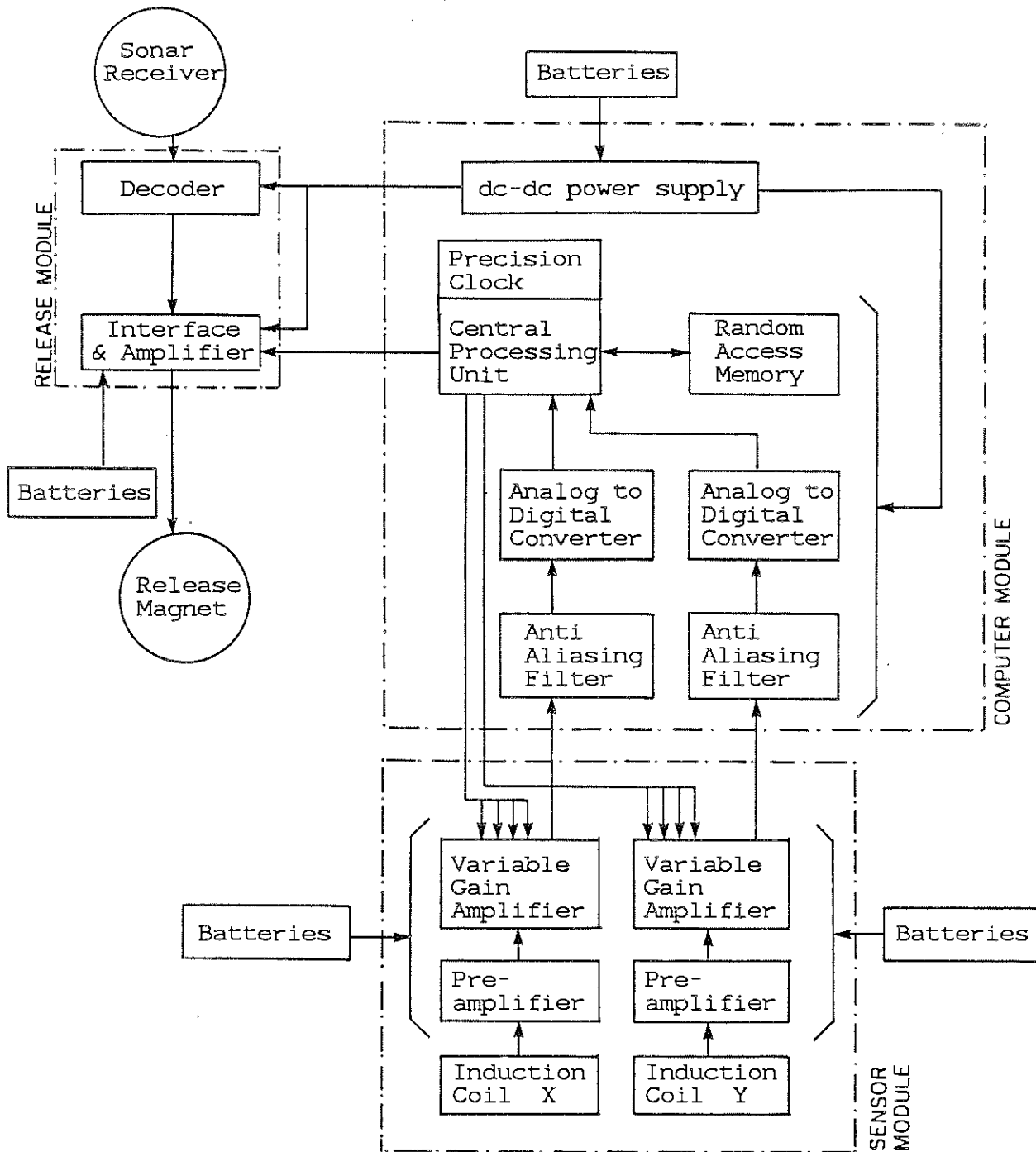


**Figure 3-6:** The magnetic field receiver package has the same release module and computer module as the transmitter package. The sensor module comprises two horizontal field induction coils on the same square steel core, integrating preamplifiers and a CPU-controlled variable gain stage.

Two horizontal components of the time derivative of the magnetic induction are sensed by induction coils. The electromotive force induced in the coil increase linearly with frequency. An integrating current to voltage preamplifier compensates for this increase. This reduces the dynamic range required for the digitization to the dynamic range desired for the magnetic field input. The signals are further amplified in a variable gain stage that serves to expand the 12 bit dynamic range of the analog to digital converters to an equivalent of 18 bit. The signal (and ground) lines are kept separate with separate batteries for the two components in order to prevent "cross-talk" before they are fed into the two differential signal inputs of the computer module.

### 3.2.1 INDUCTANCE AND SENSITIVITY OF THE SENSOR COILS

The sensor design is shown in figure 3-7a. Each of the two horizontal components of the time derivative of the magnetic induction  $dB/dt$  is sensed by a parallel pair of horizontal-axis coils that make up two sides of a square. 14,000 turns on each side have been pilewound by McNeill Electronics, Toronto in non-perfect windings in order to

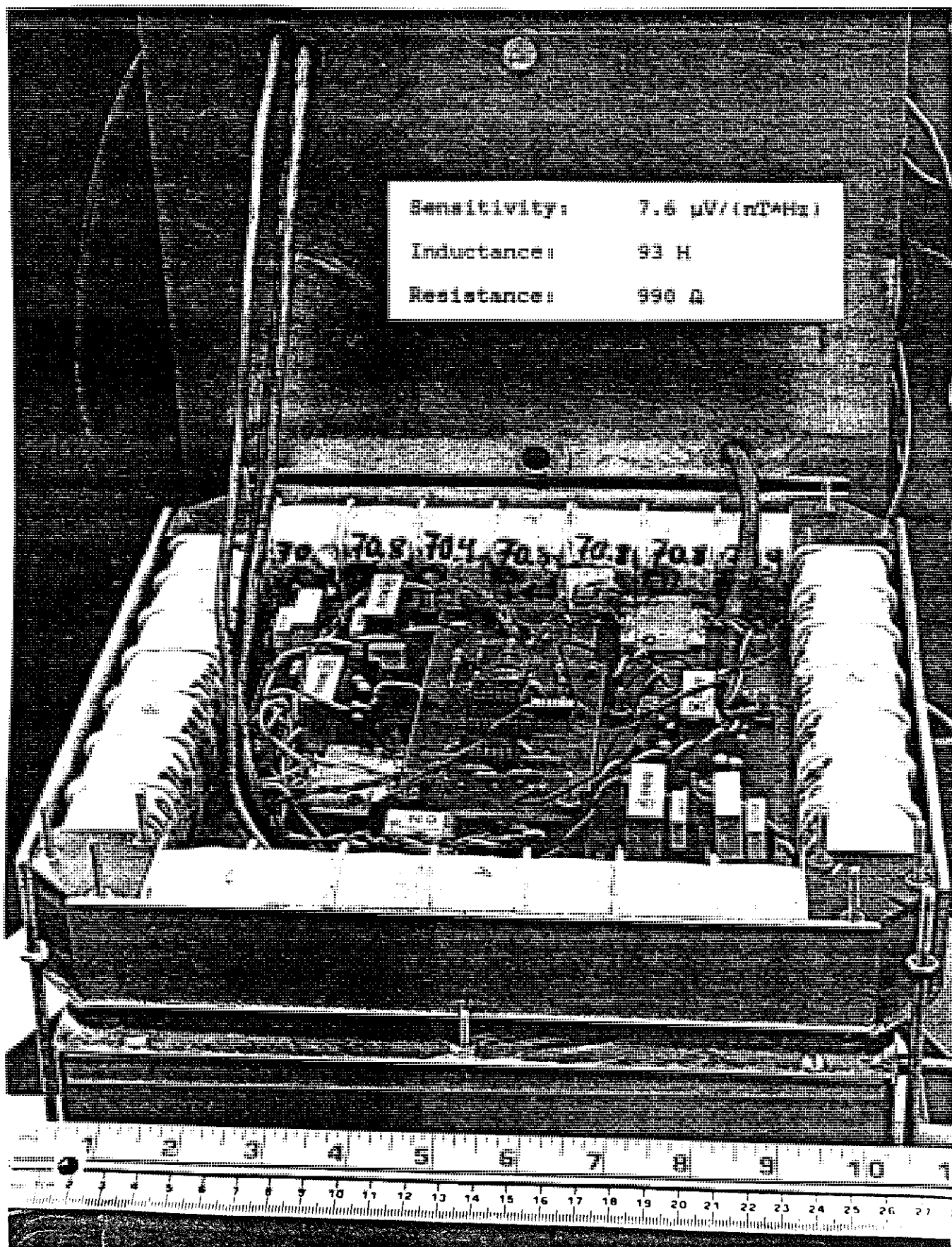


Figure 3-7a: The sensor module with the square cored toroidal sensors (two for each of the two horizontal components of the magnetic induction) and the amplifier circuits.



reduce the capacitance of the coil. Through the four identical coils is threaded a core made of laminated cold rolled 3% Si transformer steel with an initial permeability of (Heck, 1974, chapter 13.4.3) several thousand times  $\mu_0$ .

The pair of coils for one component is connected in such a way that the voltages induced by an external (homogenous) field in each of the coils add. This implies that the mutual inductance  $M_{12}$  due to magnetic flux circulating in the core opposes the self-induced voltages so that the impedance of one pair of coils is

$$Z = i\omega(L_1 + L_2 - 2M_{12}) + R_1 + R_2$$

The resistance  $R = R_1 + R_2$  is 990  $\Omega$ . The inductance  $L = L_1 + L_2 - 2M_{12}$  was measured as  $(93 \pm 1)$  Henry from the step-decay time of the pair of coils in series with the (variable) smaller resistor of a voltage divider. The resistors in the voltage divider reduced the output current from a waveform generator to about 10  $\mu\text{A}$  in order to prevent core saturation. This was even more important for the measurement of  $L_1 \sim L_2 \sim (440 \pm 20) \text{H}$  because here 10  $\mu\text{A}$  produced already 0.14 A/m or about  $10^{-3} \text{T}$  in the core. Using the values of  $L$ ,  $L_1$  and  $L_2$  the coupling factor  $K_{12}$  in  $M_{12} = K_{12} (L_1 L_2)^{1/2}$  is calculated to be  $0.89 \pm 0.02$ . The mutual inductance  $M_{12}$  may be predicted when a coupling factor of 1 is assumed i.e.: all the magnetic flux stays in the core:

$$M_{12} = \frac{n^2}{R'}$$

where  $n=14,000$  is the number of turns on each side and where the core is specified by its reluctance

$$R' = \frac{\ell}{\mu A}$$

i.e.: its total length  $\ell = 4 \times 0.236\text{m}$ , its cross sectional area  $A = 0.029^2 \text{ m}^2$  and its permeability  $\mu$ . The calculated  $M_{12}$  agrees with the measured 440 Henry when assuming  $\mu \sim 5000\mu_0$  which appears large but reasonable.

Two effects due to the shape of the core shall now be considered: leakage of magnetic flux out of the core and gathering of magnetic flux into the core.

The magnetic flux created by a current in one of the coils is schematized in figure 3-7b. Some of the flux may leak out of the core thereby reducing the voltage induced in any of the other coils. This would decrease the effective mutual inductance. It was already estimated above that the coupling factor between opposite coils is  $0.89 \pm 0.02$  so that little flux is lost from the core when going from one side to the other. As a consequence, flux leakage decreases the mutual inductances of opposing coils little.

The second effect is the gathering of magnetic flux into a permeable core that is placed into an external magnetic field. The effect is shown schematically in figure 3-7c.

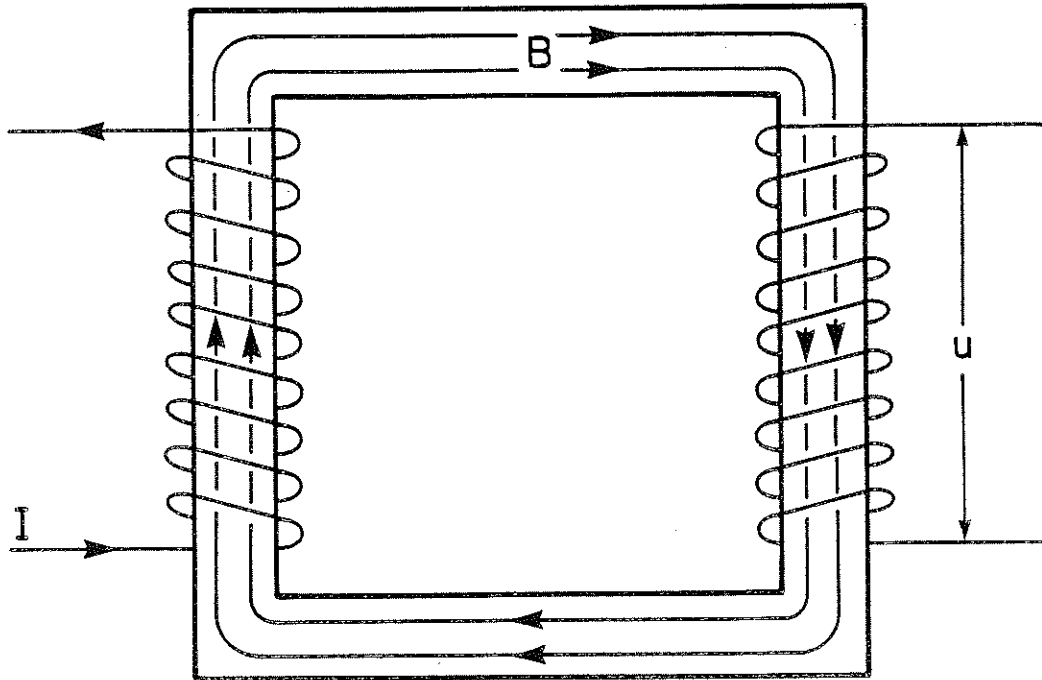


Figure 3-7b: The magnetic flux density  $B$  created by a current  $I$  in one of the coils induces a voltage  $U$  in any of the other coils.

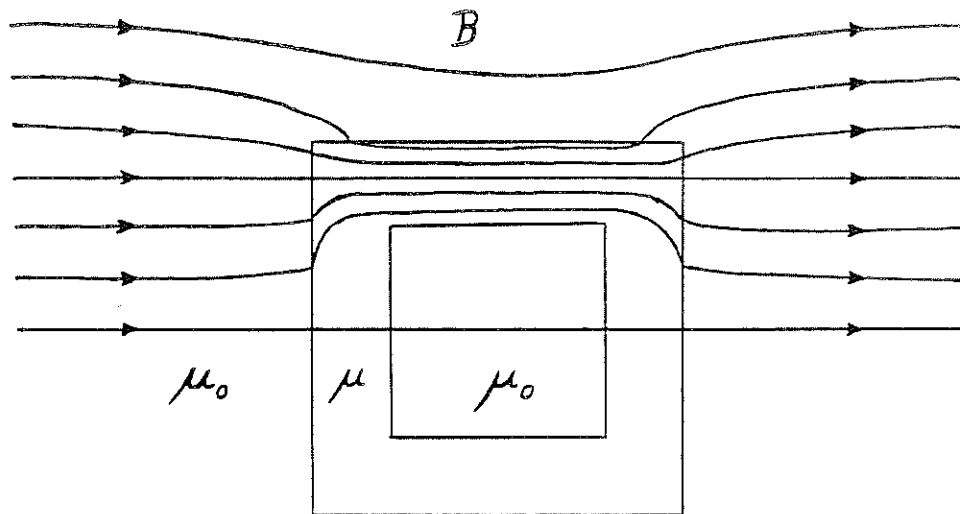


Figure 3-7c: Channeling of the magnetic flux (density  $B$ ) in the square core. Only half the flux lines are drawn because the problem is symmetrical.

The concept of a permeable body channeling magnetic flux is an analogy to the channeling of electric currents by a conductor, which Edwards et al. (1981) approximated by a current channeling number. If we define a flux channeling number for the square rod (thickness  $a$ , length  $\ell$ ) as the ratio of two inverse reluctances

$$\alpha = \frac{\mu a^2}{\ell} / \frac{\mu_0 \ell^2}{\ell} = \mu_r \left( \frac{a}{\ell} \right)^2$$

then  $\alpha/(1+\alpha)$  is a measure of the fraction of flux channeled as compared with a perfectly permeable rod ( $\alpha \rightarrow \infty$ ). For  $\alpha \gg 1$  the fraction approaches 1 so that the rod becomes indistinguishable from one with infinite permeability. For the OBC-coil  $(a/\ell)^2 \sim 0.015$  and  $\mu_r \sim 5000$  so that  $\alpha \sim 75$ .

The same conclusion is obtained after replacing the concept of flux channeling by the concept of an induced magnetization. The core acquires an induced magnetization in an external field. The induced magnetization is reduced by an opposing demagnetizing field that depends on the core's shape. The net effect is an increase in the magnetic induction in the core as compared to the magnetic induction in air. Therefore, the sensitivity of the square cored sensor to an external time-varying magnetic field increases. The increase in sensitivity was measured using a small induction coil in an external field that was produced by a

set of Helmholtz coils. The electromotive force induced in the small coil increased by a factor of 50 after assembling it on the square core. It follows that  $B=50\mu_0 H=50B_0$  where  $B_0$  is the magnetic induction in the coil without the core. The effective relative permeability  $\mu_r \sim 50$  is relatively small compared to the true  $\mu_r \sim 5000$ . This indicates that the demagnetizing field is relatively large. It appears that the effective  $\mu_r$  depends mainly on the core geometry and to a lesser extent on the true permeability of the core material.

With this estimate of the effective permeability of  $\mu_r \sim 50$  it is now possible to predict the sensitivity of the sensor from  $U=i\omega BnA$  as

$$\frac{U}{f B_0} \sim 2\pi \times 50 \times 28,000 \times (0.028 \pm 0.002)^2 \frac{V}{T \cdot \text{Hz}} \sim (7 \pm 1) \frac{\mu V}{nT \cdot \text{Hz}}$$

This is however not as accurate as the value of

$$(7.6 \pm 0.2) \frac{\mu V}{nT \cdot \text{Hz}}$$

that was measured using a pair of Helmholtz coils with radius 60 cm and a total of 150 turns with a 1% field uniformity over 20 cm (for the field uniformity see Everett and Osemeikhian, 1966).

Effects of possible variations in the permeability of the core material were checked by switching a large (5 times

the earth's field) static field on or off while the instrument was measuring a small ( $<1\text{A/m}$ ) oscillating field. No distortion was apparent in the measured small field when monitored on an oscilloscope. This implies that neither the impedance of the coil in the amplifier circuit (hence its inductance) nor its sensitivity were significantly affected.

The coil resonates at 1.5 kHz which using  $L = 93\text{ H}$  shows that the winding capacitance  $C = 1/(\omega^2 L) \sim 120\text{pF}$  is very small. The resonance is very sharp:  $\Delta f = R/2\pi L \sim 1.7\text{ Hz}$  so that it does not disturb the impedance of the sensor within the application bandwidth 0.3-10Hz.

The square-cored induction coil is a promising concept, and the following suggestions can be made for future designs:

The sensitivity may be increased by a factor  $\tau$  without changing weight or size of the sensor by using  $\tau$  times more turns of wire with  $\tau$  times smaller cross sectional area. This would, however, increase the resistance  $R$  and thereby the thermal noise power spectral density  $\tilde{U}^2 d\omega$  (Becker, 1966, §85.a):

$$\tilde{U}^2 d\omega = \frac{2}{\pi} kTR \quad [V^2/\text{Hz}]$$

(Boltzmann's constant  $k = 1.38062 \times 10^{-23}$  J/K, temperature (2°C at the seafloor)  $T=275K$ ) by the factor  $\tau^2$ . The sensitivity is optimized when the thermal noise reaches the noise produced in the amplifier circuit because further increase would not improve the signal to noise ratio.

The inductance of the coils may be varied by balancing the two sides with a small tuning inductor or by adjusting the number of turns. The frequency below which the coil is resistive ( $R/2\pi L \sim 1.7$  Hz at present) should be moved to the lower end of the bandwidth. This would make the coil inductive over the bandwidth so that no integration would be required. A flat phase response and a larger bandwidth without saturation problems in the amplifiers can then more easily be realized.

Dr. H.F. Morrison, University of California at Berkeley, pointed out (private communication) that the U.S. Geological Survey has been using a square ferrite cored induction coil since 1976 for audio-frequency magnetotellurics. Each pair of sensor coils is coupled to a low-noise amplifier by an 80:1 iron cored transformer. The sensor unit is larger and heavier than ours while the coil + transformer has a much lower voltage sensitivity but similar self resonance frequency. Labson et al's (in press) measurements indicate

that the rms noise stays below a few  $\text{pT}/(\text{Hz})^{1/2}$  from 1 Hz to 10 kHz. No technical details were however available so that the low frequency performance of the USGS sensor cannot be compared with our instrument.

### 3.2.2 CALIBRATION OF THE OBC

The sensor coil represents an electromotive force  $U = 7.6(i\omega/2\pi)B$  in  $\mu\text{V}$  (angular frequency  $\omega$  in  $\text{s}^{-1}$ , magnetic induction  $B$  at the OBC in nT) in series with a complex impedance  $Z_L = R_L + i\omega L$  (resistance  $R_L = 990\Omega$  and inductance  $L = 93\text{H}$ ) across the inputs of the low-noise amplifier OPA27 (figure 3-8). A negative feed-back loop serves to integrate below the natural frequency  $2\pi \times 1.7\text{Hz} = \omega_n = R_L/L = 1/(R_{s1}C_{s1})$  of the coil and just amplify above it because there the increasing reactance  $i\omega L$  compensates for the increase in sensitivity with frequency. The first stage amplifies the signal enough so that a standard operational amplifier (356) suffices for the second stage. The high-cuts  $C_{p1}, C_{p2}$  and the high-passes  $C_{12}, R_{12}, C_{23}, R_{23}$  and  $C_{34}, R_{34}$  bandlimit the signal which was mainly useful for testing the instrument in a noisy laboratory. The capacitor



# Sensor Module

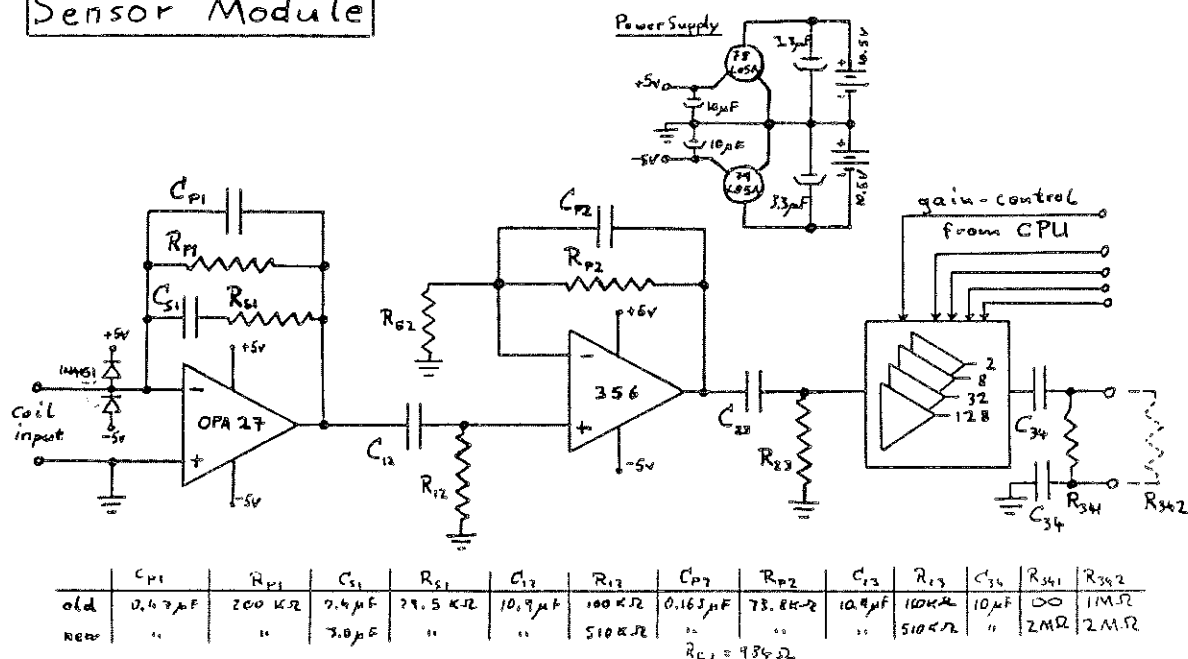


Figure 3-8: The preamplifiers and variable gain stage for one component of the two-component sensor module. Everything shown here is located inside the coil box (figure 3-7).

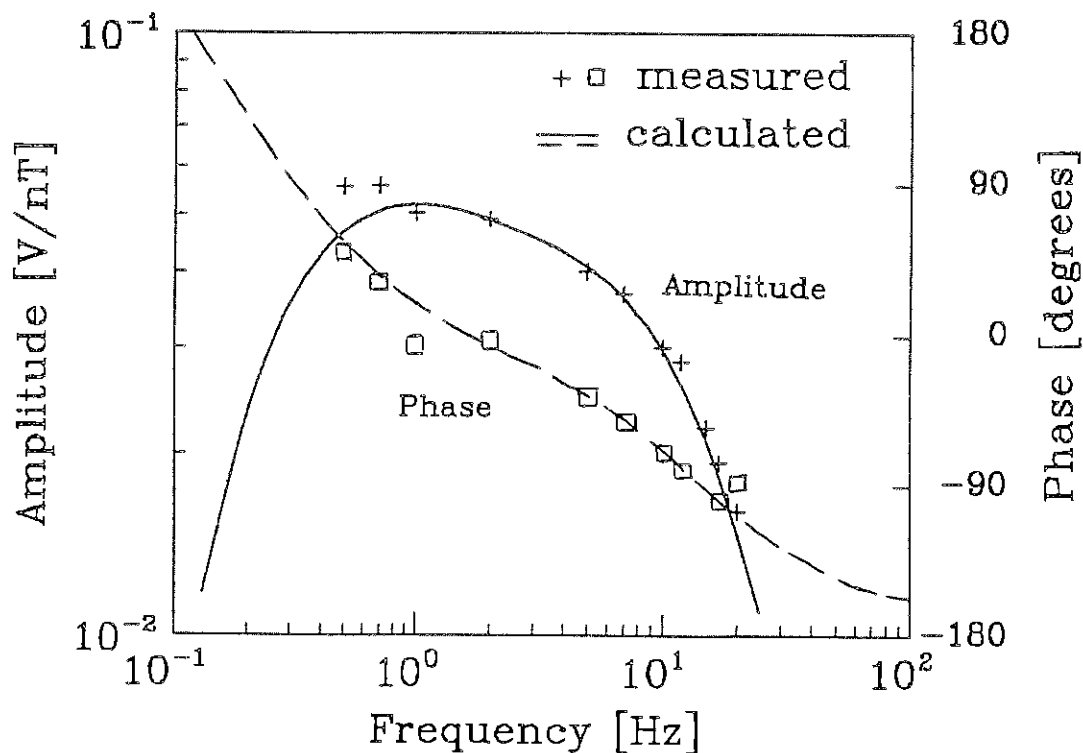


Figure 3-9: Calibration of the sensor module. The values at low frequencies are less accurate because the field produced by the Helmholtz coils became buried in laboratory noise.

$C_{34}$  in the ground line appeared necessary to prevent drifting. The transfer-function for each amplifier stage was derived by combining Kirchhoff's current conservation law at the three nodes closest to the operational amplifier with the condition that the voltage drop across the input terminals is zero without current flow. The product of these transfer functions with the sensor calibration  $2\pi U/i\omega B = 7.6 [\mu V/(nT*Hz)]$  (see above) compares well with the measured frequency calibration as is seen in figure 3-9. The amplitude and phase can be made flatter over the band 0.3 Hz to 10 Hz by carefully tuning  $R_{s1}C_{s1}=L/R_L$  as indicated by the "new" component values in figure 3-8. This was done successfully for a survey near Toba Inlet, British Columbia in October 1984, but the "old" values are applicable to the ALVIN survey in August 1984 which provided the data for this thesis.

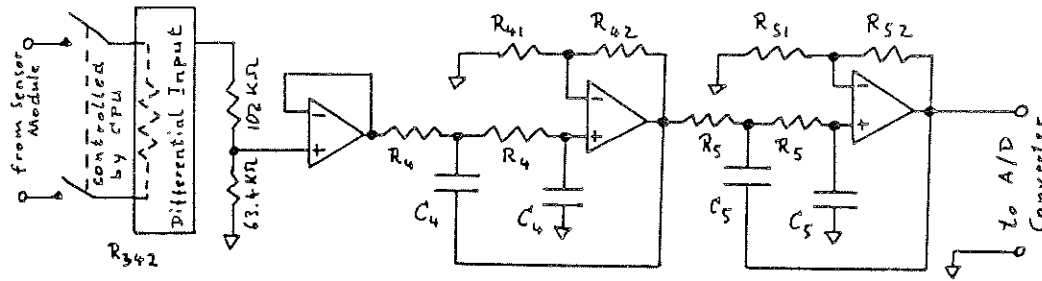
It should be noted that the phase decreases with frequency. This is a direct consequence of the sign-convention  $\exp(i\omega t)$  for the inverse Fourier transforms used later in the data processing. This sign-convention dictated an  $\exp(i\omega t)$  factor in the derivation of the transfer functions. It means that "phase" is defined as the phase of the input (transmitter) minus the phase of the output (receiver).

The variable gain (figure 3-8) has its gain factors carefully adjusted to 2,8,32,128 whereas the software compensates only for 1,4,16,64 so that a factor of 2 has to be included in the transfer function. Another constant factor arises from the voltage divider in front of the anti-aliasing filters (next paragraph) that scales the voltage in order to obtain unity gain for the subsequent filters.

The signals are low-pass filtered before the digitization in order to prevent aliasing from frequencies above half the sampling rate (Nyquist frequency = 20 Hz). The anti-aliasing filters (figure 3-10), built by the electronics workshop as part of the computer module, are two equal-component-value, Sallen-Key, second-order low pass filters (Lancaster, 1975) in series and tuned identically through  $R_4=R_5$ ,  $C_4=C_5$  with a combined  $\omega^{-4}$  or 24 dB per octave roll-off from 10 Hz. The transfer function derived the same way as already explained is in excellent agreement with the measured values as shown in figure 3-11.

Induced electric currents in the pressure sphere modify the magnetic field signal although the wall of the sphere is inductively thin: skin depths of 50cm for 0.1 Hz and 3.6 cm for 20 Hz compared to 2.54 cm wall thickness would limit induction to produce mainly currents parallel to the surface. The effect of these currents on the magnetic field

# Anti - Aliasing Filters



|     | $R_{342}$   | $R_4, R_5$     | $C_4, C_5$ | $R_{41}, R_{51}$ | $R_{42}$        | $R_{52}$        |
|-----|-------------|----------------|------------|------------------|-----------------|-----------------|
| old | 1M $\Omega$ | 487 K $\Omega$ | 33 $\mu$ F | 39.2 K $\Omega$  | 5.90 K $\Omega$ | 48.7 K $\Omega$ |
| new | 2M $\Omega$ | "              | "          | "                | "               | "               |

Figure 3-10: The two second order anti-aliasing filters for one channel (the other channel is identical). The voltage-divider at the input scales the input voltage so that the filter has unity gain at low frequencies.

## Anti Alias Filter Transfer Function

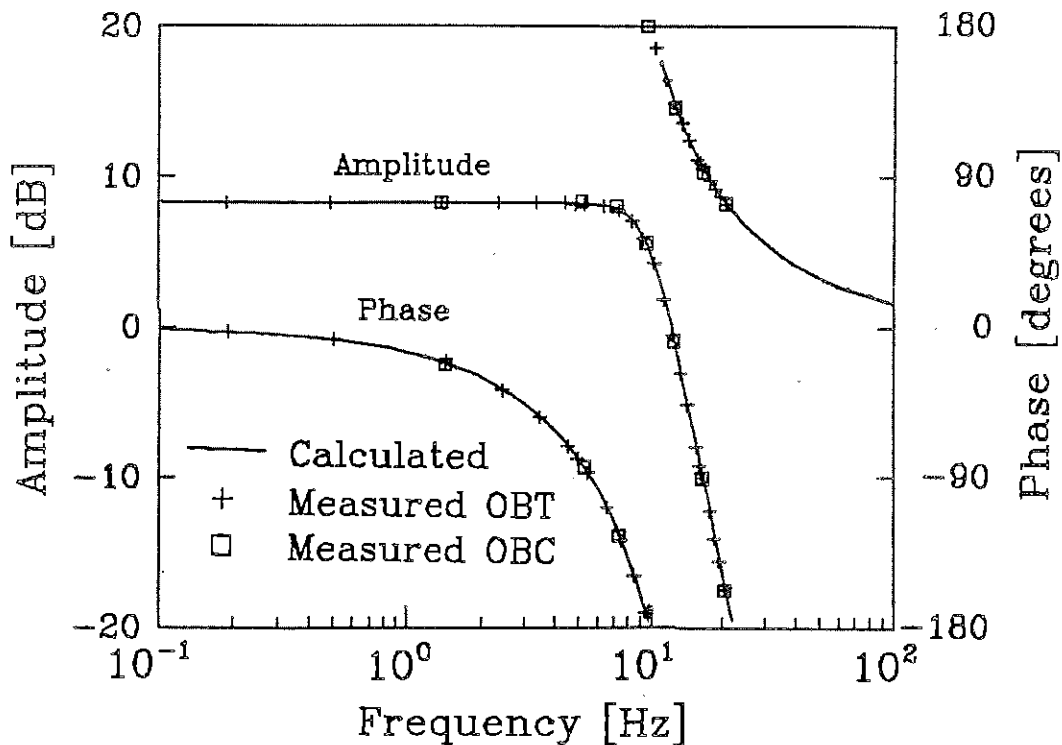


Figure 3-11: Transfer function of the anti-aliasing filters. The normalizing voltage divider (figure 3-10) has not been included here - otherwise the low-frequency amplitude would be =0dB; it is however included in the final OBC-calibration (see below). The accurate measurements were made possible through the use of a Data Precision DATA 6000 spectrum analyser as a digital oscilloscope.

inside the sphere might be predicted from Wait's (1969) results. The homogeneous initial field

$$\underline{B}_0 = \hat{z} B_0 e^{i\omega t} = (\hat{r} \cos \Theta - \hat{\Theta} \sin \Theta) \underline{B}_0 e^{i\omega t}$$

can be represented in free space by a stream function  $\Psi_0 = i\omega\mu_0 B_0 r^2 \cos \Theta$ . Wait's (1969) solution for  $\Psi^e$  (outside) and  $\Psi^i$  (inside the spherical shell) given as a spherical harmonics expansion can be reduced to

$$\Psi^e = A_1 \frac{b}{r} \cos \Theta + \Psi_0 \quad \text{and} \quad \Psi^i = B_1 \frac{r^2}{b^2} \cos \Theta$$

(where  $b$  is the radius of the outer surface) because the coefficients of higher order multipoles are zero in this problem.  $A_1$  and  $B_1$  are determined from the thin sheet boundary conditions

$$E_\phi^e = E_\phi^i \quad E_r^e = E_r^i \quad (B_r^e - B_r^i) / (\mu d) = \sigma E_\phi$$

(where  $d$  is the wall thickness) similar to Wait (1969). It finally results that  $\Psi^i = \Psi_0 / (1 + \alpha)$  or

$$\underline{B}^i = \underline{B}_0 / (1 + \alpha)$$

where the response number  $\alpha = i\omega\mu\sigma(db/3)$ . The magnetic induction inside the spherical shell has its direction preserved - only a decrease in amplitude and a phase shift occur. The calculated transfer function  $1/(1 + \alpha)$  differs however considerably from values measured with a square 1.2m coil as magnetic field source and the OBC-sensor inside the pressure sphere as can be seen in figure 3-12, dashed line.

### Sphere Transfer Function

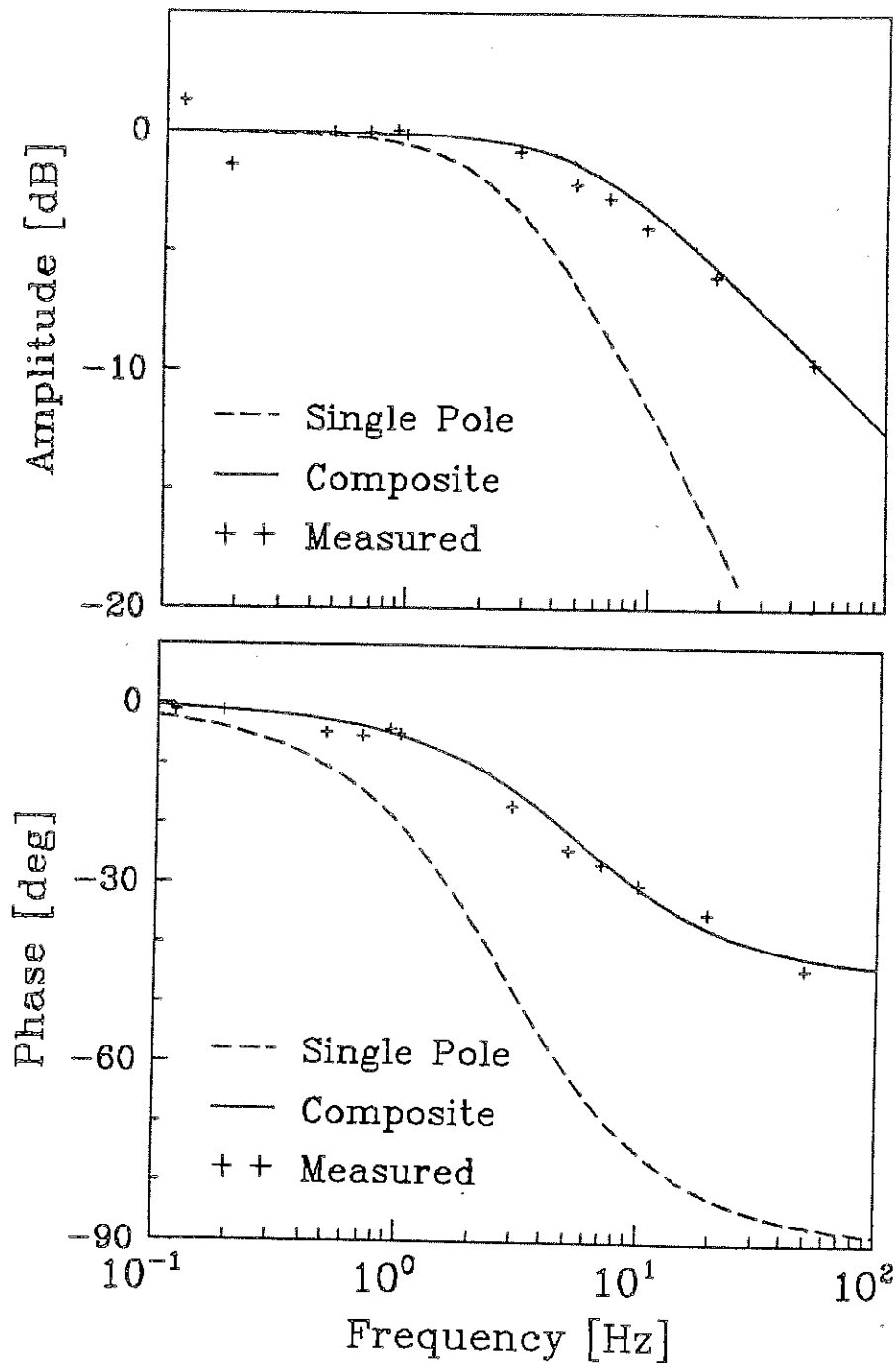


Figure 3-12: Transfer function of the pressure sphere. Dashed:  $\sigma = 19.2$  MS/m,  $a=1$  (single pole); solid:  $\sigma = 9.6$  MS/m,  $a = 0.5$  (sum of multipoles). See text for the meaning of  $\sigma$  and  $a$ .

This may in part be an effect of the slightly inhomogeneous field used as a source or that the thin sheet approximation loses its validity at the high frequency end or that the permeability of the material differs from the assumed permeability of free space  $\mu_0$ . The main causes appear to be the following.

a) The process of spinning the aluminum alloy into a hemisphere may have reduced its conductivity to about 1/2 (inferred from comparing cold rolled and un-treated aluminum in the ASM (1983) tables).

b) The applied and measured field was parallel to the plane of the equatorial midring that insulates the upper from the lower hemisphere. This midring has an anodized surface which is electrically insulating. The longitudinal currents induced by the horizontal field can only cross through six steel bolts holding the hemispheres together. These provide a relatively resistive path due to their small cross section. Closed current loops will consequently be induced in each hemisphere so that the problem requires a full expansion into multipoles and a solution under the additional boundary conditions at the equator. A simple empirical expression serves however the purpose of a transfer function for the data processing:

$$\underline{B}^i = \underline{B}_0 / (1+\alpha)^a$$

An assumed conductivity of half the literature value and  $a=0.5$  give a good approximation to the measured transfer function as can be seen from figure 3-12, solid line.

The temperature decrease from room temperature ( $20^{\circ}\text{C}$ ) to seafloor temperatures ( $2^{\circ}\text{C}$ ) will increase the conductivity of aluminum by about 7% (Küpfmüller, 1973, p. 11/12). The resultant shift of the transfer function by about 7% along the frequency axis is negligible.

If, in a future version of the OBC, the bandwidth was to be expanded to higher frequencies, then the instrument would have to be repackaged into a glass sphere or with the sensor outside the conductive Aluminum sphere in order to prevent high-frequency attenuation.

The product of all transfer functions from the previous paragraphs predicts the recorded voltage  $U$  for a sensed magnetic induction  $B$  at each frequency. This OBC calibration shown in figure 3-13 is accurate to  $\pm 5\%$  in amplitude and  $5^{\circ}$  in phase. The steep phase response above 10 Hz might however cause larger errors there when electronic components change their values at the lowered temperature on the seafloor.



# OBC Calibration

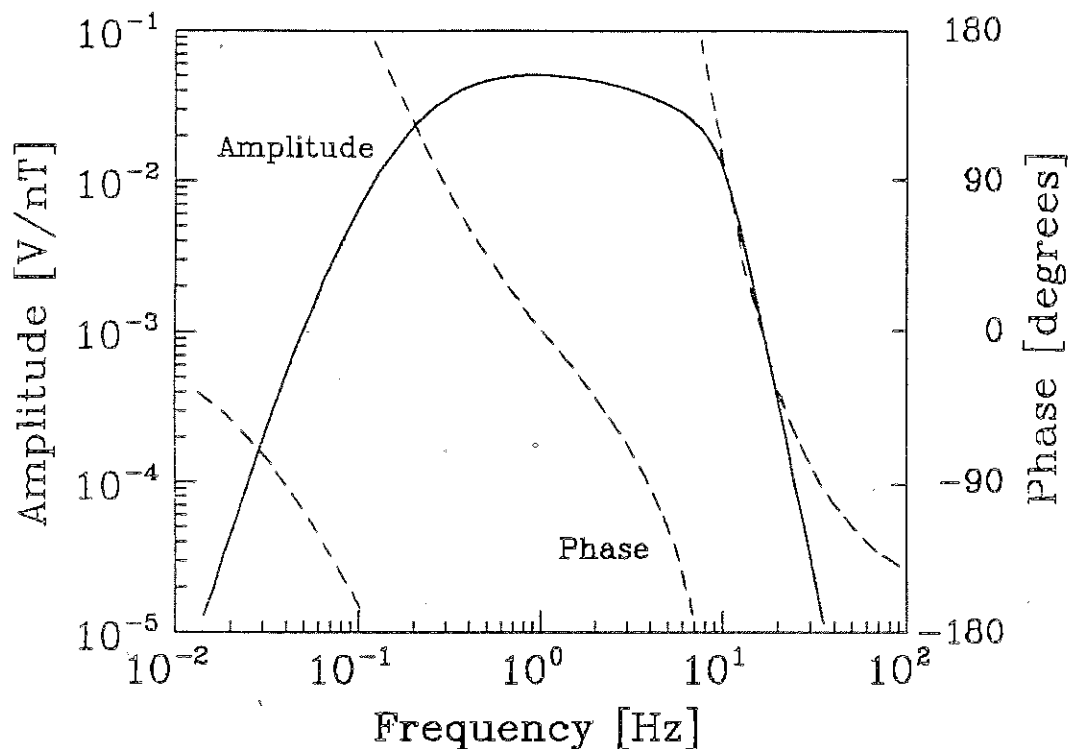


Figure 3-13: Calibration of the ocean bottom induction coil magnetometer (OBC) in recorded voltage  $U$  [V] per sensed magnetic induction  $B$  [nT].

# Synthetic Waveforms

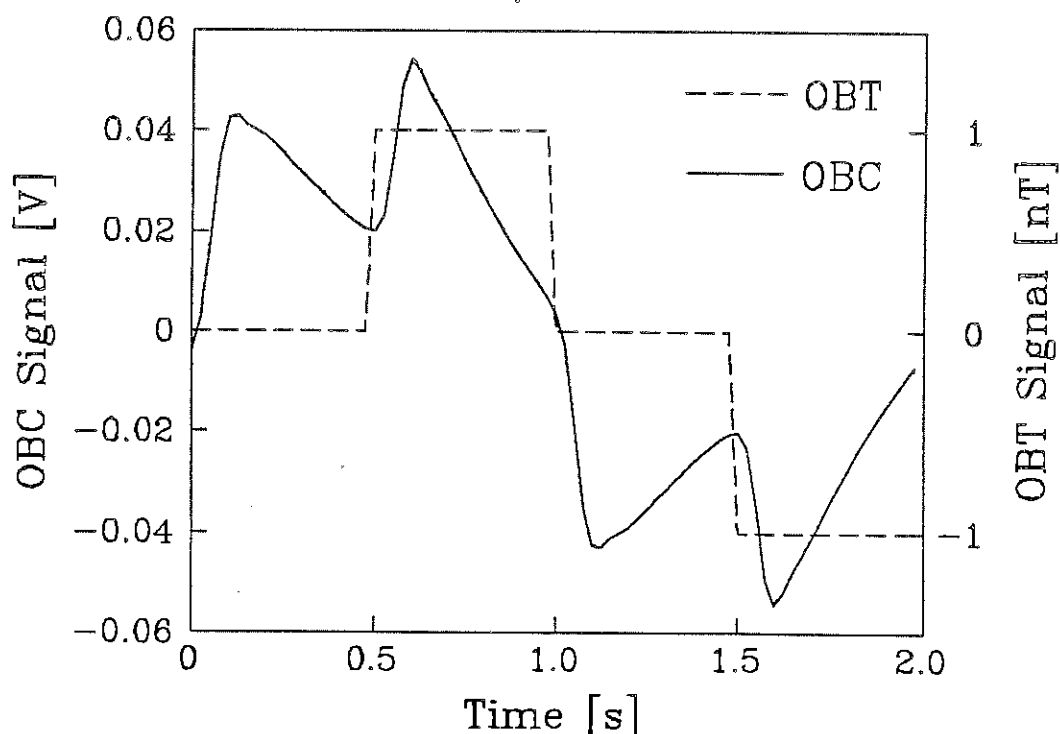


Figure 3-14: Synthetic OBC signal in recorded Volts for a 1 nT magnetic induction with the transmitter (OBT) waveform at the receiver (OBC) location.

The response to the 1 nT transmitter (OBT) signal shown in figure 3-14 can be used for a first shipboard estimate of the measured magnetic induction:  $B[nT] \sim V/0.04$  where V is the height of the first peak in Volts.

### 3.3 SIGNAL TO NOISE RATIO

Among noise sources within the OBC package are the thermal action in the coil resistance and amplifier noise in the first stage. Magnetic fields generated by currents on the microprocessor board appeared negligible. The noise at the output of the first stage may be calculated by replacing in the circuit the coil-emf with

$$\left( \tilde{U}_{nc}^2 + \tilde{U}_{na}^2 \right)^{1/2}$$

and adding a current source  $\tilde{I}_{na}$  across the input terminals of the OPA27 amplifier.  $\tilde{U}_{na}^2 dw$  and  $\tilde{I}_{na}^2 dw$  are the specified amplifier noise power spectral densities and  $\tilde{U}_{nc}^2 dw$  is the thermal noise power spectral density in the coil (see 3.2.1):

$$\tilde{U}_{out}^2 = \left| \frac{Z_F}{R_L + i\omega L} \right|^2 \left( \tilde{U}_{nc}^2 + \tilde{U}_{na}^2 \right) + |Z_F|^2 \tilde{I}_{na}^2$$

where  $Z_F$  is the impedance of the negative feed-back loop. The second term (current noise) will dominate over the first term (voltage noise) at high frequencies. The total noise can only be predicted approximately because the amplifier specifications had to be extrapolated to low frequencies; the results are shown in table 3-1. The equivalent signals are the the output voltage from the OPA27 amplifier due to predicted noise inputs divided by the voltage due to the sensor input. The latter is in turn related to the magnetic induction via the calibration. The "equivalent signals" are therefore the ratios of rms-noise to a unit (1 pT) signal. Integrating the squares of the last column and taking the square root gives an approximate noise level of 3 pT for the 0.5-10 Hz frequency band. Note that most of the noise power appears to be concentrated at the low frequency end.

The 1 mV resolution of the analog to digital converter determines the smallest signal measurable without averaging while its 12 bit range determines the largest measurable signal. Four dynamic ranges result from the four different settings of the variable gain stage. Using the OBC calibration at its plateau (0.3 Hz to 10 Hz) they are expressed as measurable magnetic induction and listed in table 3-2. The total dynamic range of the OBC (0.3 pT -  $\pm 82$  nT) is  $\pm 2^{12} \times 64 \sim \pm 2.6 \times 10^5 \sim \pm 108$  dB. The smallest signal that could be resolved in the OBC-bandwidth (0.3 pT for the

Table 3-1: Predicted instrumental noise.

| Frequency | OPA27 specs                       |                                   | Equivalent Signals         |                            |                          |
|-----------|-----------------------------------|-----------------------------------|----------------------------|----------------------------|--------------------------|
| Hz        | $U_{na}^{rms}$<br>nV/ $\sqrt{Hz}$ | $I_{na}^{rms}$<br>pA/ $\sqrt{Hz}$ | U-noise<br>pT/ $\sqrt{Hz}$ | I-noise<br>pT/ $\sqrt{Hz}$ | total<br>pT/ $\sqrt{Hz}$ |
| 0.5       | 10                                | 9                                 | 2.7                        | 2.4                        | 3.6                      |
| 5         | 4.3                               | 2.2                               | 0.1                        | 0.2                        | 0.2                      |
| 10        | 3.8                               | 1.7                               | 0.05                       | 0.1                        | 0.1                      |

Thermal noise  $U_{nc}^{rms} = 1.6 \text{ nV/Hz}^{1/2}$  at 275 K ( $\approx 2^\circ\text{C}$ )

Table 3-2: Digitizing noise and dynamic range at the plateau of the OBC-calibration. LSB and HSB mean least and highest significant bit, respectively.

| gain | 1        | 4        | 16      | 64        |    |
|------|----------|----------|---------|-----------|----|
| LSB  | 20       | 5        | 1.3     | 0.3       | pT |
| HSB  | $\pm 82$ | $\pm 20$ | $\pm 5$ | $\pm 1.3$ | nT |

highest gain setting) is thus smaller than the 3 pT noise level estimated above. A higher resolution is therefore obtainable through signal stacking and averaging. Stacking the periodic signal improves the signal to white, uncorrelated noise ratio by  $N^{1/2}$  ( $\sim 20$  for the ALVIN-data) where  $N$  ( $=393$ ) is the number of sweeps that have been averaged to obtain one stack (appendix A).

Several sources of instrumental noise not discussed yet may be identified from the ALVIN-data:

The switch at the input to the computer module (figure 3-10) was closed by the CPU only during the measurements. At idling times the open switch caused the charging of capacitors  $C_{34}$  at the output from the amplifiers (figure 3-8,  $R_{341} = \infty$  in the old design, was changed to 2 M $\Omega$  for the October 1984 Inlet cruise). Figure 3-15 shows what happened at the start of each 15 min measuring cycle during the August 1984 ALVIN cruise. The time constant of the exponential decay (3.9s) as obtained from a log-lin plot corresponds to an  $RC = 5\mu F * 0.8M\Omega$  circuit which supports the above explanation.

The short time for development resulted in another source of noise shown in figure 3-16. Every other channel 1 sample (dashed line) is zero indicating that one of the

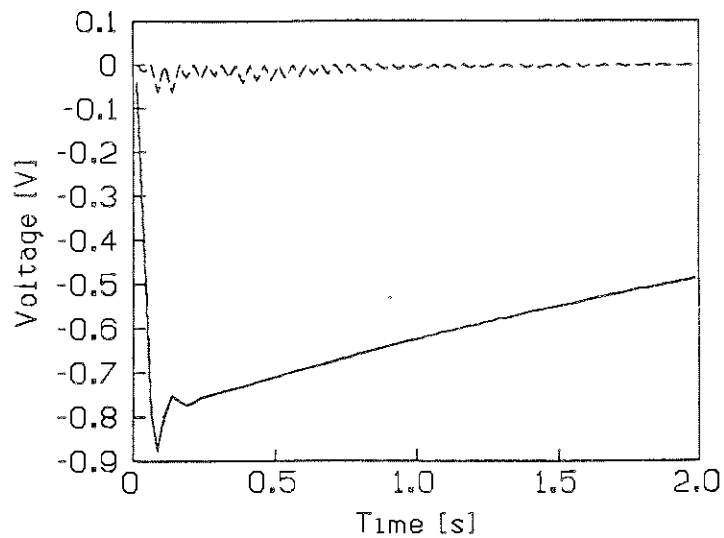


Figure 3-15: Un-calibrated single sweep (stack #18) recorded by the OBC with the OBT turned off during the ALVIN cruise. It clearly shows the exponential discharge of the capacitors  $C_3$  across the input resistance of the computer module. The dashed line shows channel 1 that had intermittent black-outs in the analog-to-digital converters and did not produce useful data.

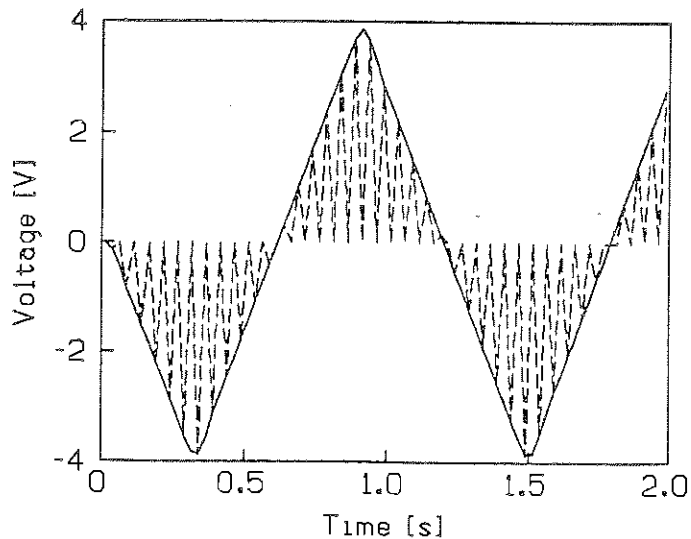
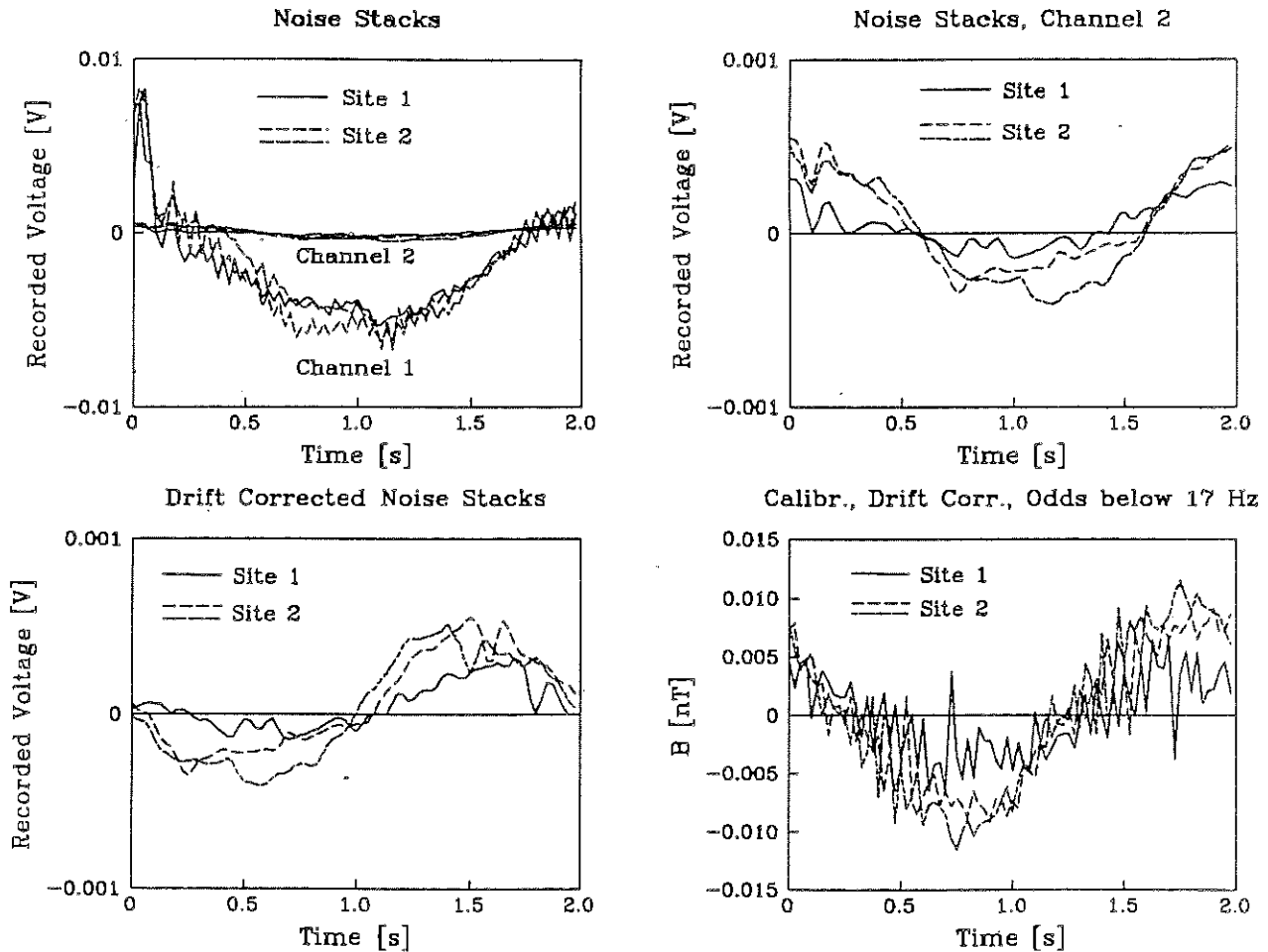


Figure 3-16: Single OBC-sweep (stack #1) with internal calibration triangle showing electronic problems in the channel 1 (dashed) analog to digital converters.

interlacing 20 Hz analog to digital converters became damaged during the survey. Only a complete redesign for the October survey avoided this inherent problem. The effect was intermittent so that part of the channel 1 data looked reasonable but none of it was used for interpretation.

The noise stacks shown in figure 3-17a were recorded during the ALVIN-cruise with the transmitter turned off (site 1 is the near transmitter site, site 2 the far one). After magnifying the useful channel 2 data in figure 3-17b a short 5 Hz oscillation over 0.25 mV appears near the beginning of all three time series. Magnifying this by the number of stacks gives about 0.1V which is just the size of the oscillation that occurs once at the beginning of a measurement cycle as can be seen in figure 3-15. It might thus be connected to the discharging capacitor discussed above. Figure 3-17c shows the noise stacks after they were shifted along the time axis in order to compensate for the frequency offset between OBC-clock and OBT-clock. There appears to be a 0.5 Hz signal just opposite to the polarity of the OBT which might imply some action at the OBT that was supposed to be turned off. This would however contradict the observation that the "signal" is smaller at the near site 1 than at the far site 2. On the other hand the tidal water currents appeared stronger at the far site 2 (chapter 4). Although any further speculation might be futile I have



**Figure 3-17:** Stacked (397 sweeps) OBC measurements with the transmitter (OBT) turned off during the ALVIN-cruise (stacks #17, #30, #42). (a) upper left: including the bad channel 1 data, (b) upper right: channel 2 singled out, (c) lower left: corrected for the differential drift between the OBC-clock and the OBT-clock, (d) lower right: calibrated in frequency domain and inverse transformed using only odd harmonics below 17 Hz.



calculated and displayed in figure 3-17d the magnetic induction at the OBC by calibrating the drift corrected "signal".

It should also be noted that the electronic problems with channel 1 might have caused part of the noise observed in the "clean" channel 2. Figure 3-18 shows how the channel 1 data quality deteriorated from the start (3-18a) towards the middle of the survey (3-18b) (dashed lines). Along with this a) the first peak in the channel 2 record appears to become cut off, b) the small oscillation at the start of the stacking window disappears and c) the record becomes more symmetrical about zero voltage. Such disturbances may be the reason that the even harmonics of 0.5 Hz of the power spectral density (figure 3-19) - although not contained in the 0.5 Hz OBT-signal - stand out above the measured noise (solid lines, same data as discussed in figure 3-17). Here and in the following only channel 2 data are used but it should be remembered that even they are not "clean".

The same selection of recorded data that was used for the previous figure 3-19 have been calibrated using the OBC transfer function. Their power spectral densities are re-plotted in figure 3-20 together with the instrumental noise predicted above and with horizontal magnetic noise at 2 km water depth (labeled "external") taken from Chave and Cox

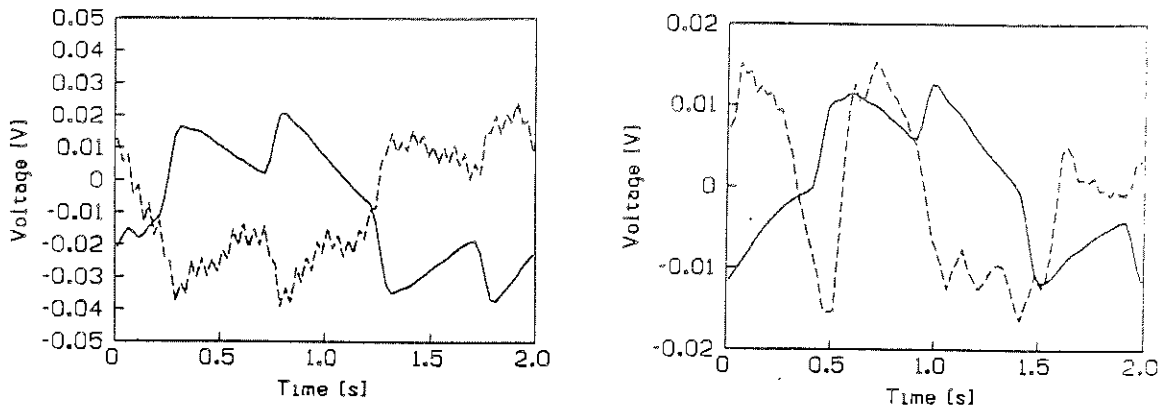


Figure 3-18: Signal records from the ALVIN-cruise: (a) left: near the start of the survey (stack #10), (b) right: towards the middle (stack #19). Dashed: channel 1, solid: channel 2.

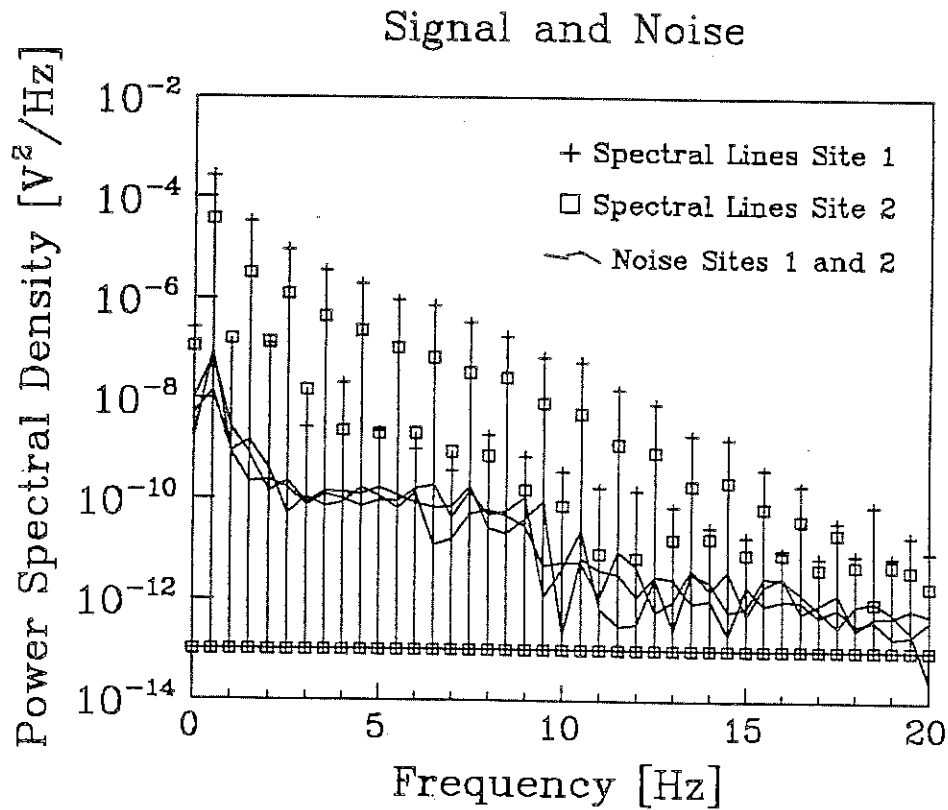
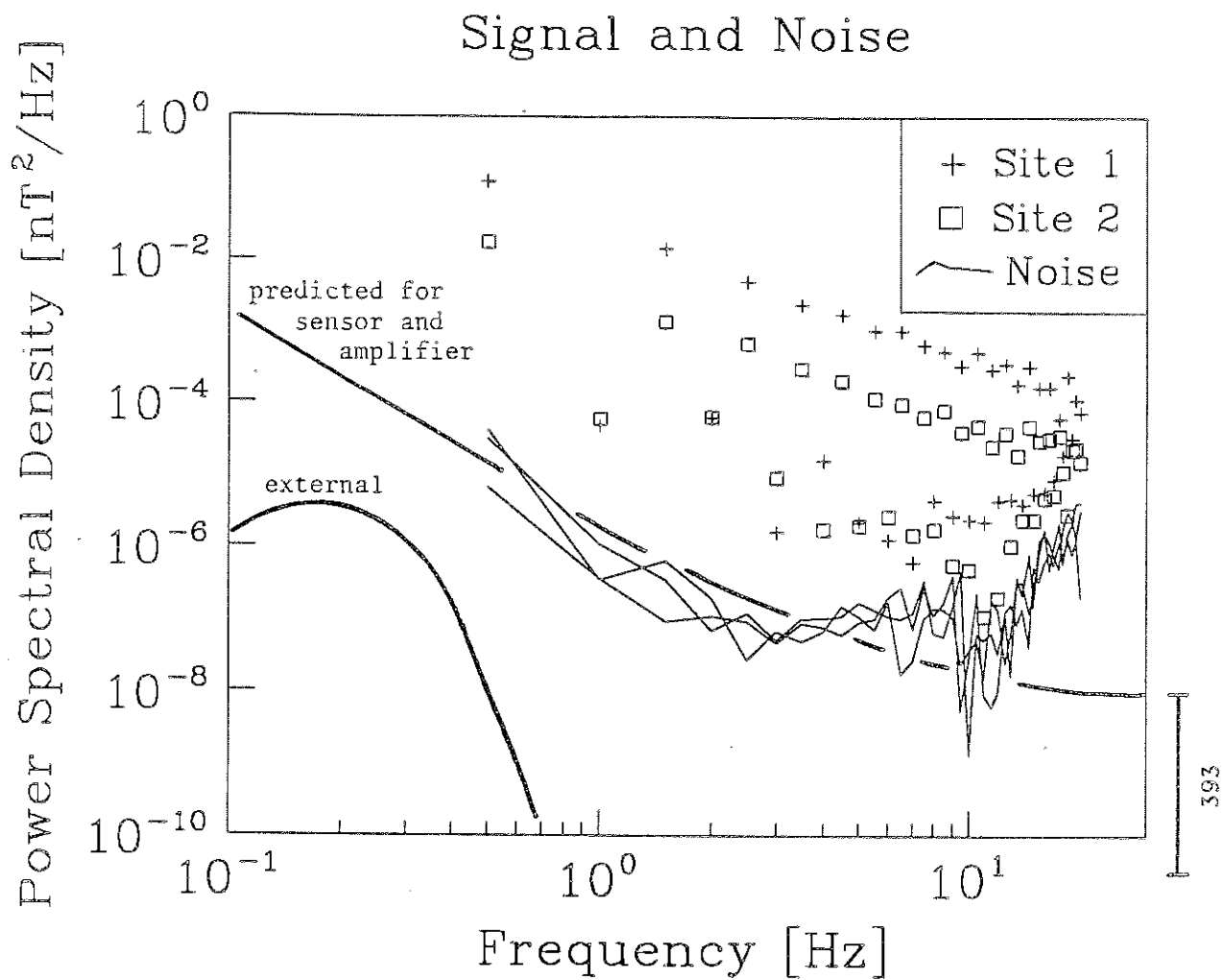


Figure 3-19: The power spectral density of the recorded voltage (signal stacks #14, #23; noise stacks #17, #30, #42) calculated according to appendix A.



**Figure 3-20:** The power spectral density of the calibrated signal stacks #14 (site 1), #23 (site 2) and noise stacks #17 (site 1) and #30, #42 (site 2). The additional noise information has not been corrected for the stacking process. "External" noise after Chave and Cox, 1982.

(1982). The stacking process has obviously reduced the measured noise below the predicted noise. The ratio of signal to measured rms noise between 0.5 Hz and 10 Hz ranges from 20 to 100 for site 2 and from 60 to 300 for site 1 (square root of the distance between measured points and curves in the figure).

#### 4. SURVEY AND RESULTS

The recent discovery of metalliferous, high-temperature hydrothermal vents and accompanying sulphide accumulations offshore from the Canada - United States of America boundary triggered an increased scientific activity on the Northern Juan de Fuca Ridge (Schabas, 1983). A "workshop to discuss future multidisciplinary research on seafloor hydrothermal sulphide deposits in the Juan de Fuca - Explorer Ridge areas of Canada" was held in May, 1983 at the Pacific Geoscience Centre in Sidney, British Columbia. It attracted the leading scientists of the field from the U.S., France and Canada. The contacts to U.S. researchers established there eventually resulted in an invitation to the MOSES-group early in 1984 to participate in an ALVIN-dive program that was to be conducted at the northern end of the Juan de Fuca Ridge in August/September 1984.

The modifications and new developments in the MINI-MOSES instrumentation (chapter 3) were accomplished within six months including the pressure testing of the spheres as required by ALVIN-safety regulations. Dr. Lawrie K. Law, Mike N. Bone and I participated in the survey. Their enthusiasm and 24 hour efforts as well as the tremendous support from captain P. Howland and the crew of the USS ATLANTIS II during deployment, from the pilots and

scientists onboard ALVIN, from captain K. Palfry and the crew of the USS WYCOMA at recovery, made it possible to overcome the considerable logistic problems of the experiment.

#### 4.1 GEOLOGICAL SETTING

The survey was conducted in 2.2 km deep water in the central valley of the Endeavour Segment of the Northern Juan de Fuca Ridge. The inset in the location map (figure 4-1a) shows the MERGE (Multidisciplinary Endeavour Ridge Geo Expedition) study area and is redrawn to scale in figure 4-1b. The geological features shown were mapped on four reconnaissance dives indicating that the basalts on the valley floor are roughly the same age (as indicated by sediment cover) as the basalts on the flanking ridges. Fissuring occurs only in the valley floor and evolves into normally faulted blocks with increasing throw as the valley flanks are approached. Hydrothermal activity was located in three areas within a region 150m x 500m and appeared to be situated on fault-bounded ridges that paralleled the general ridge strike. Eleven dives were devoted to detailed mapping and sampling of a hydrothermal vent field (250m x 150m, indicated by the

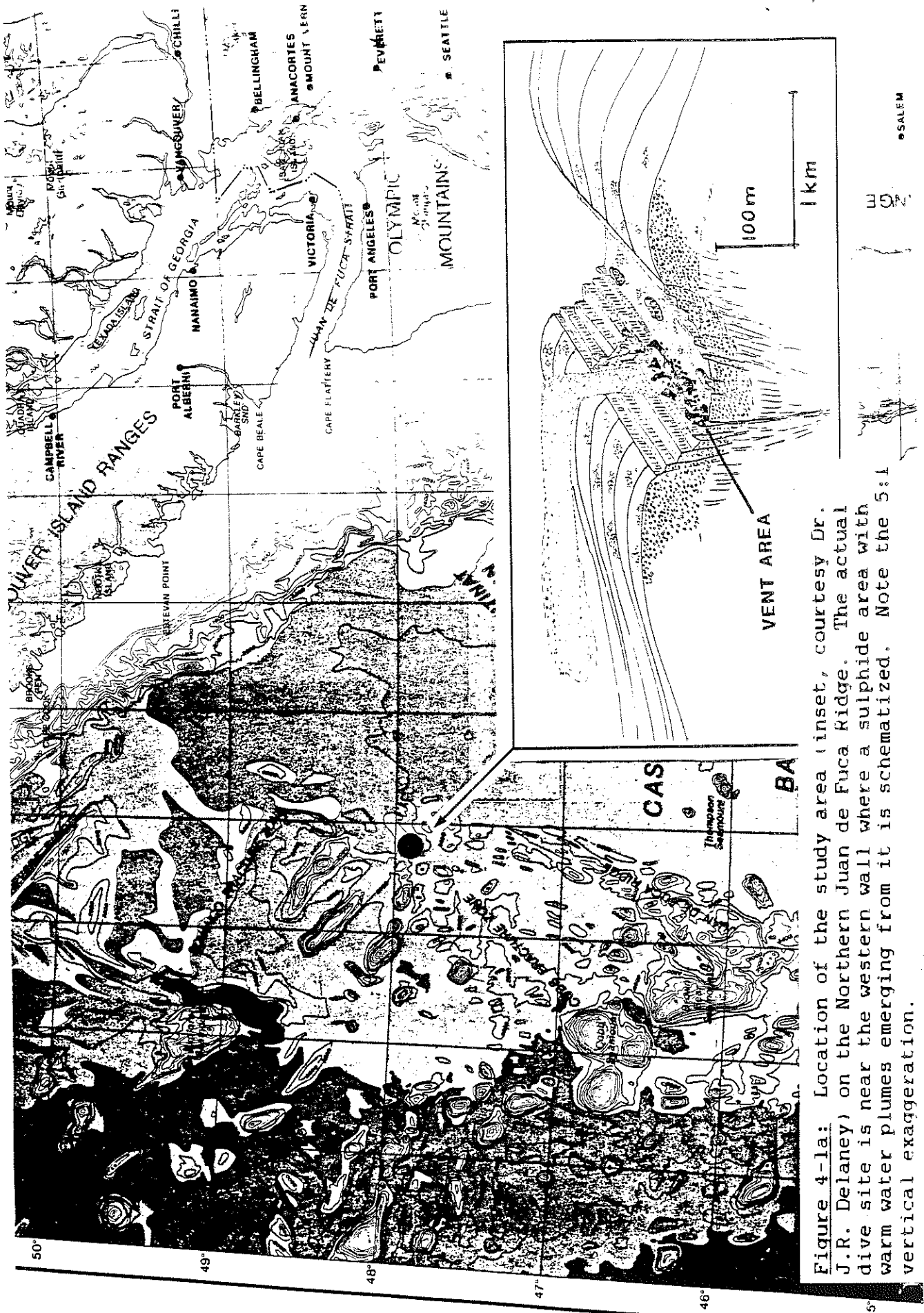


Figure 4-1a: Location of the study area (inset, courtesy Dr. J.R. Delaney) on the Northern Juan de Fuca Ridge. The actual dive site is near the western wall where a sulphide area with warm water plumes emerging from it is schematized. Note the 5:1 vertical exaggeration.

## STUDY AREA

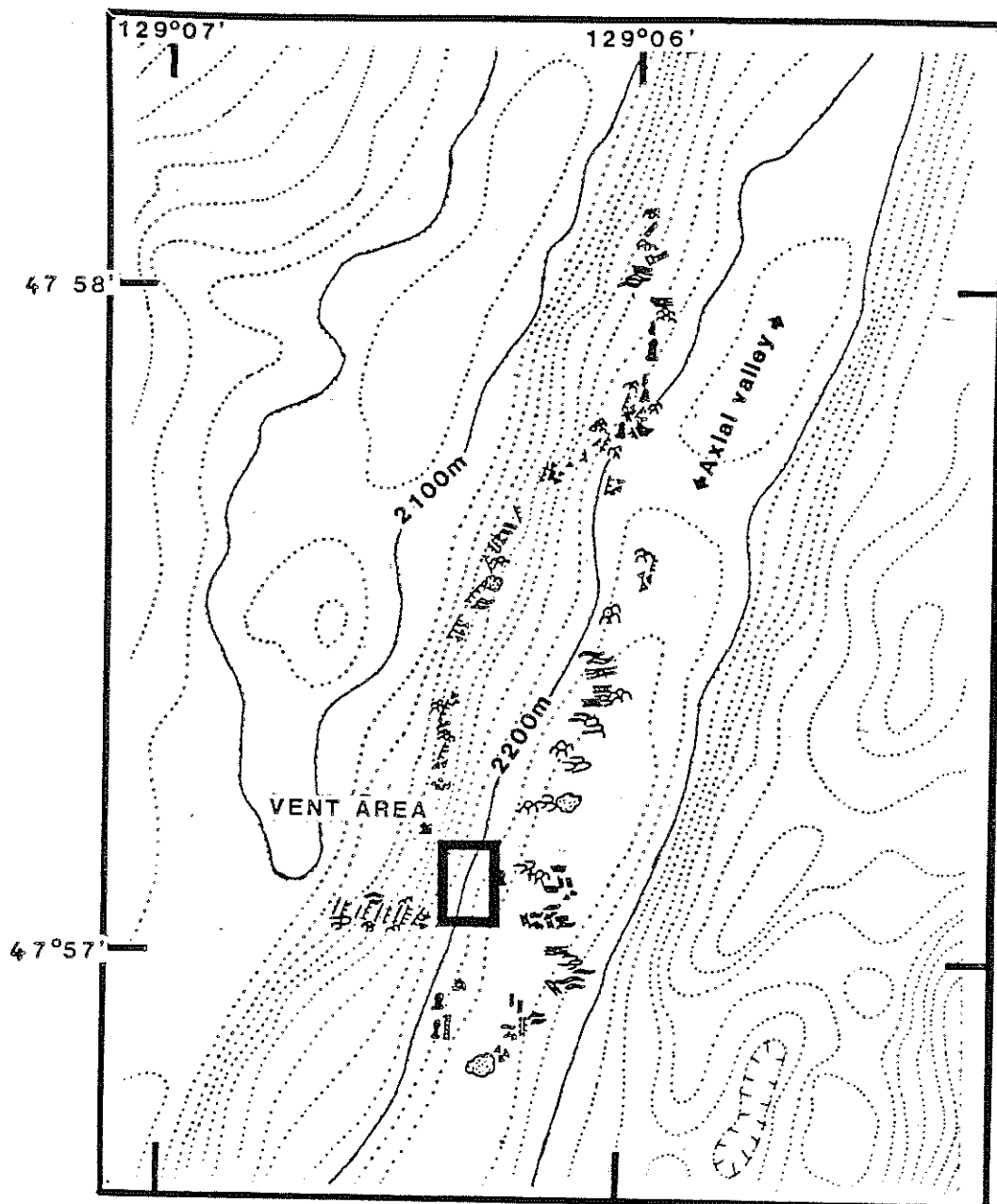


Figure 4-1b: Plan view of the study area (preliminary, from cruise report, approximately the same area as shown on the inset in fig. 4a). The dive site is indicated by the box marked "vent area" (approximately 250m x 150m).

Following Page:

Figure 4-2: Section of the preliminary geological map of the vent area (about half the box in figure 4-1b) with the location of the OBC marked R (for "receiver") and the two consecutive OBT sites marked T<sub>1</sub>, T<sub>2</sub> (for "transmitter") with water depths. The nearby hydrothermally active sulphide area is delineated by a dashed line. Depths are given in the legend. Placing the instruments relative to the geological features might have reduced the  $\pm 10$ m uncertainty in horizontal position somewhat.



# Key

INACTIVE SULFIDE STRUCTURE

HYDROTHERMAL ACTIVITY:

BLACK SMOKER

CASTLE-LIKE STRUCTURE

TUBEWORMS/LOW-TEMP. VENT

MONTRONITE

POOR VISIBILITY

FISSURE

SCARP

BASALT:

PILLOW

LOBATE FLOW

SHEET FLOW

COLLAPSE STRUCTURE

TALUS

SEDIMENT COVER:

HEAVY

MEDIUM

LIGHT

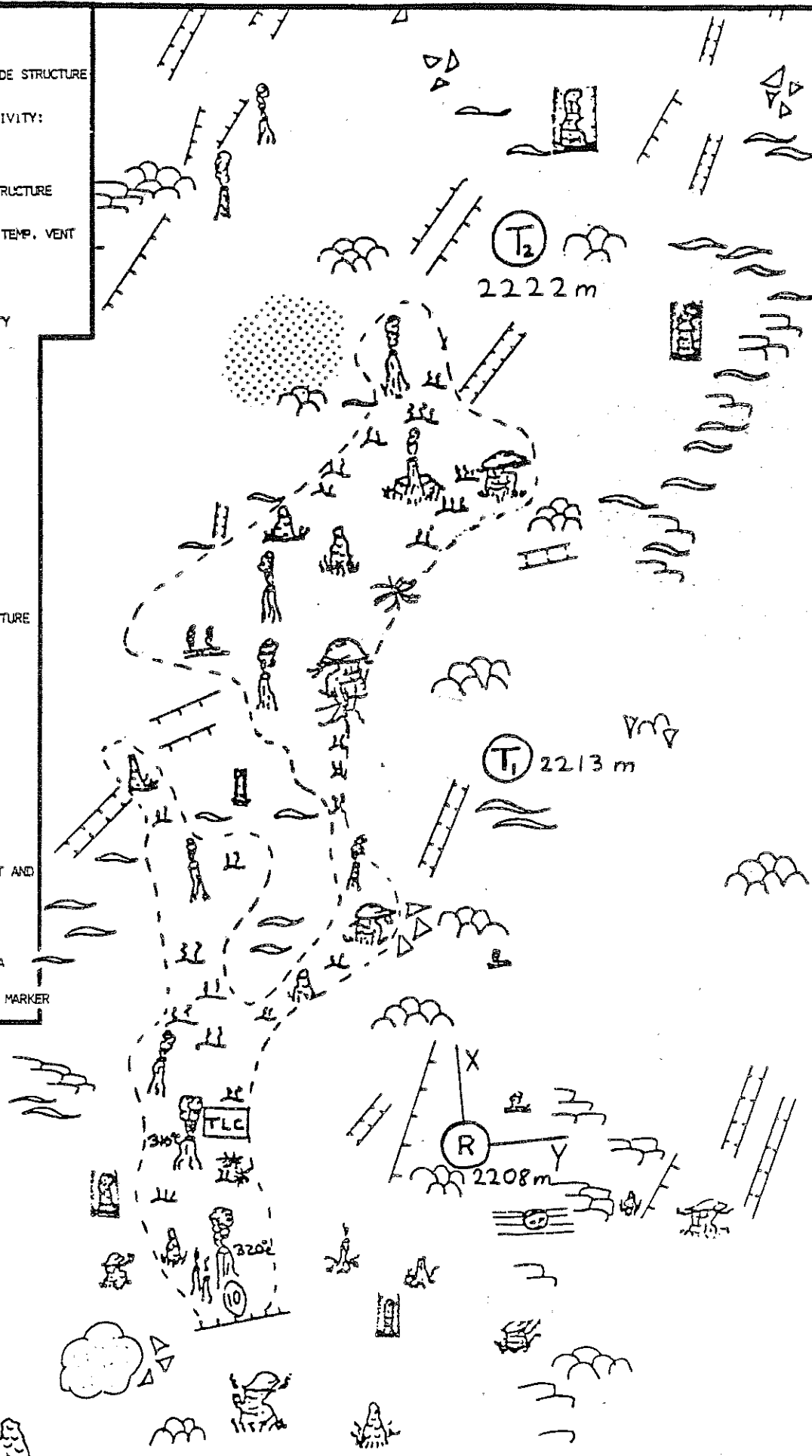
(R) RECEIVER, (T<sub>1</sub>) FIRST AND

(T<sub>2</sub>) SECOND TRANSMITTER LOCATIONS

TLC TIME LAPSE CAMERA

○ PERMANENT SAMPLE MARKER

10m



box "vent area" in figure 4-1b) which displayed all possible types of hydrothermal activity (see figure 4-2): fossil sulphide structures, warm water emanating from fractured basalt at the periphery, low temperature vents (white smokers) with unusual biological communities, sulphide-depositing chimneys situated on bare basalt, and high temperature vents (black smokers). Chimneys and vents displayed a wide range of morphologies, from single small edifices (about one meter high), to complex, castle-like structures (20m high) with multiple vent openings.

The OBC ("R" in figure 4-2) and the two consecutive OBT sites ("T<sub>1</sub>" and "T<sub>2</sub>") are located on basalts along a vent field (delineated by the dashed line) in an area that was multiply covered with ALVIN dive tracks.

## 4.2 EXPERIMENTAL PROCEDURE

This experiment was a trial of a new technique in a frontier environment, conducted as a cooperation between two geographically separated research groups. Therefore, it required careful preparation and planning. The Toronto-built OBC and OBT microprocessor units were interfaced with

the commandable anchor release units at the Pacific Geoscience Centre and with a desk-top computer later used to download the survey instructions. An interview was arranged with the submersible crew to plan the use of dive time and to obtain final advice on deployment details. We boarded the USS WECOMA in Seattle (figures 4-3a,b) which sailed on August 30, 1984 to rendezvous on site with the support vessel USS ATLANTIS II of the deep submersible ALVIN.

Being a trial of a new technique, our experiment was allocated parts of two of the eighteen dives, but only at the lowest priority. In order to avoid wasting ALVIN's precious bottom-time in the search for our instruments, we had to deploy the instruments from the ATLANTIS II because the latter could be positioned relative to the same sea bottom acoustic transponder net that was used for ALVIN's navigation. Our equipment was therefore transferred at sea from the WECOMA to the ATLANTIS II (figures 4-3c,d). The OBC and OBT were assembled in their deployment packages (figure 4-3e) and the survey instructions downloaded from a floppy disk file. The two packages were attached to each other with a pull-pin mechanism so that they could be lowered together at the end of a long cable. They were released from an acoustic command release hook when the desired position and depth (100 m above bottom) was reached.

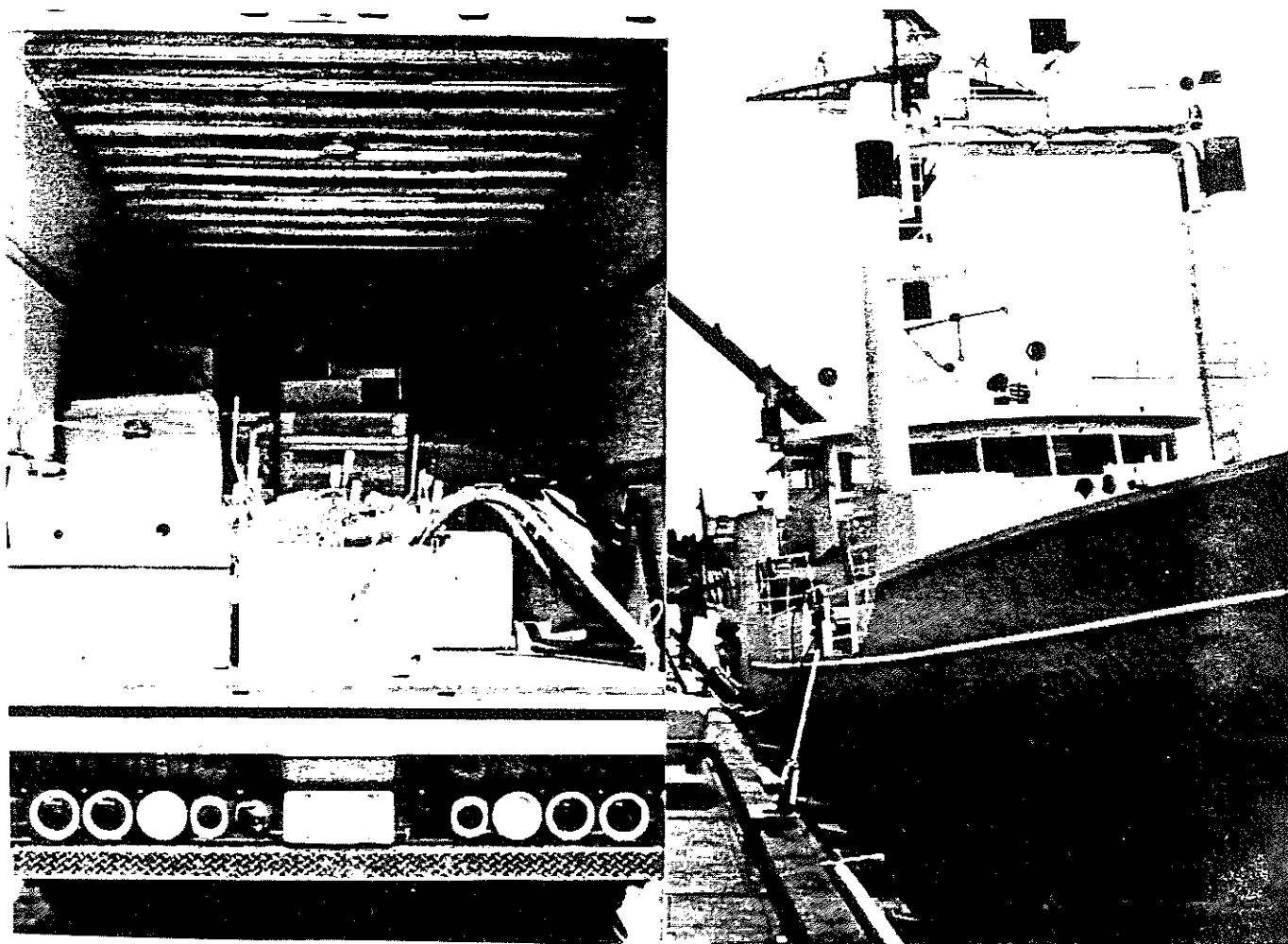


Figure 4-3: Logistics involved in the survey. (a) upper left: the 5m<sup>3</sup> equipment, (b) upper right: USS WECOMA docked in front of the University of Washington at Seattle, (c) lower: equipment transfer between USS WECOMA and USS ATLANTIS II in 4m swell.

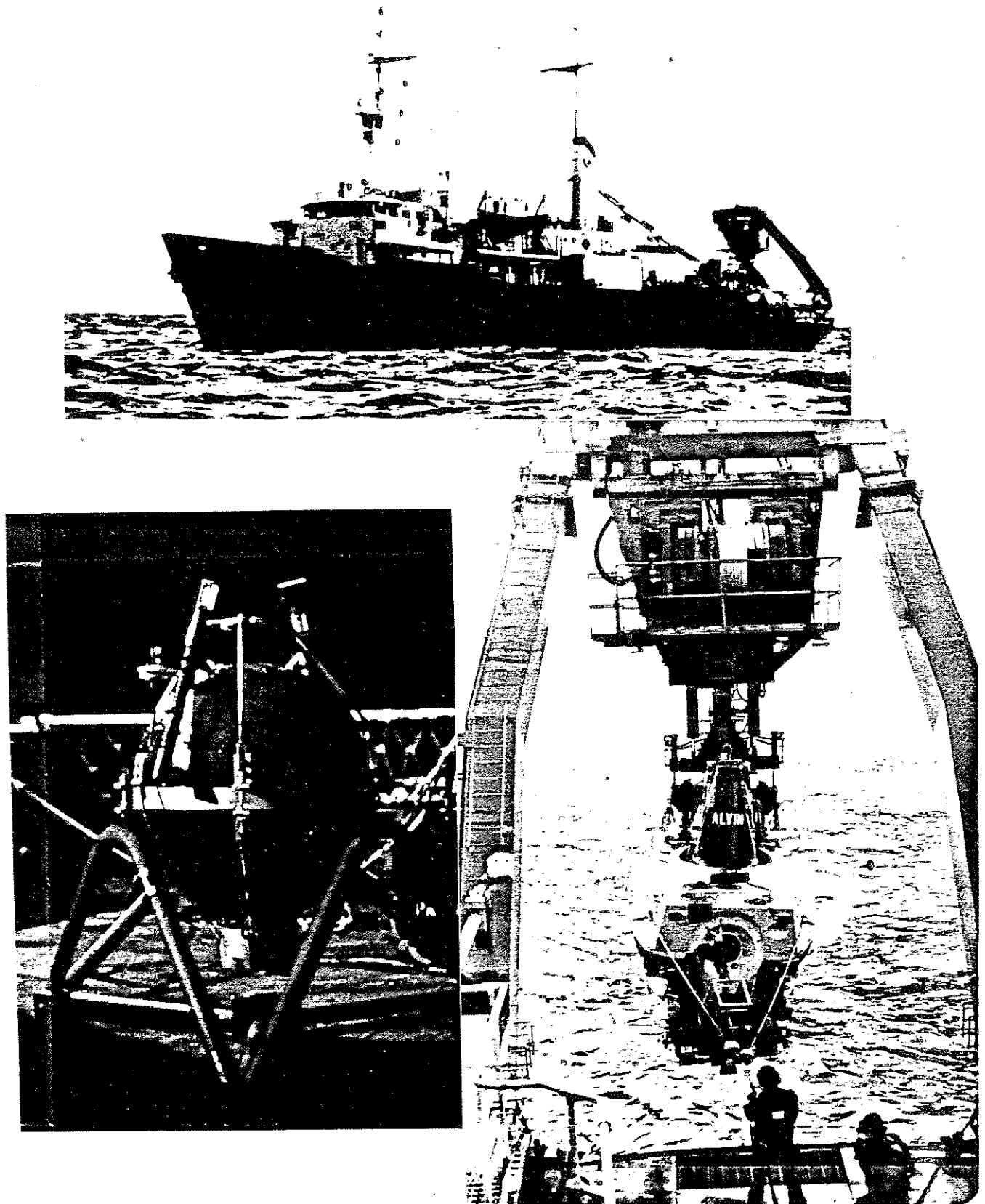


Figure 4-3: continued, (d) upper: USS ATLANTIS II on site, (e) lower left: The OBC assembled in pressure sphere and anchor with release (bottom of the sphere) and strobe-light and radio-beacon (top) a few hours before deployment, (f) lower right: deploying ALVIN the next morning.

Although ALVIN has proven a versatile instrument for many deep sea operations, my experiment was noted as a new type of usage and was monitored for similar tasks in the future. The weight under water of the OBC/OBT had been adjusted to about 10 kg by the number of lead plates attached to the anchor. ALVIN was thus able to lift the instruments off the bottom without raising its own buoyancy through much energy-consuming pumping. This made the rapid moves of 30 to 45 minutes possible and also prolonged bottom-time through energy conservation. Based on pre-cruise estimates of this timing, I planned to have the initial positions and one extra transmitter site occupied on the first dive. It would then take about half of another dive to move the transmitter three times so that a total of five transmitter-receiver separations could be realized in two half-dives.

The instruments had been instructed to start each day with an internal calibration followed by 15 min noise stacking (OBT not transmitting). During ALVIN's bottom time six 15 min cycles of signal stacking were performed starting at the full hour. All measurements were interlaced with single noise sweeps. Repeating this pattern every day gave the necessary flexibility for moving our instruments whenever it was convenient within a three-day time window of the dive-program.

ALVIN with Dr. Margaret Leinen, Dr. Gary Taghon and pilot Skip Glesson onboard (dive 1446, September 2) was launched shortly after our deployment operation (figure 4-3f) and located the OBC/OBT package (figure 4-3g). The OBC and the OBT were separated by pulling the pin from the pull-pin connection, and each instrument was moved individually to a suitable initial position. The time spent on an initial unsuccessful attempt to move the entire OBC/OBT package preempted moving the transmitter to a second site on the first dive. The following day (dive 1447, September 3) Dr. Ross McDuff, Dr. Meg Tivey and chief pilot Dudley Foster located the transmitter and moved it to its second site. The priorities were then shifted to a different experiment so that no more transmitter sites could be occupied.

We transferred back to USS WECOMA with our equipment on September 2 and, on September 4, recovered the instruments late at night and dumped the recorded data onto a floppy disk a few hours before they were erased due to the fading battery voltages. The recovery took several hours because the packages were poorly balanced so that the strobe-light and radio-beacon could only be detected when lifted above the waterline through the wave action.

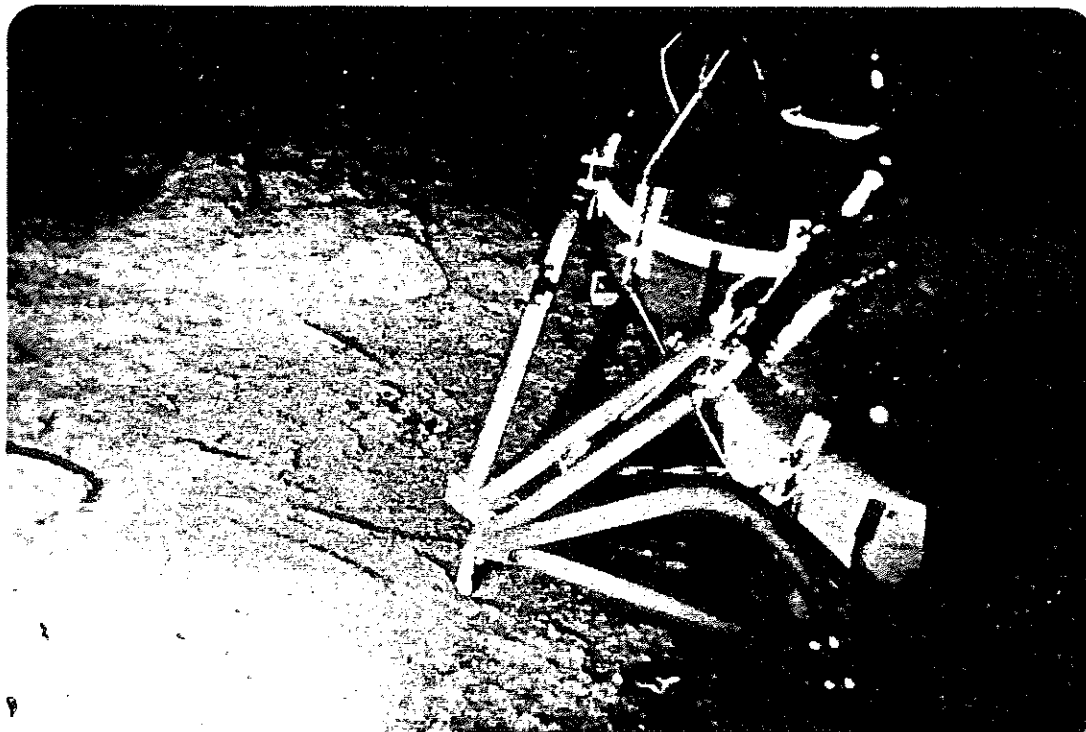


Figure 4-3: continued, (g) the OBT/OBC package on the seafloor before it was separated into two individual instruments.



### 4.3 DATA PROCESSING

The data were transferred from the floppy disk onto the Department of Physics VAX 11 and plotted for a first visual inspection. Some features of the data have already been discussed in chapters 2 and 3. The example of raw data records in figure 4-4 shows transmitted (right column, negative current shown positive) and received (left column) waveforms for site 1 (first row) and site 2 (second row). The X (channel 1) and Y (channel 2) sensors were oriented relative to strobe-light and radio-beacon before deployment and the bearing of strobe and beacon recorded by the observers in the submersible. The labels X and Y in figure 4-4 correspond to the same labels in the location map (figure 4-2). The Y-sensor happened to be almost perpendicular to the direction to both transmitter stations and should therefore receive most of the signal amplitude. It is clear that we were lucky to have this channel working even though the X-channel was damaged. The X-data will not be used in the further processing.

The visual inspection of all data records showed that the amplitude did not remain constant at each site (amplitude drift). A considerable time-shift (phase drift) can also be recognized when comparing the Y-data of stack #14 (figure 4-4) with the Y-data of stack #23 that was

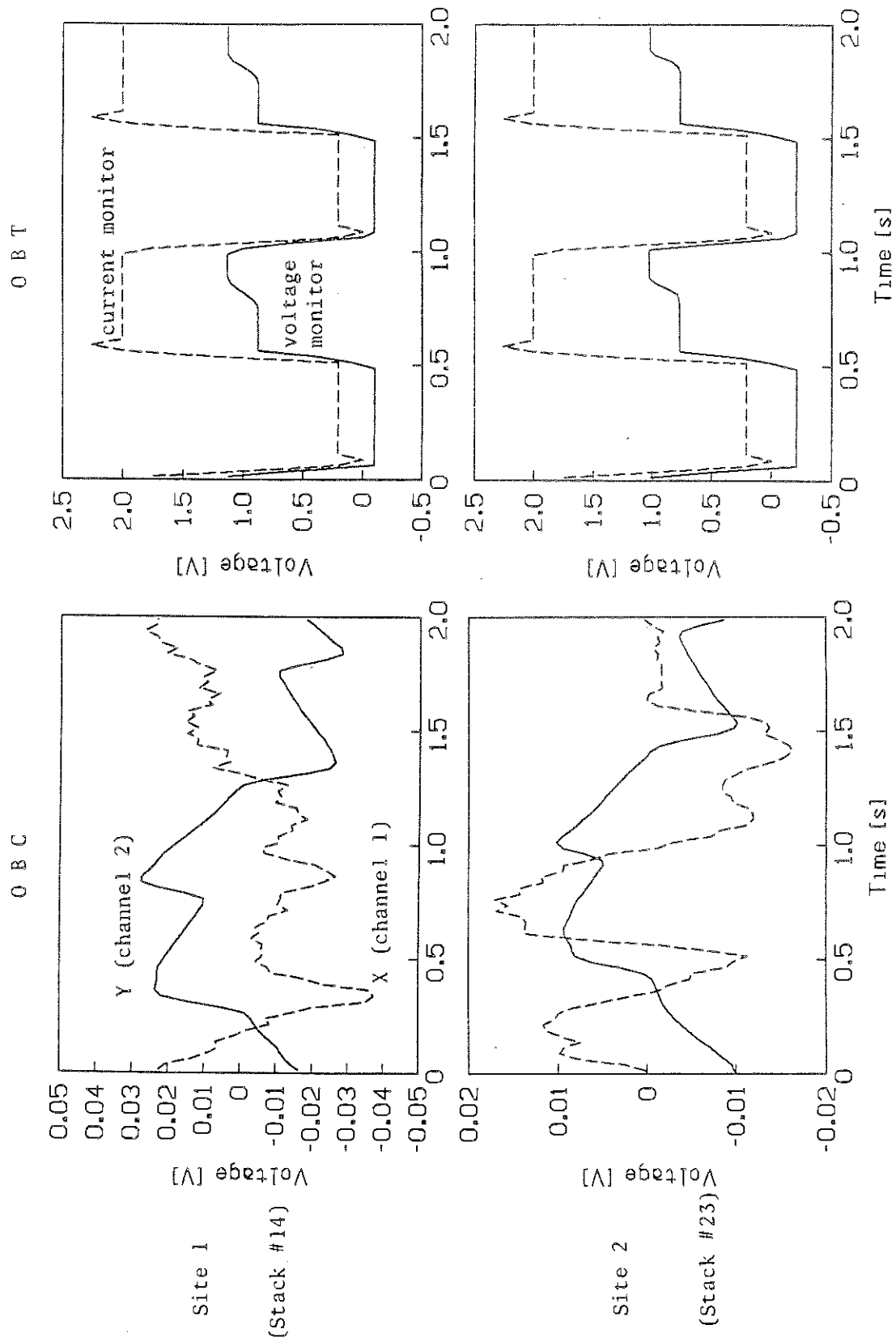
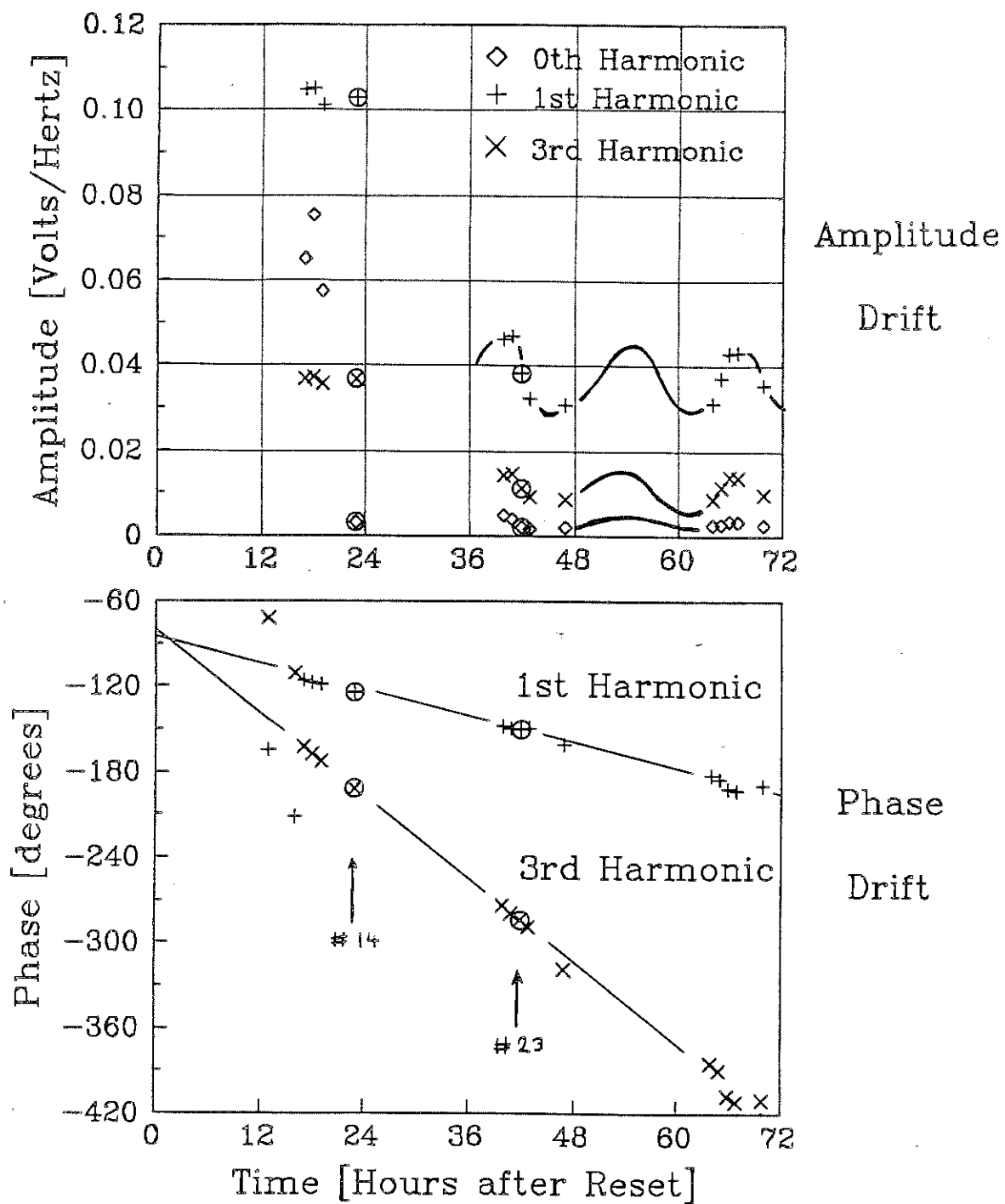


Figure 4-4: Raw data (recorded voltage) examples: OBC (left column) and OBT (right) waveforms for OBT site 1 (first row) and site 2 (second). x,y corresponds to figure 4-2. Each channel consists of 80 samples spaced 0.025 s and averaged 393 times.

recorded about 20 hours later. In figure 4-5 the zero'th harmonic and the first two signal lines were extracted from the Fourier transforms of each of the 14 signal records (the first two had to be discarded because OBC and OBT had not been separated yet) and plotted versus the time when the records were taken. The amplitude drift was most likely caused by tidal water currents that moved the transmitter bipole back and forth. The source wire would have to be tilted by 1 m in 100 m in order to produce the  $\pm 30\%$  variation in the signal amplitude (cf. section 2.2). Using only stack #14 and #23 should avoid the problem because there the wire would just be passing through the vertical.

The phase drift in figure 4-5 can be explained with a 2.3 ppm (parts per million) clock-frequency offset between OBT and OBC: the OBC-clock was faster than the OBT-clock. This value is however not yet accurate enough if phase differences were to be interpreted in terms of induction in an ocean-seafloor model. A more accurate estimate can be obtained during the data processing and only the final results will be corrected for drift (see below).

The OBC data from figure 4-4 (Y-component only) have been Fourier transformed (appendix A) to obtain the spectral densities shown in figure 4-6a,b. The signal lines (odd harmonics of 0.5 Hz) have clearly a larger amplitude than



**Figure 4-5:** Drift curves (Y-component data only) of Fourier amplitude and phase versus survey time. 0 hours corresponds to local 20:15h on September 1st, 1984. Stacks #14 and #23 are highlighted by circles. The interpolating lines in the amplitude drift data have a typical tidal period. The straight lines through the phase data both correspond to 2.3 ppm relative clock-frequency offset between OBT and OBC.

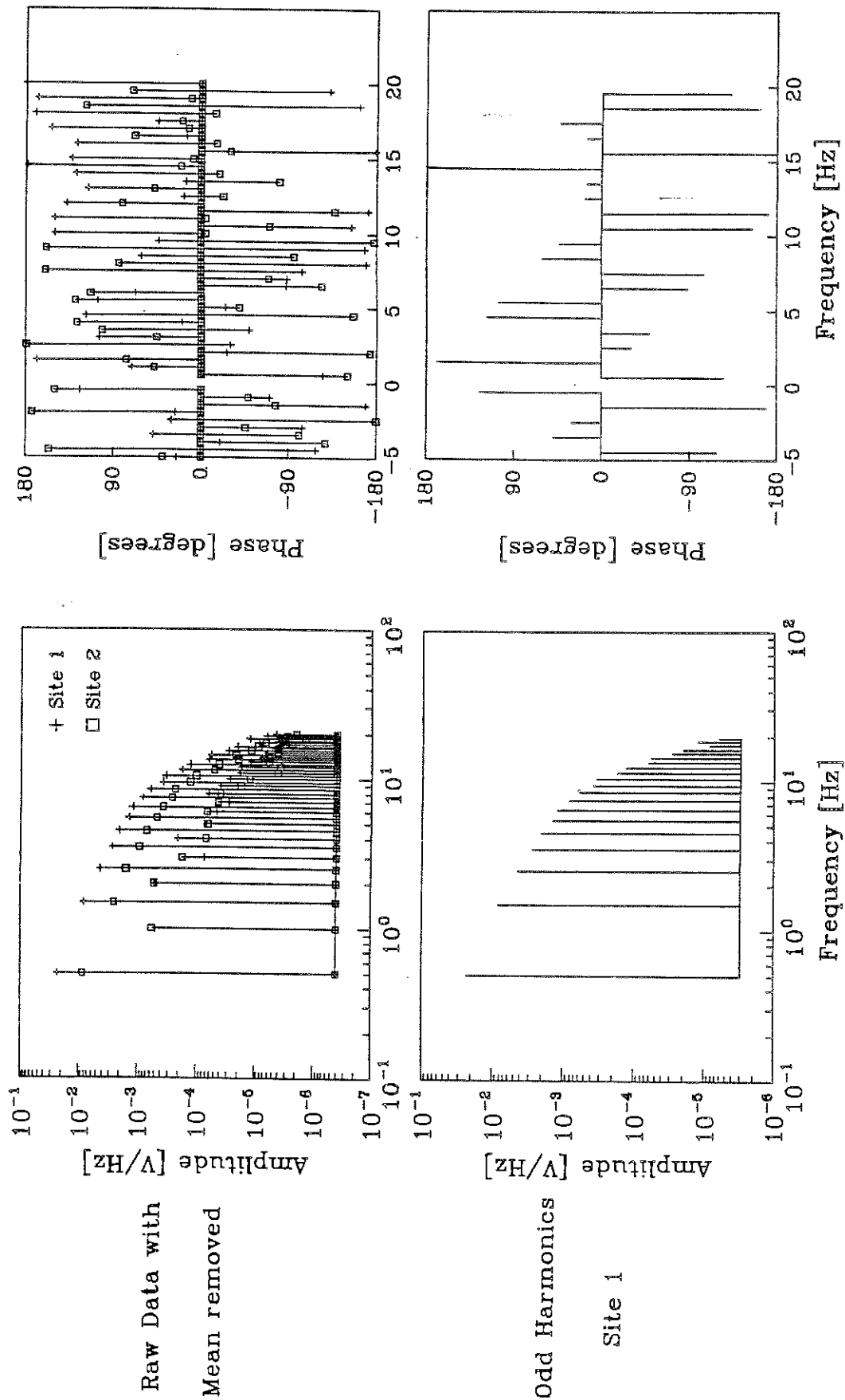


Figure 4-6: Steps in the data processing: upper left (a) and upper right (b): Spectral densities of the row data for both sites obtained from stacks #14 and #23 shown in figure 4-4; lower left (c) and lower right (d): The signal lines (odd harmonics) of the site 1 (stack #14) data singled out.

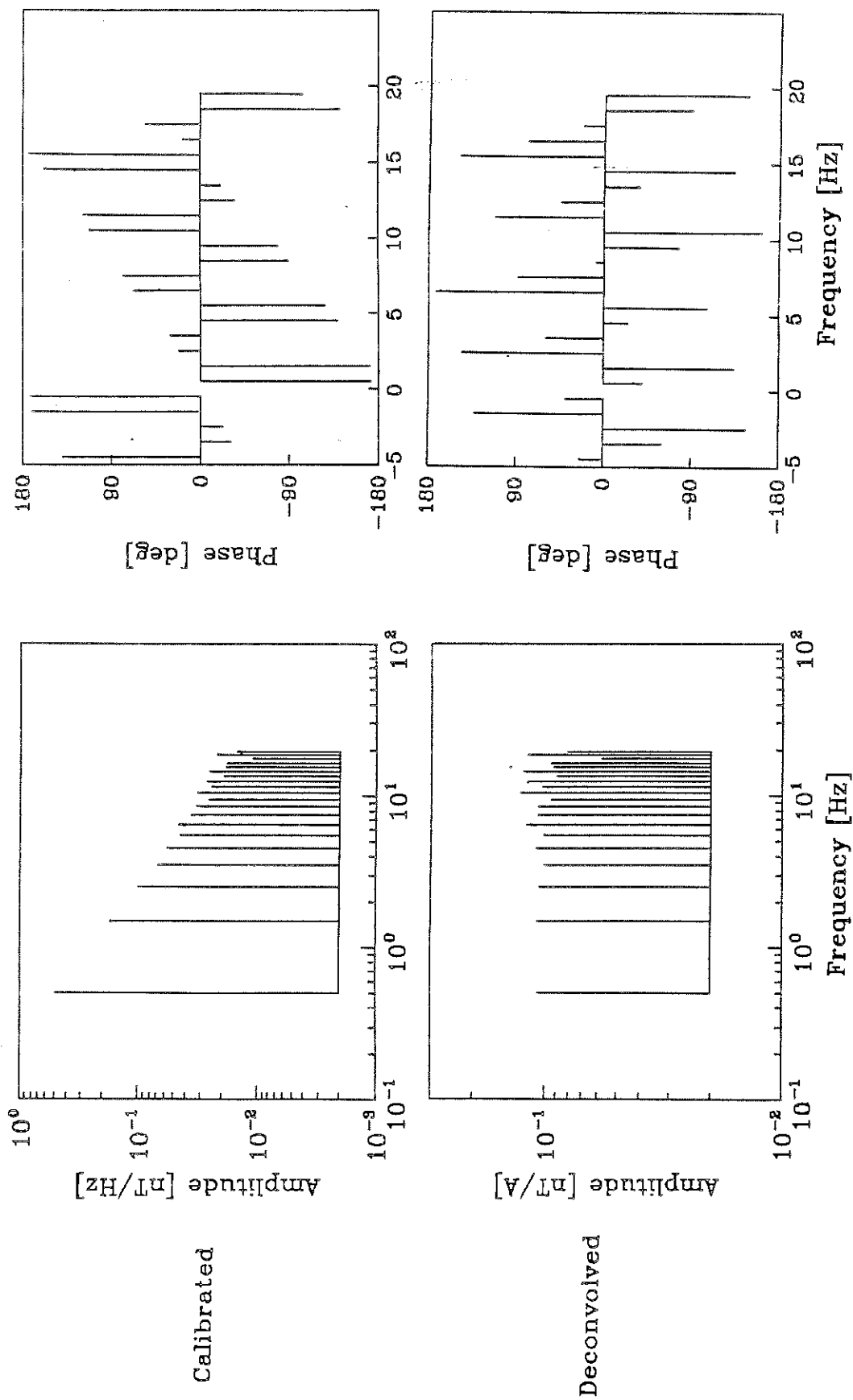


Figure 4-6: continued, upper left (e) and upper right (f): calibrated through division of 4-6 c.d by the OBC transfer function; lower left (g) and lower right (h): earth response function obtained after dividing 4-6 e,f through the artificial OBT signal spectral density. No drift correction applied so far.

the even harmonics that were not contained in the transmitted OBT signal. The amplitudes range over 5 decades so that the mean had to be removed before the Fourier transformation in order to prevent inaccuracies that could arise because the calculations were done in 6 decimal digit precision.

The signal lines of the site 1 (stack #14) data have been selected in figure 4-6c,d and will now serve as an example to explain the further processing. The spectral densities of the recorded signal from figure 4-6c,d are calibrated through division by the OBC transfer function. The result in figure 4-6e,f clearly exhibits the  $1/\text{frequency}$  shape that is indicative of the transmitted signal spectral density at the low frequencies. In the next step the spectral densities are divided by the spectral density of the artificial transmitter (OBT)-signal because the monitored OBT-signal is too distorted as discussed in chapter 3. The result of this deconvolution in figure 4-6e,f represents the earth response function as measured by the MINI-MOSES system. Its unit nT/A indicates the meaning: received magnetic induction per transmitted electric current at a certain frequency.

Two different representations useful for the interpretation can now be derived from the processed data:

the inverse Fourier transform of the calibrated data represents the magnetic induction at the OBC produced by the OBT action (time domain representation) and, secondly, apparent resistivity and phase spectra follow from the deconvolved data (frequency domain representation). In both cases the quality of the representation is limited by the bandpass nature of the OBC transfer function: small signal spectral densities especially at high frequencies are divided by small values of the OBC transfer function in the calibration process so that noise becomes relatively more important.

The time-domain representation obtained by inverse Fourier transforming (appendix A) the calibrated spectral densities is shown in figure 4-7. The above mentioned effect of high frequency noise amplification is clearly visible but not severe enough to justify filtering which would also deteriorate the signal shape. The results in figure 4-7b were obtained by setting all even harmonics to zero so that the inverse transform uses only signal lines. The apparent improvement seen in the results is however misleading because the operation forced a symmetry upon the result that the original data records did not have: the cut-off first peak in the original data (section 3.3) shows through in the reduced amplitude around  $t = 0.5s$  in figure 4-7a. Slightly better results may be obtained after



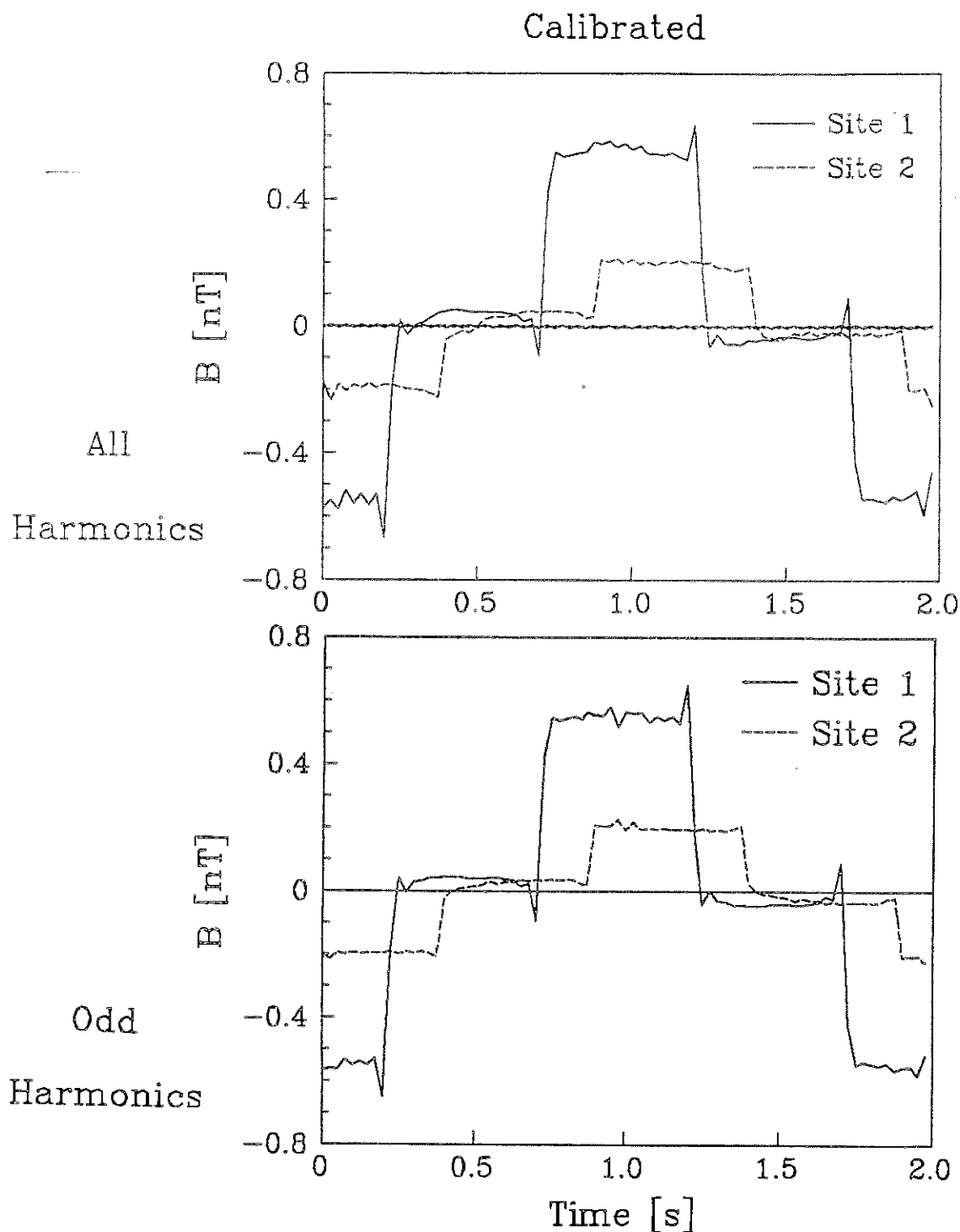


Figure 4-7: Magnetic induction signal at the receiver (OBC) due to the transmitter (OBT) action at two different sites. (a) upper: obtained by inverse Fourier transforming the calibrated spectral densities at the OBC, (b) lower: obtained using only the signal spectral lines (odd harmonics of 0.5 Hz) for the inverse Fourier transform.

tediously correcting the first peak in the original data by hand. A drift correction (see below) was found to introduce high frequency noise because being more accurate than a sample length (25 ms) it was applied to the phase spectrum before the inverse Fourier transformation. It should not be done for this representation.

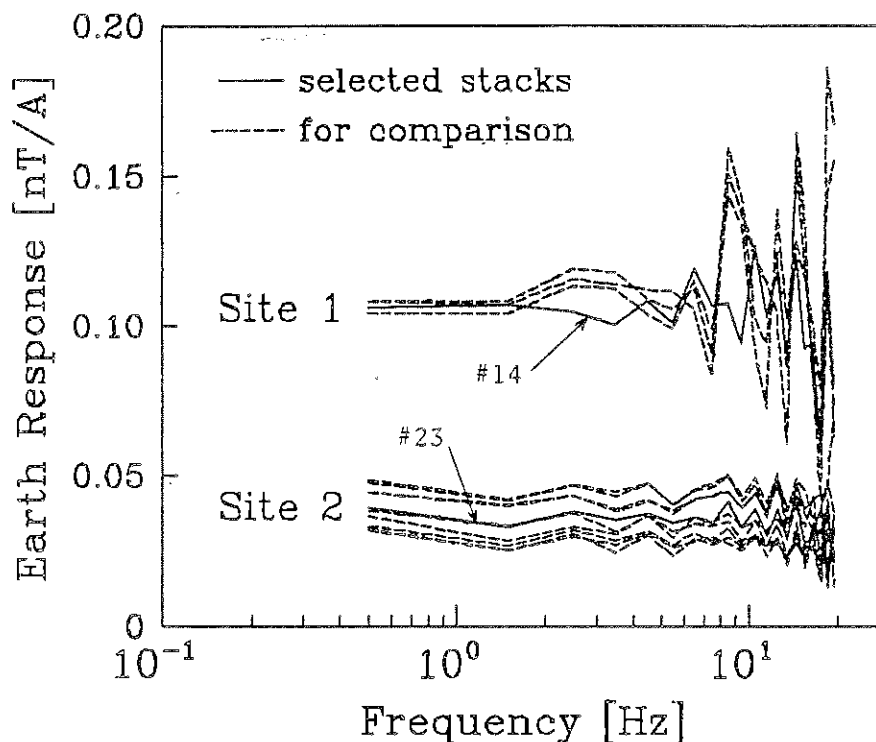
The earth amplitude responses in figure 4-8a were obtained for all signal stacks from the ALVIN survey the same way as the one for stack #14 shown previously (figure 4-6g). This consistency check shows visually that the amplitude drift did not appreciably change the frequency characteristics. The short 3 Hz oscillation in all but the selected #14 site 1 data shows up as an increased spectral density around 3 Hz (dashed lines in figure 4-8a). Stack #23 - selected from the site 2 data - lies in the center of the variable amplitude levels attributed to tidal water currents (see above).

The frequency domain representation required the decision of which OBT signal to use for the deconvolution and it now requires an improved estimate of the phase drift; each item will be explained now.

Figure 4-8b shows how using the distorted monitor-data from the OBT for the deconvolution could result in false

## Consistency Check

Using Synthetic OBT Current



Using Measured OBT Current

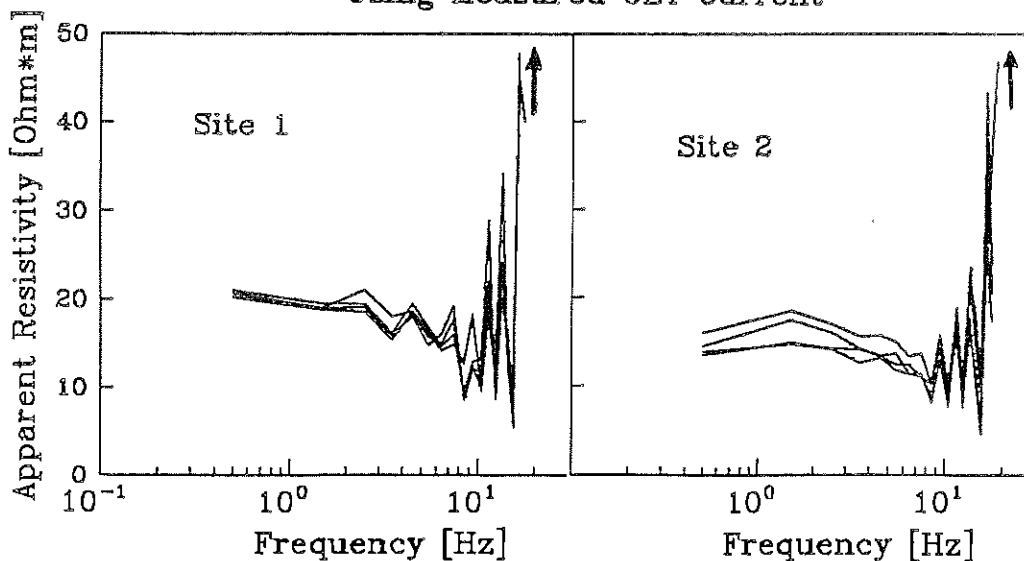


**Figure 4-8:** Consistency check and comparison between results obtained with synthetic or measured OBT signal. (a) upper: the earth response obtained as in figure 4-6 g ("deconvolved") but repeated for all signal stacks from the survey and assembled. (b) lower: the same as in (a) except with the measured OBT signal used for the deconvolution and with the ordinate scaled in apparent resistivity which is inversely proportional to the earth response at each site.

interpretations: the results shown are scaled in apparent resistivity (equation 2.1(6)) which is inversely proportional to the earth response at each OBT-site. The apparent resistivity appears to consistently decrease with frequency which could lead to the false assumption of an induced polarization effect. Obviously the OBT-monitor needs to be redesigned before its records could be useful for the deconvolution.

The initial rough estimate of the frequency difference (2.3 ppm, figure 4-5b) between the clock-oscillators (phase-drift) was improved using the condition that the phase spectra of redundant data sets (stacks recorded at the same site) be consistent. Trial and error resulted in  $(2.34 \pm 0.01)$  ppm as shown in figure 4-9a. The phase changes with frequency seem still much larger than expected from a reasonable earth model. Using the condition that the earth impulse response (the inverse Fourier transform of the earth response function) be symmetric about zero time (and about 1 s because of the antisymmetric signal) it was found by trial and error that all data sets have a common offset of  $(0.040 \pm 0.002)$ s. This offset could have been generated when the OBC and OBT were synchronized onboard the ship: instead of using a well defined logic edge we simply grounded the reset lines by hand. The accuracy found for the offset seems the maximum possible for these data sets because 2 ms is just

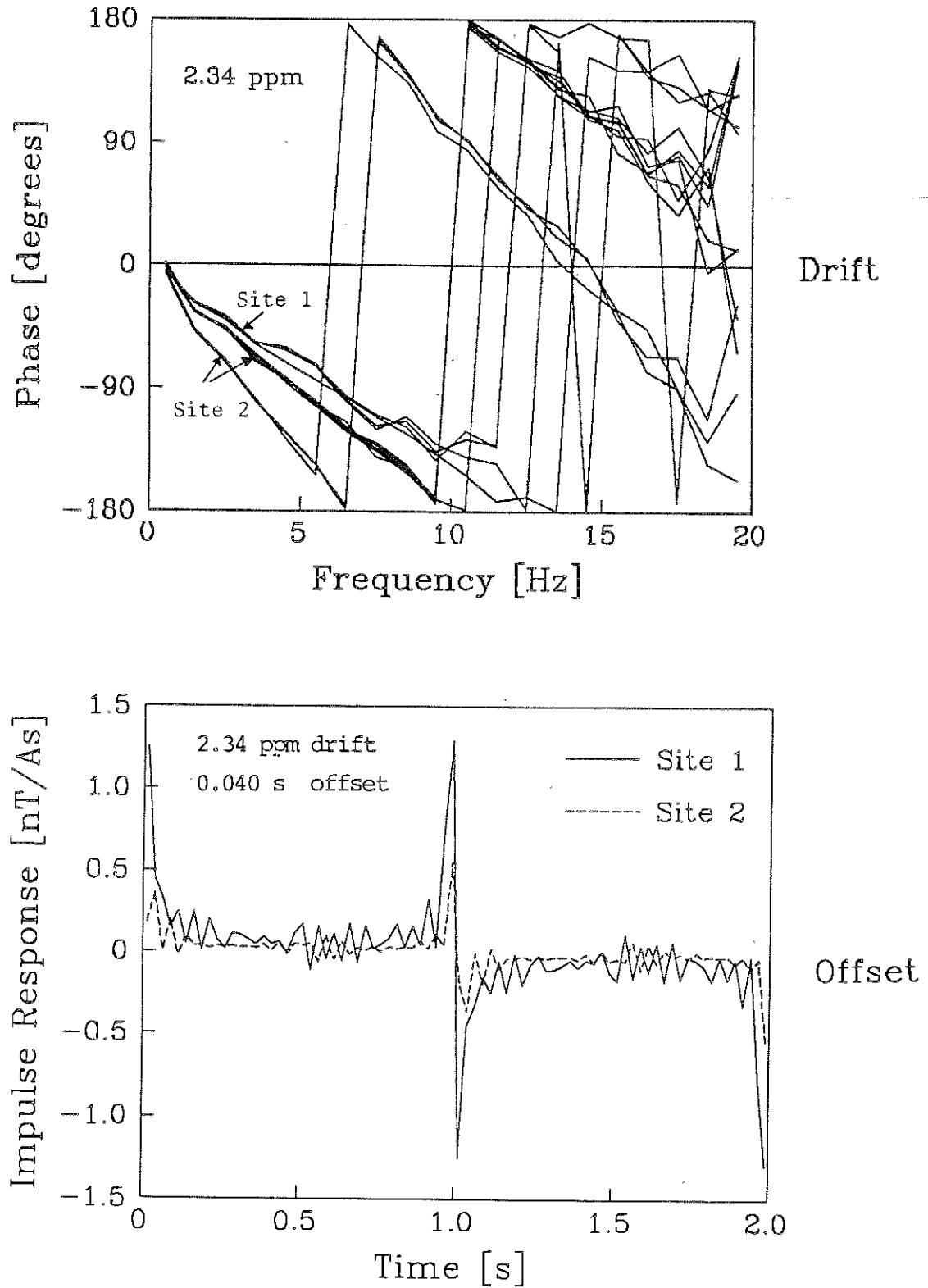


Figure 4-9: (a) upper: consistency of the phase spectra used to find an accurate drift correction; the steeper one of the site 2 groups of phase curves corresponds to signal stacks recorded during the extreme of the tidal variation; (b) lower: symmetry of the earth impulse response used to find an offset common to all data sets.

the time shift caused by the 2.34 ppm phase-drift rate over the 15 min averaging time. Both drift and offset can be used to correct the phase  $\phi$  [degrees] at frequency  $f$  [Hz] measured at time  $t$  [s] after the start (reset time) of the survey by the amount:

$$\Delta\phi = (0.040s + 2.34 \times 10^{-6} \times t) \times f \times 360^{\circ}$$

with the uncertainty:

$$\delta(\Delta\phi) = (\pm 0.002s) \times f \times 360^{\circ}$$

The earth response function represents the received magnetic induction per transmitted electric current. The apparent resistivity contrast derived in chapter 2 can now be generalized by redefining the factor  $I/B$  in equation 2.1(6) as the frequency-dependent earth response function. Figure 4-10a shows the so calculated apparent resistivity for the selected stack #14 and #23 data.  $B/I$  has been scaled down to the projection of the  $Y$ -sensor onto the azimuthal direction (perpendicular to the OBC-OBT line). The error bars represent the  $\pm 10m$  uncertainty in separation propagated through the apparent resistivity formula. Errors in  $I/B$  (about 10%) are comparably small. Beyond the OBC-bandwidth amplified noise causes a larger scattering of the apparent resistivity estimates - they have not been included here nor will they be used in the interpretation.

The phase spectra in figure 4-10b are obtained from the phase of the earth response functions (see for example

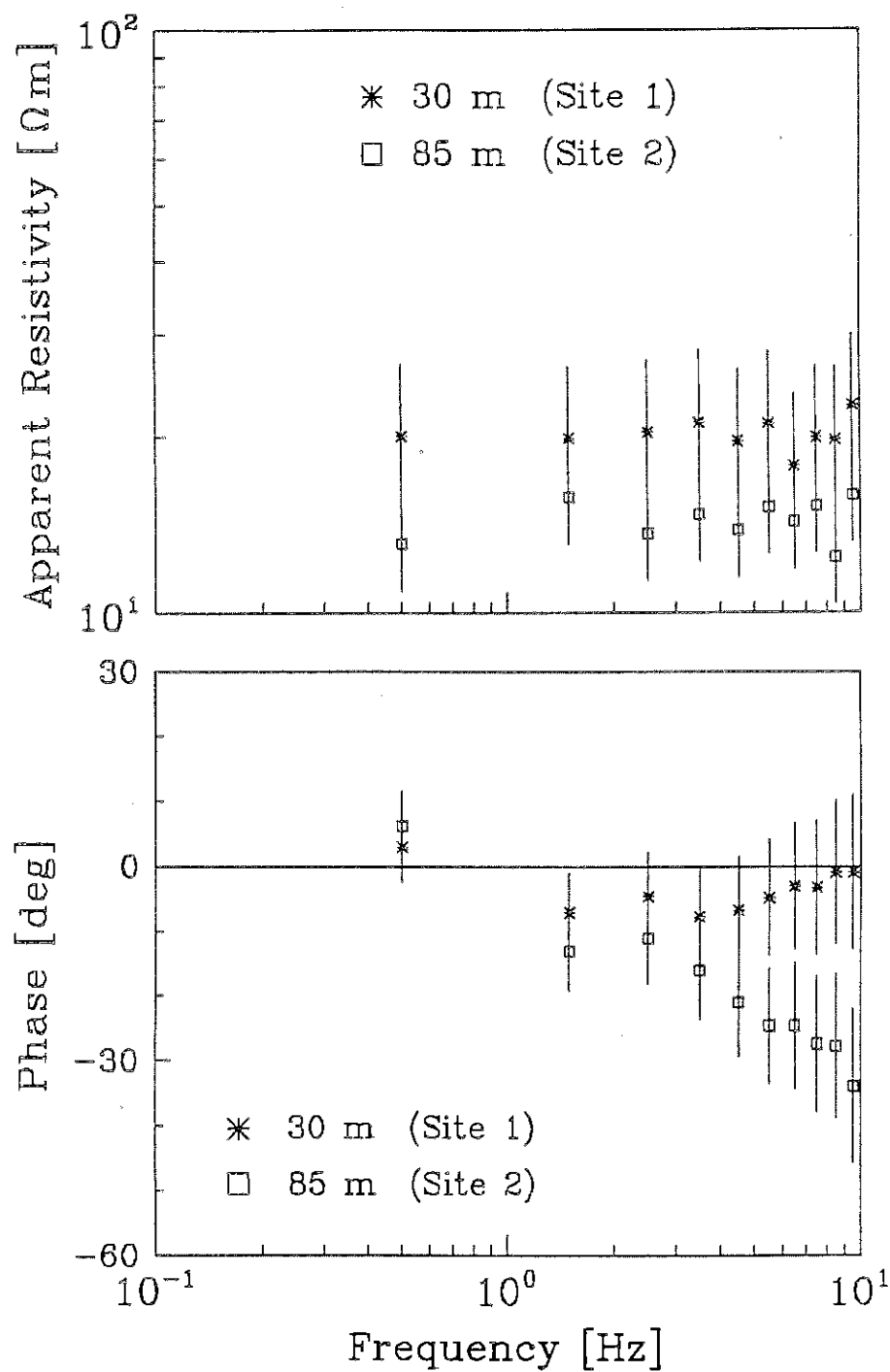


Figure 4-10: Frequency domain results derived from the earth response function. (a) upper: apparent resistivity with errors mainly due to the uncertainty in position. (b) lower: phase spectrum after correction; errors are due to uncertainties in the OBC transfer function and in the phase correction.

figure 4-6h) after adding the above derived correction  $\Delta\phi$ . The error bars represent the sum of the  $\pm 5^\circ$  uncertainty in the OBC transfer function and the above derived uncertainty  $\delta(\Delta\phi)$  in the phase correction. Phase estimates beyond the OBC-bandwidth are unreliable because of the steep phase transfer function in connection with the decreasing signal to noise ratio.

#### 4.4 RESULTS AND INTERPRETATION

The various steps of the data processing allowed three stages of extracting increasingly sophisticated results. All stages could however be implemented on a personal computer for onboard processing without unreasonably long computing times.

The first stage requires only the recorded voltages from the OBT for estimating the transmitted current from the OBT calibration (2.59 A/V), and the recorded voltage from the OBC for estimating the received magnetic induction from the height of the first peak divided by 0.04 (section 3.2.2). Together with the OBC-OBT separation recorded by the ALVIN-crew they give onboard apparent resistivity estimates of



about 20  $\Omega\text{m}$  (OBT site 1, 30 m separation) and 10  $\Omega\text{m}$  (OBT site 2, 85 m separation).

The second stage requires Fourier transformations and the knowledge of the OBC-transfer function in order to reconstruct the magnetic induction at the OBC. More accurate estimates of the magnetic induction at the OBC can now be obtained by measuring the average height of the square pulses in nT and scaling them with the direction cosines. Using the positioning information the results can then be plotted directly onto a prefabricated set of type curves (calculated according to chapter 2) as shown in figure 4-11. A seafloor halfspace of 15  $\Omega\text{m}$  (curve A) fits the data (crosses), but just within the error bars. The measured fields are also consistent with a resistive layer over a conductive halfspace (for example curve D: 30 m of 30  $\Omega\text{m}$  over 1  $\Omega\text{m}$ ). Conductivities and depths in this model cannot be determined separately because of the inherent non-uniqueness of the inverse problem. A conductive layer over a resistive halfspace would however have to be thin and not much more conductive than the halfspace in order to be consistent with the data (see curve E). Such a model would differ very little from a simple halfspace model. I will therefore not consider it for the interpretation.

## One-dimensional Models

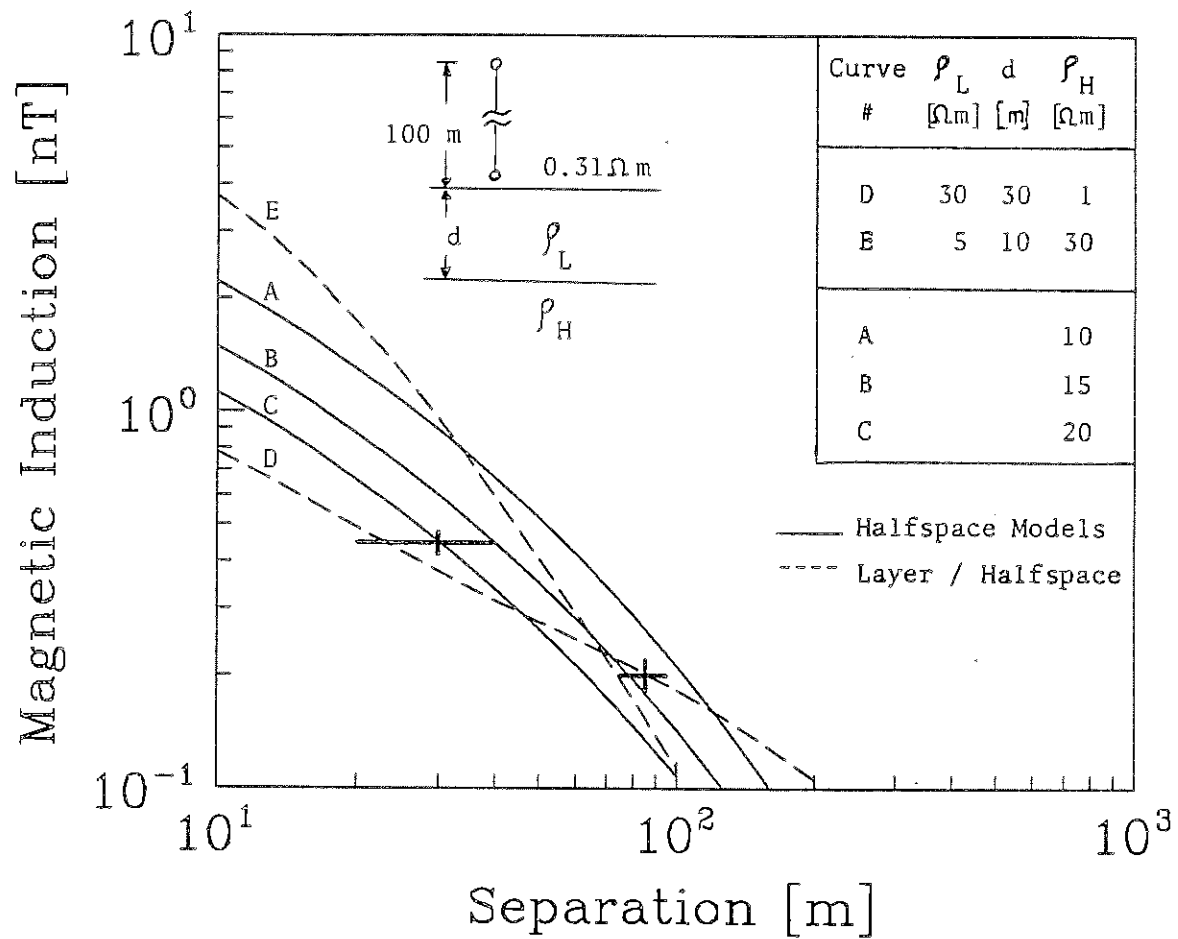


**Figure 4-11:** One dimensional interpretation of calibrated OBC data and positioning information. Errors in separation are  $\pm 10m$ ; errors in magnetic induction are the visually estimated standard deviations of the calibrated records

The third stage of data processing results in the apparent resistivity and phase spectra. The variation with frequency could provide additional independent information. Dr. R.N. Edward's inversion programme (see section 2.1) was modified for the MINI-MOSES configuration and applied to apparent resistivity and phase spectra below 10 Hz (i.e. within the OBC-bandwidth). The results in figure 4-12b show that the data are consistent with a variety of models even though the class of models had been restricted to halfspace and layer over halfspace cases. The decreasing sensitivity of the apparent resistivity with depth seen in figure 4-12a (the curves were produced using equation 2.1(12)) may explain why the resistivity is not well constrained there. All these models fit the data as can be seen in figures 4-12c,d. Even when the programme was forced to fit a halfspace it succeeded with the predicted apparent resistivities just grazing the error bars of the measured ones for a 14  $\Omega\text{m}$  halfspace. This value agrees with the 15  $\Omega\text{m}$  found from the straightforward modeling of the results from the second stage of the data processing above.

The halfspace model would correspond to seawater-saturated seafloor basalts. Their bulk porosity  $\phi$  could be calculated from the measured electrical resistivity,  $\rho$ , and the resistivity of the pore fluids,  $\rho_f$ , using the empirical Archie's law:

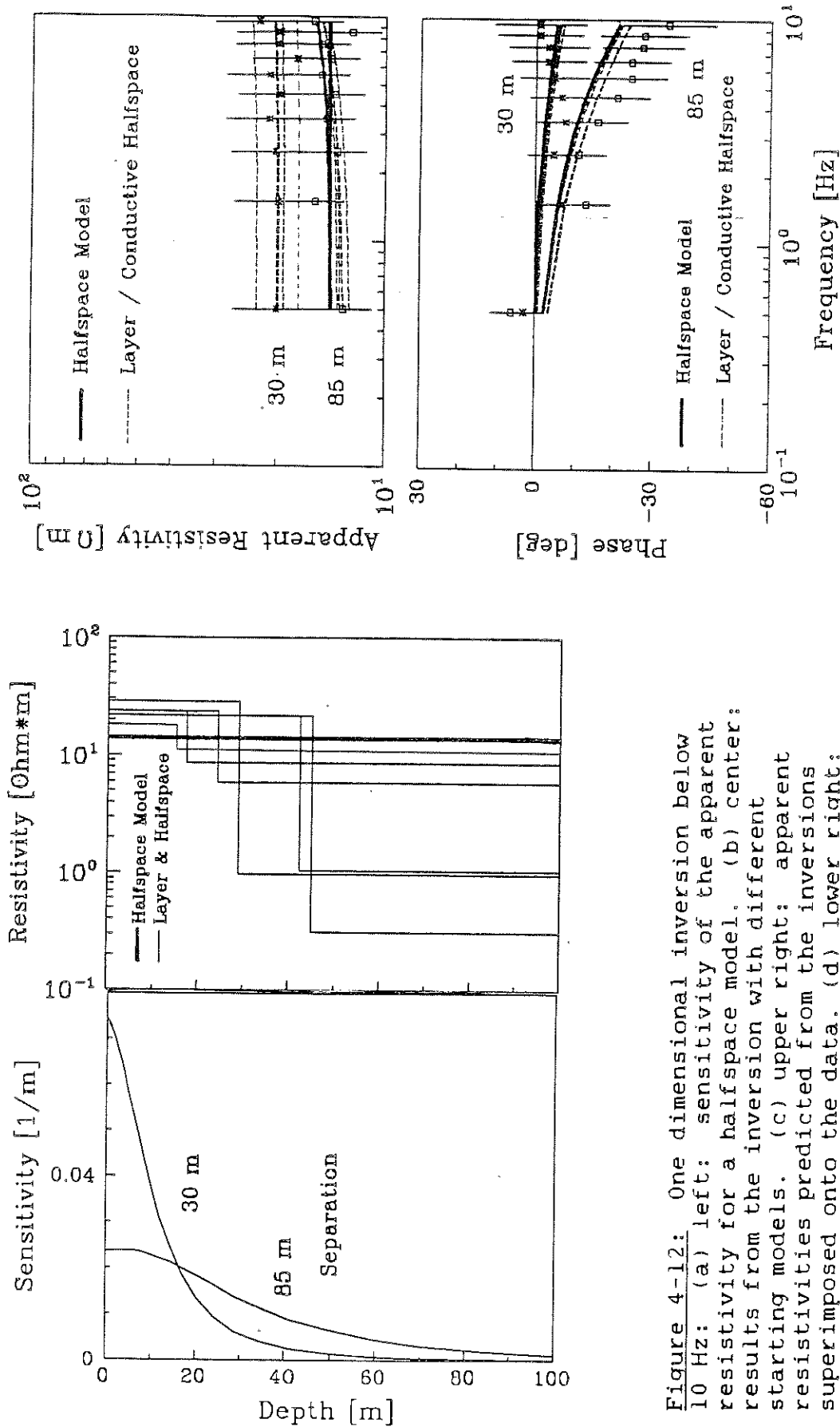


Figure 4-12: One dimensional inversion below 10 Hz: (a) left: sensitivity of the apparent resistivity for a halfspace model. (b) center: results from the inversion with different starting models. (c) upper right: apparent resistivities predicted from the inversions superimposed onto the data. (d) lower right: predicted phase spectra. A 140m halfspace fits all apparent resistivity and phase data thereby just grazing the apparent resistivity error bars.

$$\frac{\rho}{\rho_f} = a \phi^{-m}$$

where  $a$  and  $m$  are empirical constants. Although developed for sedimentary rocks this relationship has been tested and applied to seafloor basalts that have largely vesicular and thus poorly connected porosity (except in rubble zones and in fractured zones) resulting in the empirical values  $a \sim 1$  and  $m \sim 2$  (reviewed by Becker et al., 1982; Hyndman et al., 1983).  $\phi = 12\%$  was estimated for the uppermost basalts in DSDP Hole 504B (Becker et al., 1982; Becker, in press) and in DSDP Hole 395A (Hyndman et al., 1983) after correcting resistivity logs for the decrease in fluid resistivity with the higher temperature in the boreholes. For the upper tens of meters the temperature of the pore fluids should be near that of the deep ocean ( $2^{\circ}\text{C}$ ). The electrical resistivity of the deep ocean water,  $0.31 \Omega\text{m}$  (Bullard and Parker, 1970, appendix) seems therefore appropriate for the pore fluids in my case.

Because of the non-uniqueness involved in inverting my two data points without additional information, the  $14 \Omega\text{m}$  halfspace model does not constrain the basalt resistivity. The latter would be higher if I allowed for a two-layer model with a low-resistivity zone. Rather than calculating a porosity I will now assume that the shallowest well-log

porosities (12 % at about 300 m depth) are representative for the upper tens of meters of basalt. This results in 20  $\Omega\text{m}$  resistivity for the seawater-saturated basalts.

The resistive layer over a conductive halfspace comprises a wide range of possible models as can be seen from the inversion results in figure 4-12b. This class of models may be interpreted in two different ways: a) as a water lens covered by a basalt layer or b) as a stratiform sulphide deposit covered by a basalt layer.

a) A drained lava lake, now filled with seawater is indicated on the map (figure 4-2, "collapse structure") near the OBC. Such structures can be 15 m deep (Hekinian, 1984) and represent a conductive (seawater) lense (layer) over a resistive halfspace (basalt). Such a "water-layer" underneath the OBC would not have been detected if it was very thin (about 0.5 m). It might however be thick and covered by tens of meters of basalt thus representing a 0.3  $\Omega\text{m}$  "halfspace" underneath a thick (about 40 m, inferred from figure 4-12b for a 0.3  $\Omega\text{m}$  halfspace) resistive layer. A large, thick water lense, covered by thick, heavy material might be mechanically unstable and parts of it may collapse. Rubble zones with 50 % or more porosity or interconnected small water lenses also represent conductive zones underneath the solid-looking basalt flows at the seafloor.

Such scenarios are most likely the cause for the results obtained in this survey.

b) A stratiform sulphide deposit might have been formed when a vent area with sulphides was covered by lava flows. The electrical resistivity of the seafloor sulphides can however at best be guessed. Various models are therefore possible according to the inversion results in figure 4-12b, even when the basalt resistivity is close to 20  $\Omega\text{m}$  as I have suggested above. They range from a 15 m basalt layer over 10  $\Omega\text{m}$  sulphides to a 40 m basalt layer over 0.3  $\Omega\text{m}$  sulphides. As seen from the halfspace sensitivity in figure 4-12a, little information is available from below 40 m. The trend that lower resistivities are allowed for sulphides underneath thicker basalt cover may well continue. Metallic sulphide deposits in ophiolites on land are typically covered by younger lava flows which stopped their dissolving in seawater immediately after formation. A detailed MINI-MOSES survey could delineate such conductive lenses at depth underneath the seafloor.

So far, the inversion of the survey results was restricted to layered earth models and each statement about possible interpretations should have an "if there are no lateral variations in electrical resistivity, then ..." placed in front. Allowing for lateral resistivity changes

introduces new variables into an already non-unique inversion. I will therefore start with the assumption that the seawater-saturated basalts have a bulk electrical resistivity of 20  $\Omega\text{m}$ . An estimate of the direct-current channeling by a steep conductive plate underneath the surface expressions of the sulphides may then serve to estimate an upper limit on the size of the deposit. A vertical plate appears reasonable because the hydrothermal activity is likely controlled by the vertical faults near the ridge-axis. Stephen J. Cheesman (1983) devised an algorithm to calculate the magnetic field of an electric current source in a conductive medium in the presence of a conducting thin plate (i.e. currents only in the plane of the plate). An integral equation is solved for the electric field in the plate. With the conductance of the plate given, surface currents can be calculated and from them the magnetic field at the receiver. The algorithm was modified for the MINI-MOSES case.

A possible stockwork zone was simulated as the plate shown in figure 4-13 with various conductances and embedded in a 20  $\Omega\text{m}$  host medium. The depth extent of 50 m would include only the part that might contain appreciable amounts of sulphides. The 90 m length of the plate was taken as the length of the active hydrothermal zone. The results in figure 4-14 indicate that a 5 S plate is consistent with the



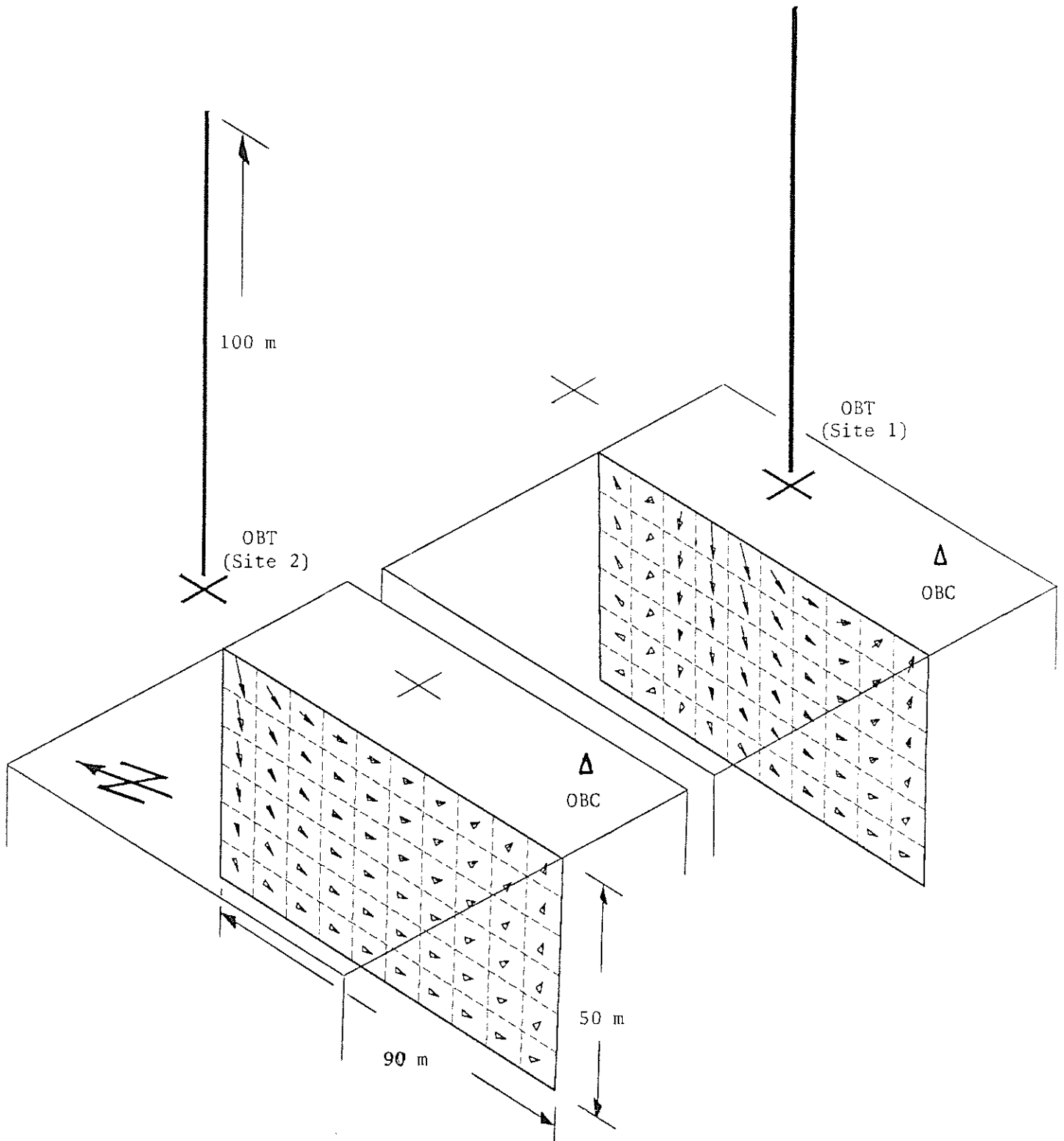


Figure 4-13: Thin conductive plate model for a possible downward extension of the sulphides. The arrows indicate direction and normalized size of the currents in the plate for each transmitter location. The plane of the ocean-seafloor boundary is indicated as the top of the two perspective "boxes".

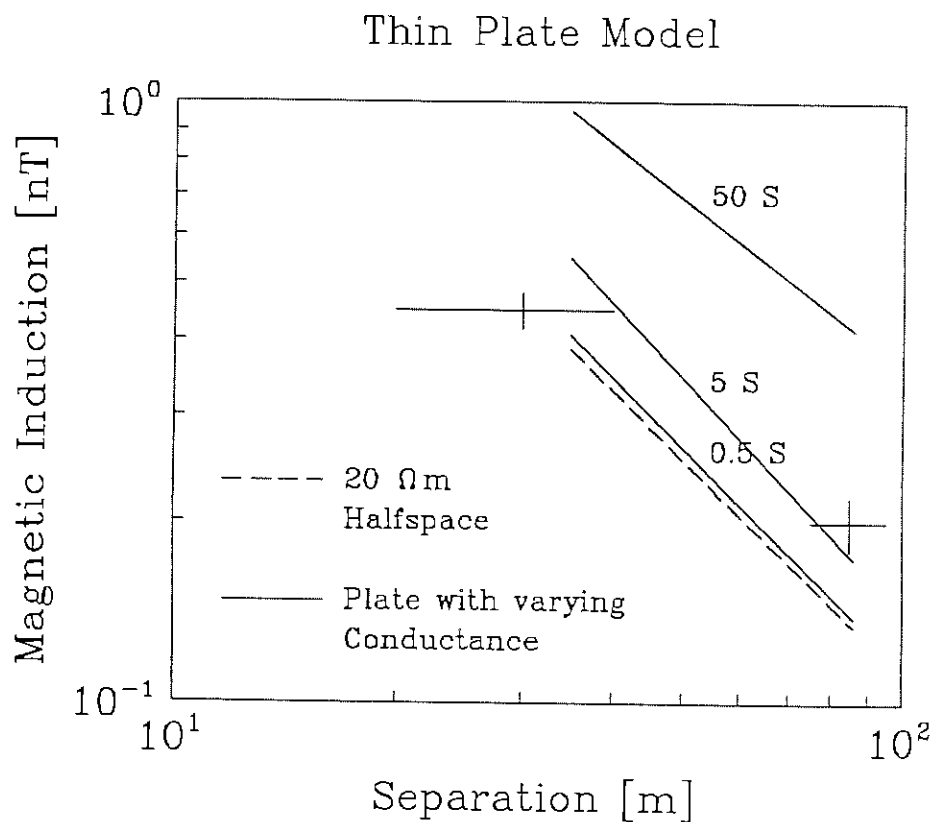


Figure 4-14: Results from the thin plate models (lines) superimposed onto the measured fields (crosses). The model results (even though there are only two points per line) are shown as lines for easier viewing. The dashed line is the field due to the host medium alone.

data. The thickness of the plate could be obtained by multiplying conductance with resistivity. Francis (in press) measured  $0.035 \Omega\text{m}$  on one sample of seafloor sulphides. The bulk resistivity may, however, be larger because of the abundant Sphalerite in seafloor deposits (Oudin et al., 1981). Even with a water content of 25-50% (Crawford et al., 1984) the in situ resistivity might be as high as  $1 \Omega\text{m}$ . This would result in 5 m thickness for the plate. The deposit is then at most  $20,000 \text{ m}^3$  in volume which, using the density  $5 \text{ g/cm}^3$  for pyrite translates to 100,000 metric tons. This is below the size of economic land deposits even after adding the few hundred to few thousand tons visible at the surface. If one assumes that this plate continues along the ridge-axis then at most 100,000 tons every 100 m could be found. More likely, the deposit is localized because of the localized nature of the hydrothermal activity (Crane and Ballard, 1980). If the host resistivity was only  $14 \Omega\text{m}$  instead of the assumed  $20 \Omega\text{m}$ , then there would be no need of a conductive plate to explain the data. If the host resistivity was  $30 \Omega\text{m}$ , then the plate model would still result in a relatively small deposit.

This type of metallic sulphide accumulation would therefore not represent the ancestors of land deposits in the Cyprus ophiolites or elsewhere that have been related to

submarine hydrothermal springs. It might, however, develop into a larger one before the magmatic activity shifts (as proposed by Crane and Ballard, 1980) to a different volcanic center along the ridge-axis. A MINI-MOSES survey over a relatively young, inactive vent area might clarify this point. The deposits in the Cyprus and Oman ophiolites are clearly fault-controlled (Coleman, 1977, chapter 5) and may - as suggested by Malahoff (1982) - be related to the large deposits discovered in off-axis fault scarps. A MINI-MOSES survey should therefore be located in this geological setting.

## 5. CONCLUSIONS AND SUGGESTIONS FOR FUTURE WORK

### 5.1 SUMMARY

The upper few tens of meters of seafloor basalt on a mid-oceanic ridge have been investigated with a geophysical method. Also for the first time a possible subsurface extension of a polymetallic sulphide deposit has been examined at the seafloor.

For this purpose I have developed an electromagnetic technique that uses a vertical electric bipole transmitter to feed electric current into the seafloor, and an induction coil magnetometer that measures the magnetic field of that current at various distances from the source bipole. Both instruments are self-contained and microprocessor-controlled, recording transmitted and received waveforms in random access memory. The transmitter drives a  $\pm 5$  A regulated current with an IP-waveform of 2 s period into a 100 m long insulated vertical wire with large stainless steel electrodes at either end. The induction coil receiver measures two orthogonal, horizontal components of the magnetic field. Four horizontal-axis coils (two for each component of the magnetic field) are wound on a square, soft-iron core. Each of the two sensor components

represents a 990  $\Omega$  resistance, a 93 H inductance, and a 7.6  $\mu\text{V}/(\text{nT}\cdot\text{Hz})$  electromotive force. After amplification and digitization, the signal is recorded with the dynamic range 0.3 pT - 80 nT over the bandwidth 0.3-10 Hz. Predicted instrumental noise was mainly of low frequency at a level of 3 pT. The noise during the test survey was an order of magnitude higher because of faulty electronic parts.

A test survey was conducted in 2200 m deep water on the Endeavour Segment of the Northern Juan de Fuca Ridge ( $47^{\circ}57'\text{N}$ ,  $129^{\circ}06'\text{W}$ ) near a sulphide deposit in an active hydrothermal vent field (Wolfgram et al., 1984). The OBT and OBC were lowered close to the seafloor at the end of a cable and then released. The deep submersible ALVIN located them and then adjusted their separation to different values at prearranged times. After three days the buoyant aluminum pressure spheres automatically released from their anchor weights and floated up to the surface to be recovered and the instruments interrogated. The data were measurements of two horizontal components of the magnetic field at two different transmitter-receiver separations (30m and 85m).

The transmitted and received signals included the odd harmonics of the 0.5 Hz base frequency with decreasing amplitudes towards the higher harmonics. The redundancy in the phase data was used to find accurate corrections for

offsets in start time and frequency of the clock-oscillators in transmitter and receiver. These corrections allowed the recovery of phase information from the data. The data processing resulted thus in apparent resistivity and phase spectra. The redundancy in the amplitude data allowed an estimate of the inclined wire effect that appears mainly due to (reversing) tidal water currents.

The inversion in terms of a one-dimensional electrical resistivity structure below the seafloor showed that the data are consistent with a resistive layer over a conductive halfspace. The thicker the resistive layer on top, the lower a resistivity of the halfspace is allowed by the data. Possible interpretations range from a 15 m basalt layer over a 10  $\Omega\text{m}$  high porosity zone or stratiform sulphide deposit to a 40 m basalt layer over 0.3  $\Omega\text{m}$  sulphides or over a drained lava lake now filled with 0.3  $\Omega\text{m}$  seawater. Little can be said, however, about depths beyond 40 m because the 85 m maximum transmitter-receiver separation in this survey limited the depth penetration to about 40 m. The vertical electric bipole technique would have resolved thicknesses and resistivities with little "geological input" if enough data points had been available (about 10 instead of my 2 points, see for example Edwards et al., 1985).

With lateral resistivity changes allowed in the form of a vertical conductive (sulphide) plate, the inversion was again non-unique. The host resistivity was inferred from DSDP results as 20  $\Omega$ m for the upper seafloor basalts with about 12 % porosity. With this model parameter fixed the interpretation indicates a deposit between a few 100 tons and a few 100,000 tons of sulphides which is smaller than economic land deposits.

## 5.2 SUGGESTIONS FOR FUTURE WORK

All three main aspects of this thesis - theory, instrumentation, and application - represent advances into unknown territory. I have attempted to lay down a solid basis for future work. The possible extensions will now be summarized.

### 5.2.1 THEORY

The simple one-dimensional model in chapter 2 requires an extension to include lateral changes in electrical conductivity. The measured magnetic induction as a function



of frequency and transmitter-receiver separation could be predicted through numerical modeling. Appendix B seems a promising basis for an efficient computer algorithm.

The theory should also be extended to the case of an anisotropic resistivity. This was already done for the MOSES technique by Nobes (1984) and Edwards et al. (1984).

#### 5.2.2 INSTRUMENTATION

Much of the success of the MINI-MOSES instrumentation can be attributed to its bandlimiting features. On the other hand, an expansion of the bandwidth may permit induced polarization measurements and frequency sounding. I have indicated in chapter 3 several possible modifications that would allow an extension of the bandwidth to optimistically 0.1 Hz - 1000 Hz. Table 5-1 shows the ranges where induction becomes important enough to limit OBC-OBT separations.

Both OBC and OBT would require a faster analog to digital conversion and optimized software to keep up with kHz sampling rates. The clock oscillators would have to be

adjusted, and shorter intervals between system resets (shorter survey times) should be taken into consideration.

Table 5-1: Skin depths in various media

| Resistivity<br>[ $\Omega$ m] | Skin depths in [m] for frequency |       |        |         | Material at<br>the seafloor |
|------------------------------|----------------------------------|-------|--------|---------|-----------------------------|
|                              | 0.1 Hz                           | 10 Hz | 100 Hz | 1000 Hz |                             |
| 20                           | 7070                             | 707   | 224    | 71      | basalt                      |
| 2                            | 2236                             | 224   | 71     | 22      | sediment                    |
| 0.3                          | 880                              | 88    | 28     | 9       | sea water                   |

Another important improvement would be a separate battery back-up for the CMOS random access memory to protect the data.

The addition of a vertical component coil would be very desirable for applications over laterally varying conductivity structures.

The measured magnetic fields are created by electric currents underneath the receiver. It should be possible to include into a single pressure vessel both a transmitter and a receiver. If two such packages are placed on the seafloor then the "transmit" and "receive" functions could be swapped by software control. Information about the electrical conductivity underneath each package can thus be obtained

without additional (expensive) submersible actions. Multiple receivers could provide more sounding points without much additional dive-time requirements.

Automatic ranging with software-controlled, acoustic transponders was tested in the October 1984 survey near Toba Inlet, British Columbia. It may provide greater accuracy in estimating the separations as well as save on submersible time.

The anchor weight may be redesigned for easier orientation and levelling in rugged terrain. Lowering the center of mass of the sphere by repackaging is mandatory to make it float upright so that strobe-light and radio-beacon can be detected in the recovery operation.

### 5.2.3 SURVEYS

It is clear from the discussion of the conductive plate model in section 4.4 that we need more information about bulk resistivities of seafloor sulphides in situ. It could be obtained with short MINI-MOSES separations over a large deposit. The separations would have to be short enough so that the deposit "looks" like a halfspace to the receiver.

The porosity or permeability of seafloor basalts - useful parameters for hydrothermal modeling - can be estimated from the measured electrical resistivities. For this purpose, a sounding should be done with a receiver placed in a basaltic area that lacks signs of sulphides to within several hundred meters. A porosity-versus-depth profile could then be determined that ties into the DSDP results which do not contain information from the cased part of the holes (upper few hundred meters).

Both the structural and resistivity information about a large seafloor metallic sulphide deposit as well as the porosity information about its host rocks could provide new insights into the processes that - in geological history - formed many of our valuable mineral resources.

## 6. REFERENCES

- ASM, 1983: Metals reference book, 2nd ed., American society for metals, Metals Park, Ohio.
- Becker K., R.P. Von Herzen, T.J.G. Francis, R.N. Anderson, J. Honnorez, A.C. Adamson, J.C. Alt, R. Emmermann, P.D. Kempton, H. Kinoshita, C. Laverne, M.J. Mottl, R.L. Newmark, 1982: In situ electrical resistivity and bulk porosity of the oceanic crust Costa Rica Rift. *Nature* 300(5893), 594-598.
- Becker K., in press: Large scale electrical resistivity and bulk porosity of the oceanic crust, Hole 504B, Costa Rica Rift. Init. Repts. DSDP, 83, U.S. Govt. Printing Office, Washington.
- Becker R., 1975: *Theorie der Wärme*. Springer-Verlag, Berlin.
- Boerner D., 1984: The calculation of electromagnetic fields from an arbitrary source in a horizontally layered earth. Research in applied Geophysics no.26, Geophysics Lab., Dept. of Physics, University of Toronto.
- Bullard E.C., R.L. Parker, 1970: Electromagnetic induction in the oceans (appendix) in: *The Sea*, 4, Wiley & Sons, Toronto.
- Cathles, L.M., 1980: Fluid flow and genesis of hydrothermal ore deposits. *Econ. Geol.* 75, 424-457.
- Chave A.D., C.S. Cox, 1982: Controlled Sources for measuring electrical conductivity beneath the oceans - 1. Forward problem and model study. *J. Geoph. Res.* 87(B7), 5327-5338.
- Cheesman S.J., 1983: The cross-hole MMR response of a bent lamella. B.Sc. thesis at University of Toronto.
- Coleman R.G, 1977: *Ophiolites - ancient oceanic lithosphere?* Springer-Verlag Berlin.
- Cox, c.S., 1981: On the electrical conductivity of the

- oceanic lithosphere. Phys. of the Earth and Plan. Int. 25, 196-201.
- Crane K., R.D. Ballard, 1980: The Galapagos Rift at 86°W: 4. structure and morphology of hydrothermal fields and their relationship to the volcanic and tectonic processes of the rift valley. J. Geoph. Res. 85(B3), 1443-1454.
- Crawford A.M., S.C. Hollingshead, S.D. Scott, 1984: Geotechnical engineering properties of deep-ocean polymetallic sulfides from 21°N, East Pacific Rise. Marine Mining 4(4), 337-354.
- CYAMEX scientific team, 1979: Massive deep-sea sulphide ore deposits discovered on the East Pacific Rise. Nature 277(5697), 523-528.
- Edwards R.N., L.K. Law, J.M. DeLaurier, 1981: On measuring the electrical conductivity of the oceanic crust by a modified magnetometric resistivity method. J. Geoph. Res. 86(B12), 11,609-11,615.
- Edwards R.N., D.C. Nobes, E. Gomez-Trevino, 1984: Offshore electrical exploration of sedimentary basins: the effects of anisotropy in horizontally isotropic, layered media. Geophysics 49(5), 566-576.
- Edwards R.N., L.K. Law, P.A. Wolfgram, D.C. Nobes, M.N. Bone, D.F. Trigg, J.M. DeLaurier, 1985: First results of the MOSES experiment: Sea sediment conductivity and thickness determination, Bute Inlet, British Columbia, by magnetometric offshore electrical sounding. Geophysics 50(1), 153-161.
- Everett J.E., J.E. Osemeikhian, 1966: Spherical coils for uniform magnetic fields. J. Sci. Instrum 43, 470-474.
- Francis T.J.G., 1985: Resistivity measurements of an ocean floor sulphide ore deposit from the submersible Cyana. Submitted for publication.
- Gerthsen C., H.O. Kneser, H. Vogel, 1974: Physik. Springer Verlag, Berlin.

- Haymon R.M., M. Kastner, 1981: Hot spring deposits on the East Pacific Rise at  $21^{\circ}\text{N}$ : preliminary description of mineralogy and genesis. *Earth and Plan. Sci. Let.* 53, 363-381.
- Heck C., 1974: Magnetic materials and their applications. Translated from German by S.S. Hill. Butterworths Ltd., London.
- Hekinian R., M. Fevrier, J.L. Bischoff, P. Picot, W.C. Shanks, 1980: Sulphide deposits from the East Pacific Rise near  $21^{\circ}\text{N}$ . *Science* 207, 1433-1444.
- Hekinian R., 1984: Undersea volcanoes. *Sci. Am.* 251(1), 46-55.
- Hyndman R.D., M.H. Salisbury, et al., 1983: The physical nature of young upper oceanic crust on the Mid-Atlantic Ridge, Deep Sea Drilling Project hole 395A. *Init. Repts. DSDP, 78B*, U.S. Govt. Printing Office, Washington.
- Jupp D.L.B., K. Vozoff, 1975: Stable iterative methods for the inversion of geophysical data. *Geophys. J. R. astr. Soc.* 42, 957-976.
- Kanasewich E.R., 1975: Time sequence analysis in geophysics. 2nd ed., University of Alberta Press, Edmonton, Alberta, Canada.
- Kertz W., 1978: Statistik geophysikalischer Beobachtungsreihen. 2nd ed., Inst. f. Geophysik und Meteorologie der Technischen Universität Braunschweig, West Germany.
- Kupfmüller K., 1973: Einführung in die theoretische Elektrotechnik. 10th ed., Springer-Verlag Berlin.
- Labson V.F., A. Becker, H.F. Morrison, U. Conti, in press: Geophysical exploration with audio frequency natural magnetic fields. In *Geophysics*.
- Lancaster D., 1979: Active-filter cookbook. H.W.Sams&Co., Inc., Indianapolis, Indiana, USA.
- Law L.K., 1984: Marine electromagnetic research. *Geophysical Surveys* 6, 123-136.
- Lee K.H., H.F. Morrison, 1985: A numerical solution for the

- electromagnetic scattering by a two-dimensional inhomogeneity. *Geophysics* 50(3), 466-472.
- Lydon J.W., 1884: Ore deposit models - 8. volcanogenic massive sulphide deposits part 1: a descriptive model. *Geoscience Canada* 11(4), 195-202.
- Malahoff A., 1982: Polymetallic sulphides from the oceans to the continents. *Sea Technology* 51, Jan. 1982.
- Mende, Simon, 1974: Physik Gleichungen und Tabellen. Heyne-Verlag, München.
- Morse P.M., H. Feshbach, 1953: Methods of theoretical physics, part 1. McGraw-Hill, New York.
- Mottl M.J., H.D. Holland, 1978: Chemical exchange during hydrothermal alteration of basalt by seawater - I. experimental results for major and minor components of seawater. *Geochim. et Cosmochim. Acta* 42, 1103-1115.
- Mottl M.J., H.D. Holland, R.F. Corr, 1979: Chemical exchange during hydrothermal alteration of basalt by seawater - II. experimental results for Fe, Mn, and sulfur species. *Geochim. et Cosmochim. Acta* 43, 869-884.
- Nobes D.C., 1984: The magnetometric off-shore electrical sounding (MOSES) method and its application in a survey of upper Jervis Inlet, British Columbia. Ph.D. thesis at Dept. of Physics, University of Toronto.
- Oberhettinger F., 1972: Tables of Bessel transforms. Springer-Verlag, Berlin.
- Oudin E., P. Picot, G. Pouit, 1981: Comparison of sulphide deposits from the East Pacific Rise and Cyprus. *Nature* 291(5814), 404-407.
- Pelton W.H., S.H. Ward, P.G. Hallof, W.R. Sill, P.H. Nelson, 1978: Mineral discrimination and removal of inductive coupling with multifrequency IP. *Geophysics* 43(3), 588-609.
- Peters, W.C., 1978: Exploration and mining geology. John Wiley & Sons, new York.
- RISE project group, 1980: East Pacific Rise: hot springs and



- geophysical experiments. Science 207(4438), 1421-1433.
- RISE study group, 1981: Crustal processes of the mid-oceanic ridge. Science 213, 31-40.
- Rona P.A., 1976: Pattern of hydrothermal mineral deposition: Mid-Atlantic Ridge crest at latitude 26°N. Marine Geology 21, M59-M66.
- Schabas B., 1983: Undersea deposits could be ancestors of Canada's sulphide orebodies. Canadian Mining Journal 105(5), 32-34.
- Schmucker U., P. Weidelt, 1975: Electromagnetic induction in the earth. Lecture notes, Aarhus, Denmark.
- Seyfried W.E.Jr., M.J. Mottl, 1982: Hydrothermal alteration of basalt by seawater under seawater-dominated conditions. Geochim. et Cosmochim. Acta 46, 985-1002.
- Stoyer C.H., R.J. Greenfield, 1976: Numerical solutions of the response of a two-dimensional earth to an oscillating magnetic dipole source. Geophysics 41(3), 519-530.
- Strens M.R., J.R. Cann, 1982: A model of hydrothermal circulation in fault zones at mid-oceanic ridge crests. Geophys. J. R. astr. Soc. 71, 225-240.
- Sunde e.d., 1968: Earth conduction effects in transmission systems. Dover Publ., New York.
- Telford W.M., L.P. Geldart, R.E. Sheriff, D.A. Keys, 1976: Applied geophysics. Cambridge University Press, Cambridge.
- Wait J.R., 1969: Electromagnetic induction in a solid conducting sphere enclosed by a thin conducting spherical shell. Geophysics 34(5), 753-759.
- Weidelt P., 1975: Electromagnetic induction in three-dimensional structures. J. Geophys. 41, 85-109.
- Wolfgram P., R.N. Edwards, L.K. Law, M.N. Bone, 1984: Electrical resistivity sounding over sulfides on the Northern Juan de Fuca Ridge: the sea floor MOSES experiment. Abstract in EOS 65(45), p.867.

Young P.D., C.S. Cox, 1981: Electromagnetic active source sounding near the East Pacific Rise. Geophys. Res. Lett. 8(10), 1043-1046.

A P P E N D I C E S

## A. FOURIER TRANSFORM AND POWER SPECTRUM

An infinitely long time series of a random variable  $f(t)$  can be thought of as a random process so that each finite section of  $f(t)$  is a realization  $f_j(t)$  of that random process lasting from  $t_j$  to  $t_{j+1} = t_j + T_0$ . A random process (Kertz, 1978)

$$f(t) = \{f_j(t), j=1,2,\dots\} \quad (1)$$

is stationary if its expectation values  $E[f_j(t)]$  - defined as averages over  $j$  - do not depend on the time  $t$  and if  $E[f_j, f_k]$  depends only on the difference  $\tau = t_j - t_k$ . The process is ergodic if averages over  $t$  are equivalent to averages over  $j$ . Now assume that the realizations are normally distributed as would be expected for white noise. The statistics of the realizations is determined by the means  $E[f_j]$  and by the covariances

$$\sigma_{jk} = E[f_j f_k] = E[f(t_j) f(t_k)]. \quad (2)$$

For a stationary and ergodic random process these expectation values can be calculated by averaging over time and the covariances depend only on the difference  $\tau = t_j - t_k$ :

$$\sigma(\tau) = \lim_{T \rightarrow \infty} \frac{1}{T} \int_{-T/2}^{T/2} f(t) f(t+\tau) dt \quad (3)$$

If the process is stationary then the integral from  $-\infty$  to  $+\infty$  over the autocorrelation function  $\sigma(\tau)$  is finite and the process can be represented by its power spectral density via a Fourier transform

$$P(\omega) = \int_{-\infty}^{\infty} \sigma(\tau) e^{-i\omega\tau} d\tau \quad (4)$$

This is a consequence of the Wiener-Khintchine theorem (see Kanasewich, 1975, chapter 7.2). After substituting (3) into

(4) it follows (Kanasewich, 1975) that the power spectral density can be calculated from the spectral density (Fourier transform) of the time series:

$$P(\omega) = \lim_{T \rightarrow \infty} \frac{1}{T} |f(\omega)|^2 \quad (5)$$

The conventions for the Fourier transform pair:

$$f(t) = \frac{1}{2\pi} \int_{-\infty}^{\infty} \tilde{f}(\omega) e^{i\omega t} d\omega \quad \tilde{f}(\omega) = \int_{-\infty}^{\infty} f(t) e^{-i\omega t} dt \quad (6)$$

converted for finite discrete time series of length  $T_0 = N\Delta t$ :

$$t \rightarrow t_j = (j + \frac{1}{2})\Delta t \quad \omega \rightarrow \omega_k = k\Delta\omega = k \cdot 2\pi/T_0 \quad (7)$$

$$f(t) \rightarrow f(t_j) = f_j \quad \tilde{f}(\omega) \rightarrow \tilde{f}(\omega_k) = \tilde{f}_k \quad (8)$$

$$f_j = \frac{1}{T_0} \sum_{k=0}^{N-1} \tilde{f}_k e^{i(j+\frac{1}{2})\frac{2\pi k}{N}} \quad \tilde{f}_k = \frac{T_0}{N} \sum_{j=0}^{N-1} f_j e^{-i(j+\frac{1}{2})\frac{2\pi k}{N}} \quad (9)$$

have been used in this thesis to calculate spectral densities ("Fourier transforms") and power spectral densities:

$$P(\omega) \rightarrow P_k = \frac{1}{T_0} |\tilde{f}_k|^2 \quad (10)$$

The power spectral density of random (white) noise equals the variance of the time series, is independent of frequency, and changes little with the length  $T_0$  of the time series if the latter is long enough.

Stacking (i.e. adding sample by sample)  $K$  time series ("sweeps") of  $N$  samples each, results in another time series ("stack") with  $N$  bins. Each bin of the stack contains the sum of  $K$  samples. These  $K$  samples for bin # $n$  will have a mean  $M_n$  and they will have a standard deviation (rms)  $m_n$  that represents their white noise content. The variance of the  $n$ 'th bin

$$m_n^2 = \frac{1}{K-1} \sum_{k=1}^K (f_n(k) - M_n)^2$$

can be rewritten as a variance w.r.t. to a value A which is not the mean, using  $m^2(A) = m^2 + [K/(K-1)](M-A)^2$ :

$$m_n^2(M_k) = \frac{1}{K-1} \sum_{k=1}^K (f_k(n) - M_k)^2 = m_n^2 + \frac{K}{K-1} (M_n - M_k)^2$$

For a large number of sweeps  $m_n^2(M_k) \sim m_n^2 \sim m_k^2 \sim m_k^2(M_n)$ , i.e. a sweep should have the same mean and variance as a bin; or: time averaging should be equivalent to statistical averaging. Therefore the quantity

$$\chi^2(n) = \sum_{k=1}^K \left( \frac{f_k(n) - M_k}{m_k} \right)^2$$

represents the normalized variance of the stack, calculated from the measurements in any of the bins. It follows a  $\chi^2$  distribution (Kertz, 1978) which has the mean  $M(\chi^2) = k$  (and the variance  $m^2(\chi^2) = 2k$ ). The power of the sum (stack) of white noise measurements increases therefore proportional to the number of measurements. The power of a periodic signal, on the other hand, increases with the square of the number of measurements. As a consequence, the signal-amplitude to rms-noise ratio of a stacked time series increases with the square root of the number of sweeps that have been added into one stack.

## B. AN INTEGRAL EQUATION TECHNIQUE FOR SIMULATING ELECTROMAGNETIC INDUCTION IN TWO DIMENSIONS

The February 1971 issue of Geophysics (vol.36, no.1) was devoted to modeling the electric and magnetic fields produced by scatterers in a conductive earth in response to excitation by sources above the earth. An integral equation is solved for scattering currents due to the excess electrical conductivity in the anomaly. Weidelt (1975) summarized and derived solutions for a three-dimensional (conductivity varies in all three directions) inhomogeneity embedded in a one-dimensional (conductivity varies only with depth) earth. His solution has been modified in this appendix for a two dimensional inhomogeneity (conductivity does not change in  $y$ , the strike direction) by a Fourier transform in the strike direction. This results in a formulation that promises high computational efficiency and speed. The ~~only~~ other two-dimensional solution is based on a finite difference approach (Stoyer and Greenfield, 1976) *and* ~~which~~ has certain disadvantages for a moving source system as explained in chapter 2 of this thesis.

The parts of this appendix that cover the three-dimensional case are presented in detail because the reference (Schmucker and Weidelt, 1975) is not well accessible.

### B.1 VECTOR INTEGRAL EQUATION FOR THE ELECTRIC FIELD

In frequency domain, with negligible displacement currents and with source currents separated into inductive ( $\sigma \underline{E}$ ) and other ( $\underline{J}$ ) parts Ampere's law and Faraday's law

$$\underline{\nabla} \times \underline{H} = \sigma \underline{E} + \underline{J} \quad \text{and} \quad \underline{\nabla} \times \underline{E} = -i\omega\mu_0 \underline{H}$$

combine into a vector differential equation for the electric field

$$\underline{\nabla} \times \underline{\nabla} \times \underline{E} + \alpha^2 \underline{E} = -i\omega\mu_0 \underline{J} \quad \text{where} \quad \alpha^2 = i\omega\mu_0 \sigma. \quad (1)$$

The geophysical model of a layered conductive halfspace is defined by a certain "normal" conductivity structure  $\sigma_n(z)$  (figure B-1). Any source distribution in that halfspace will give rise to a "normal" electric field  $\underline{E}_n(x,y,z)$  that can be calculated with existing algorithms (e.g. Boerner, 1984). Introducing a scatterer

$$\sigma = \sigma_n(z) + \sigma_a(x,y,z) \quad (2)$$

into a region  $V_a$  of the normal conductivity structure will give rise to a scattered electric field  $\underline{E}_a$ :

$$\underline{E} = \underline{E}_n(x,y,z) + \underline{E}_a(x,y,z) \quad (3)$$

The electric field of a source current  $\underline{J}$  in the normal model is a solution of

$$\underline{\nabla} \times \underline{\nabla} \times \underline{E}_n + \alpha_n^2 \underline{E}_n = -i\omega\mu_0 \underline{J} \quad (4)$$

whereas the model with the scatterer is described by

$$\underline{\nabla} \times \underline{\nabla} \times (\underline{E}_n + \underline{E}_a) + (\alpha_n^2 + \alpha_a^2)(\underline{E}_n + \underline{E}_a) = -i\omega\mu_0 \underline{J} \quad (5)$$

Subtracting (4) from (5) yields a vector differential equation for the scattered electric field  $\underline{E}_a$

$$\underline{\nabla} \times \underline{\nabla} \times \underline{E}_a + \alpha_n^2 \underline{E}_a = -i\omega\mu_0 \sigma_a \underline{E} \quad (6)$$

that simulates the effect of the boundary of the scatterer by an inductive source current  $\sigma_a \underline{E}$  contained within the bounded volume  $V_a$ . Suppose the solution  $\underline{G}_i(\underline{r}', \underline{r})$  of

$$\underline{\nabla} \times \underline{\nabla} \times \underline{G}_i(\underline{r}', \underline{r}) + \alpha_n^2 \underline{G}_i(\underline{r}', \underline{r}) = \hat{\underline{x}}_i \delta(\underline{r}' - \underline{r}) \quad (7)$$



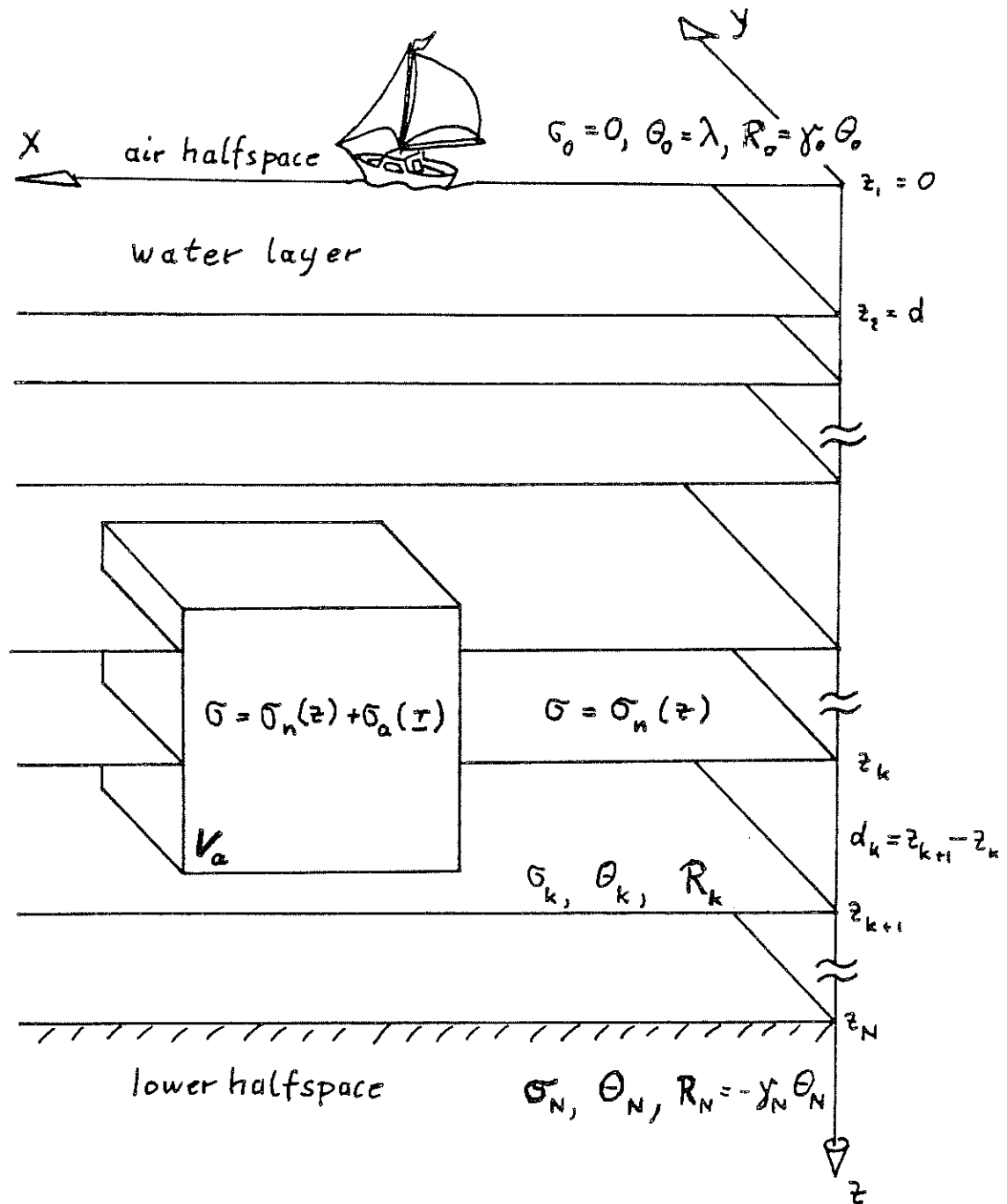


Figure B-1: Example for a scatterer of conductivity  $\sigma = \sigma_n(z) + \sigma_a(\underline{r})$  embedded within a normal conductivity structure  $\sigma_n(z)$ . The symbols included here define the numbering scheme: all quantities within one layer have the same index as the depth to the top of the layer.

that vanishes at infinity is known, where  $\underline{\hat{x}}_i$  is one of the unit vectors  $\underline{\hat{x}}, \underline{\hat{y}}, \underline{\hat{z}}$ . Multiplying (6) by the Green vector  $\underline{G}_i(\underline{r}', \underline{r})$  and (7) by the scattered electric field  $\underline{E}_a(\underline{r}')$  and integrating the difference over the whole space gives

$$\begin{aligned} & \iiint \underline{G}_i(\underline{r}', \underline{r}) \cdot \nabla \times \nabla \times \underline{E}_a(\underline{r}') - \underline{E}_a(\underline{r}') \cdot \nabla \times \nabla \times \underline{G}_i(\underline{r}', \underline{r}) \, d\underline{r}' \\ &= -\iiint \alpha_a^2(\underline{r}') \underline{G}_i(\underline{r}', \underline{r}) \cdot \underline{E}(\underline{r}') + \underline{\hat{x}}_i \cdot \underline{E}_a(\underline{r}) \delta(\underline{r}' - \underline{r}) \, d\underline{r}' \end{aligned}$$

Applying Green's vector theorem to the left hand side and observing that  $\underline{E}_a$  and  $\underline{G}_i$  vanish at infinity shows that the left hand side is zero. The second integral on the right hand side equals  $\underline{E}_{ai}(\underline{r})$  while the first integral need only be extended over the volume  $V_a$  of the scatterer because  $k_a^2(\underline{r}') = 0$  outside:

$$\underline{E}_{ai}(\underline{r}) = -\iiint_{V_a} \alpha_a^2(\underline{r}') \underline{G}_i(\underline{r}', \underline{r}) \cdot \underline{E}(\underline{r}') \, d\underline{r}' \quad (8)$$

After combining all three components and substituting  $\underline{E}_n = \underline{E}_a$ ,

$$\underline{E}(\underline{r}) + \iiint_{V_a} \alpha_a^2(\underline{r}') \underline{G}(\underline{r}', \underline{r}) \cdot \underline{E}(\underline{r}') \, d\underline{r}' = \underline{E}_n(\underline{r}) \quad (9)$$

where  $\underline{G}_i$  is the  $i$ 'th row of  $\underline{G}$  and  $\underline{G}(\underline{r}', \underline{r})$  is the dyadic Green function for the electric vector Helmholtz equation in a layered halfspace. (9) is a vector integral equation for the unknown total electric field  $\underline{E}$  within the volume  $V_a$  and has been used by Weidelt (1975) to derive an algorithm for three dimensional numerical modeling of magnetotelluric results. He divided the scatterer into a number of prisms such that the electric field within each cell can be assumed constant. The volume integral in (9) over the scatterer reduces then to a sum of integrals over single cells. The discrete equivalent of (9) is a linear inhomogeneous system of equations with the known normal electric field  $\underline{E}_n(\underline{r}_i)$  on the right hand side. The coefficient matrix contains products of the anomalous conductivity  $\sigma_a(\underline{r}_i)$  and Green functions  $\iiint \underline{G}_{ij}(\underline{r}_i, \underline{r}_j) \, d\underline{r}_i$  integrated over the  $i$ 'th cell.

A change in the source configuration affects only the right hand side and does not require a recomputation of the coefficient matrix. The cell-integrated Green functions need not be recomputed for a change in the conductivity of any cell (as long as a change in the size of the cell is not required); induced polarization is thus easily simulated as a frequency dependent complex conductivity according to the Cole-Cole formula (Pelton et al., 1978).

In a two dimensional earth conductivity is allowed to vary only in the  $x,z$  plane. The  $y'$  integration in the integral equation (9) becomes a convolution since the Green dyadic depends on  $y-y'$  whereas  $\underline{E}$  depends on  $y'$  alone and  $\alpha_a^2(x',z')$  can be taken in front of the  $y'$  integral. Hence a Fourier transformation in  $y'$  (appendix A) reduces the  $y'$  integration in (9) to a multiplication in the  $q$  wavenumber domain:

$$\underline{E}(x,z,q) + i\omega\mu_0 \iint_{S_a} \sigma_a(x',z') \underline{G}(x',z',x,z,q) \cdot \underline{E}(x',z',q) dx'dz' = \underline{E}_n(x,z,q) \quad (10)$$

where the volume  $V_a$  of the scatterer has been replaced by its cross sectional surface  $S_a$ .

## B.2 THE ELEMENTS OF THE GREEN DYADIC

The electric field  $\underline{E}$  away from sources or boundaries has only a divergence free (transverse) part  $\underline{\nabla} \times \underline{A}$  which can be represented (Morse and Feshbach, 1953, Chapter 13) by two scalar potentials so that the part of  $\underline{E}$  derived from the tangential electric (TE) potential  $\psi$  is tangential to planes  $z=z_m$  and the part of  $\underline{E}$  derived from the tangential magnetic (TM) potential  $\chi$  has a curl tangential to  $z=z_m$ :

$$\underline{E} = \underline{\nabla} \times (\underline{\hat{z}}\psi) + \underline{\nabla} \times \underline{\nabla} \times (\underline{\hat{z}}\chi) \quad (1)$$

Morse and Feshbach (1953) demonstrated that if any of the scalars satisfies the scalar Helmholtz equation then the part of the field derived from it is a solution to the vector Helmholtz equation. Hence for  $\underline{E}$  to satisfy the vector Helmholtz equation let

$$\nabla^2 \psi = -\alpha^2 \psi \quad (2), \quad \text{and} \quad \nabla^2 \chi = -\alpha^2 \chi \quad (3)$$

The potentials are suitable for the problem because for the divergence free electric field:  $\underline{\nabla} \times \underline{\nabla} \times \underline{E} = \nabla^2 \underline{E}$ , and equations B.1(1), B.1(4) - B.1(7) reduce to Helmholtz equations.

The electric and magnetic field components are in terms of these potentials:

$$\underline{E} = \begin{pmatrix} \frac{\partial \psi}{\partial y} + \frac{\partial^2 \chi}{\partial x \partial z} \\ -\frac{\partial \psi}{\partial x} + \frac{\partial^2 \chi}{\partial y \partial z} \\ -\left(\frac{\partial^2}{\partial x^2} + \frac{\partial^2}{\partial y^2}\right)\chi \end{pmatrix} \quad (4)$$

$$\begin{aligned} \underline{H} &= -\frac{1}{i\omega\mu_0} \underline{\nabla} \times \underline{E} = -\sigma \underline{\nabla} \times (\underline{\hat{z}}\chi) - \frac{1}{i\omega\mu_0} \underline{\nabla} \times \underline{\nabla} (\underline{\hat{z}}\psi) \\ &= \begin{pmatrix} -\sigma \frac{\partial \chi}{\partial y} - \frac{1}{i\omega\mu_0} \frac{\partial^2 \psi}{\partial x \partial z} \\ \sigma \frac{\partial \chi}{\partial x} - \frac{1}{i\omega\mu_0} \frac{\partial^2 \psi}{\partial y \partial z} \\ \left(\frac{\partial^2}{\partial x^2} + \frac{\partial^2}{\partial y^2}\right)\chi \end{pmatrix} \end{aligned} \quad (5)$$

The continuity of  $\underline{H}$  and the tangential  $\underline{E}$  at a horizontal boundary between the m'th and m+1'st layer requires

$$\underline{\hat{z}} \times (\underline{E}_m - \underline{E}_{m+1}) = 0 \quad (6a-6c), \quad \text{and} \quad \underline{H}_m - \underline{H}_{m+1} = 0 \quad (7a-7c)$$

Schmucker and Weidelt (1975) demonstrated how the boundary conditions for the potentials derive from (6) and (7): After substituting (5) into (7) it follows that

$$\left( \frac{\partial^2}{\partial x^2} + \frac{\partial^2}{\partial y^2} \right) (\psi_m - \psi_{m+1}) = 0.$$

The jump in  $\psi$  satisfies the two dimensional Laplace equation, is bounded and vanishes at infinity because of the finite extent of the sources. Hence, from Liouville's theorem it is zero. In other words  $\psi$  is continuous. Differentiating (7a) with respect to  $x$  and (7b) w.r.t.  $y$  and adding it follows along the same line that  $\partial\psi/\partial z$  is continuous. Differentiating (6a) w.r.t.  $x$  and (6b) w.r.t. to  $y$  and adding the continuity of  $\partial\chi/\partial z$  is obtained. Finally, differentiating (7a) w.r.t.  $y$  and (7b) w.r.t.  $x$  and subtracting gives the continuity of  $\partial\chi$ . In summary,

$$\psi, \frac{\partial\psi}{\partial z}, \partial\chi, \frac{\partial\chi}{\partial z} \quad \text{are continuous} \quad (8)$$

The aim is now to find the elements of the Green dyadic

$$\begin{aligned} \underline{\underline{G}}(\underline{r}', \underline{r}) &= \begin{pmatrix} G_x \\ G_y \\ G_z \end{pmatrix} = \begin{pmatrix} \nabla \times (\hat{z} \psi_x) + \nabla \times \nabla \times (\hat{z} \chi_x) \\ \nabla \times (\hat{z} \psi_y) + \nabla \times \nabla \times (\hat{z} \chi_y) \\ \nabla \times (\hat{z} \psi_z) + \nabla \times \nabla \times (\hat{z} \chi_z) \end{pmatrix} \\ &= \begin{pmatrix} \frac{\partial^2 \chi_x}{\partial x \partial z} + \frac{\partial \psi_x}{\partial y} & \frac{\partial^2 \chi_x}{\partial y \partial z} - \frac{\partial \psi_x}{\partial x} & -\left(\frac{\partial^2}{\partial x^2} + \frac{\partial^2}{\partial y^2}\right) \chi_x \\ \frac{\partial^2 \chi_y}{\partial x \partial z} + \frac{\partial \psi_y}{\partial y} & \frac{\partial^2 \chi_y}{\partial y \partial z} - \frac{\partial \psi_y}{\partial x} & -\left(\frac{\partial^2}{\partial x^2} + \frac{\partial^2}{\partial y^2}\right) \chi_y \\ \frac{\partial^2 \chi_z}{\partial x \partial z} & \frac{\partial^2 \chi_z}{\partial y \partial z} & -\left(\frac{\partial^2}{\partial x^2} + \frac{\partial^2}{\partial y^2}\right) \chi_z \end{pmatrix} \quad (9) \end{aligned}$$

that solves the Helmholtz equation obtained from B.1(7),

$$\nabla^2 \underline{G}_i(\underline{r}', \underline{r}) + \alpha_n^2 \underline{G}_i(\underline{r}', \underline{r}) = \hat{x}_i \delta(\underline{r}' - \underline{r}) \quad \text{where } i=x, y, z \quad (10)$$

with the boundary conditions (8) at  $z=z_m$ . The Green dyadic used to transform a source-dipole in an unbounded medium into an electric field is (Morse and Feshbach, 1953, chapter 13, p.1780):

$$G_{ij}(\underline{r}, \underline{r}') = \left( -\delta_{ij} \nabla^2 - \frac{\partial^2}{\partial x_i \partial x_j} \right) \frac{1}{\alpha^2} g(\underline{r}, \underline{r}')$$

where  $g(\underline{r}, \underline{r}') = -e^{i\alpha|\underline{r}-\underline{r}'|}/4\pi|\underline{r}-\underline{r}'|$  is the solution of the scalar Helmholtz equation  $\nabla^2 g + \alpha^2 g = \delta(\underline{r}-\underline{r}')$ . Therefore  $\nabla^2 g = -\alpha^2 g$  except at the singularity  $\underline{r}'$  and it follows that for  $\underline{r} \neq \underline{r}'$

$$G_{ij}(\underline{r}, \underline{r}') = \left( k^2 \delta_{ij} - \frac{\partial^2}{\partial x_i \partial x_j} \right) \frac{e^{i\alpha|\underline{r}-\underline{r}'|}}{4\pi\alpha^2|\underline{r}-\underline{r}'|} \quad (11)$$

Following Schmucker and Weidelt (1975) a comparison between (9) and (11) yields particular solutions for the six potentials  $\chi_i, \psi_i$  ( $i=x, y, z$ ): For  $i=z$  and since  $\partial/\partial z' = -\partial/\partial z$  (11) becomes

$$\underline{G}_z = \left( -\hat{z}\nabla^2 + \underline{\nabla} \frac{\partial}{\partial z} \right) \frac{e^{i\alpha|\underline{r}-\underline{r}'|}}{4\pi\alpha^2|\underline{r}-\underline{r}'|} = -\underline{\nabla} \times \underline{\nabla} \times \hat{z} \frac{e^{i\alpha|\underline{r}-\underline{r}'|}}{4\pi\alpha^2|\underline{r}-\underline{r}'|}$$

Comparing this with (10) shows that

$$\chi_z = - \frac{e^{i\alpha|\underline{r}-\underline{r}'|}}{4\pi\alpha^2|\underline{r}-\underline{r}'|} \quad (12) \quad \text{and} \quad \psi_z = 0. \quad (13)$$

With Sommerfeld's integral (12) is rewritten as

$$\chi_z = - \frac{1}{4\pi\alpha^2} \int_0^\infty \frac{\lambda}{\Theta} e^{-\Theta|z-z'|} J_0(\lambda r) d\lambda \quad (14)$$

$$\text{where} \quad r^2 = (x-x')^2 + (y-y')^2 \quad \text{and} \quad \Theta^2 = \alpha^2 + \lambda^2. \quad (15)$$

For  $i=x, j=z$ , using Sommerfeld's integral and the identity

$$\left( \frac{\partial^2}{\partial x^2} + \frac{\partial^2}{\partial y^2} \right) \left( \frac{\partial}{\partial x} J_0(\lambda r) \right) = -\lambda^2 \frac{\partial}{\partial x} J_0(\lambda r)$$

equation (11) becomes

$$G_{xz} = - \left( \frac{\partial^2}{\partial x^2} + \frac{\partial^2}{\partial y^2} \right) \frac{1}{4\pi\alpha^2} \frac{\partial}{\partial x} \int_0^\infty \frac{\text{sign}(z-z')}{\lambda} e^{-\Theta|z-z'|} J_0(\lambda r) d\lambda$$

and a comparison with (9) shows that

$$\chi_x = \frac{1}{4\pi\alpha^2} \frac{\partial}{\partial x} \int_0^\infty \frac{\text{sign}(z-z')}{\lambda} e^{-\Theta|z-z'|} J_0(\lambda r) d\lambda. \quad (16)$$

For  $i=x$ ,  $j=y$  and with Sommerfeld's integral (11) becomes

$$\begin{aligned} G_{xy} &= \frac{1}{4\pi\alpha^2} \frac{\partial^2}{\partial x \partial y} \int_0^\infty \left( \frac{\lambda}{\Theta} + \frac{\Theta}{\lambda} - \frac{\Theta}{\lambda} \right) e^{-\Theta|z-z'|} J_0(\lambda r) d\lambda \\ &= \frac{\partial^2}{\partial y \partial z} \chi_x + \frac{1}{4\pi} \frac{\partial^2}{\partial x \partial y} \int_0^\infty \frac{1}{\lambda \Theta} e^{-\Theta|z-z'|} J_0(\lambda r) d\lambda \end{aligned}$$

so that by comparison with (9)

$$\psi_x = - \frac{1}{4\pi} \frac{\partial}{\partial y} \int_0^\infty \frac{1}{\lambda \Theta} e^{-\Theta|z-z'|} J_0(\lambda r) d\lambda. \quad (17)$$

By symmetry,

$$\chi_y = \frac{1}{4\pi\alpha^2} \frac{\partial}{\partial y} \int_0^\infty \frac{\text{sign}(z-z')}{\lambda} e^{-\Theta|z-z'|} J_0(\lambda r) d\lambda \quad (18)$$

$$\psi_y = - \frac{1}{4\pi} \frac{\partial}{\partial x} \int_0^\infty \frac{1}{\lambda \Theta} e^{-\Theta|z-z'|} J_0(\lambda r) d\lambda. \quad (19)$$

The two dimensional integral equation B.1(11) requires the elements of  $G$  in the  $q$  wavenumber domain. On using (Oberhettinger, 1972)

$$\frac{1}{2\pi} \int_{-\infty}^{\infty} \int_{-\infty}^{\infty} f(\sqrt{p^2+q^2}) e^{i(px+qy)} dp dq = \int_0^\infty f(\lambda) J_0(\lambda r) \lambda d\lambda \quad (20)$$

with  $\lambda^2 = p^2 + q^2$  and  $r^2 = x^2 + y^2$ , the Fourier transforms B.1(10) of the particular solutions for the potentials (12) - (19) become:

$$\chi_x(x, z, q) = \int_{-\infty}^{\infty} \frac{ip \operatorname{sign}(z-z')}{2 \alpha^2 \lambda^2} e^{-\Theta|z-z'|} e^{ip(x-x')} dp \quad (21)$$

$$\chi_y(x, z, q) = \int_{-\infty}^{\infty} \frac{iq \operatorname{sign}(z-z')}{2 \alpha^2 \lambda^2} e^{-\Theta|z-z'|} e^{ip(x-x')} dp \quad (22)$$

$$\chi_z(x, z, q) = \int_{-\infty}^{\infty} \left( -\frac{1}{2 \alpha^2 \Theta} \right) e^{-\Theta|z-z'|} e^{ip(x-x')} dp \quad (23)$$

$$\psi_x(x, z, q) = \int_{-\infty}^{\infty} \left( -\frac{iq}{2 \lambda^2 \Theta} \right) e^{-\Theta|z-z'|} e^{ip(x-x')} dp \quad (24)$$

$$\psi_y(x, z, q) = \int_{-\infty}^{\infty} \left( -\frac{ip}{2 \lambda^2 \Theta} \right) e^{-\Theta|z-z'|} e^{ip(x-x')} dp \quad (25)$$

$$\psi_z(x, z, q) = 0 \quad (26)$$

where

$$\lambda^2 = p^2 + q^2 \quad \Theta^2 = \lambda^2 + \alpha^2 \quad \alpha^2 = i\omega\mu_0\sigma \quad (27)$$

The general solutions in the presence of horizontal boundaries at  $z=z_m$  are conveniently obtained by separating out the  $z$  dependence in the differential equations (3) and taking the two dimensional Fourier transform in the horizontal coordinates. The resulting equations are of the form

$$\frac{\partial^2}{\partial z^2} \Phi(p, q, z) = -\Theta^2 \Phi(p, q, z) \quad (28)$$

with a particular solution (compare to (21)-(26)):

$$\Phi(p, q, z) = e^{-\Theta|z-z'|} \quad (29)$$



The boundary conditions (8) for the potentials result in

$$\frac{1}{\varepsilon} \Phi \quad \text{and} \quad \frac{\gamma}{\varepsilon} \frac{\partial \Phi}{\partial z} \quad \text{continuous} \quad (30a)$$

where

$$\varepsilon = \begin{cases} 1 & \text{for } \chi_x, \chi_y \\ 0 & \text{for } \psi_x, \psi_y, \chi_z \end{cases} \quad \gamma = \begin{cases} \sigma & \text{for } \chi_x, \chi_y, \chi_z \\ 1 & \text{for } \psi_x, \psi_y \end{cases} \quad (30b,c)$$

General solutions for  $\Phi$  in layers may be obtained by fitting the coefficients of the upward and downward diffusing exponentials in

$$\Phi_n(p, q, z) = a_n^- e^{-\Theta_n(z-z_n)} + a_n^+ e^{+\Theta_n(z-z_n)} \quad (31)$$

to the boundary conditions and adding the resulting expressions to the particular solution (29). The general solutions for the transformed potentials may then be obtained by replacing  $e^{-\Theta|z-z'|}$  in (21) - (26) with the general solutions for  $\Phi$ . I followed this procedure for one layer (ocean) between an upper halfspace (air) and a lower halfspace (crust) and checked its consistency with a more elegant method of obtaining the general solution for  $\Phi$  in the N - layered earth as suggested by Dr. P. Weidelt (private communication) which will now be presented.

For more convenient writing let  $R_n(z)$  be an electromagnetic response function (Chave, 1982) for the TE mode or for the TM mode in the n'th layer (figure B-1):

$$R_n(z) = \frac{\gamma_n \Phi_n(z)}{\partial \Phi_n(z) / \partial z} \quad (32)$$

where  $\gamma$  as defined in (30c) separates TE and TM modes.  $R$  is continuous across horizontal boundaries  $z_n$  with no sources on them:

$$R_{n-1}(z_n) = R_n(z_n) \quad \text{for } z_n \neq z' \quad (33)$$

This does however not mean a loss of generality because every "source-layer" can be treated separately and the resulting fields added. The radiation conditions in the upper and lower half spaces require that

$$R_0(z_1) = \gamma_0 \Theta_0 \quad \text{and} \quad R_N(z_N) = -\gamma_N \Theta_N. \quad (34)$$

Starting from the upper and lower halfspaces  $R$  can be obtained at any layer boundary by use of the recursions which follow after combining (31), (32) and (33),

$$R_{n+1}(z_{n+1}) = \frac{\gamma_n}{\Theta_n} \frac{R_n(z_n) + \frac{\gamma_n}{\Theta_n} \tanh(\Theta_n d_n)}{\frac{\gamma_n}{\Theta_n} + R_n(z_n) \tanh(\Theta_n d_n)} \quad (35)$$

$$R_n(z_n) = \frac{\gamma_n}{\Theta_n} \frac{R_{n+1}(z_{n+1}) - \frac{\gamma_n}{\Theta_n} \tanh(\Theta_n d_n)}{\frac{\gamma_n}{\Theta_n} - R_{n+1}(z_{n+1}) \tanh(\Theta_n d_n)} \quad (36)$$

if no levels  $z=z'$  with singularities in  $g(\underline{r}', \underline{r})$  have been crossed.  $R$  can be obtained anywhere in the stack when introducing "artificial" layer boundaries with no change in the electrical conductivity. This is a valid procedure because the recursions (35) and (36) are associative across such artificial boundaries  $z=z_a$ : It is easy to show that one step from  $z_n$  to  $z_{n+1}$  gives the same  $R_{n+1}(z_{n+1})$  as two steps from  $z_n$  to  $z_a$  to  $z_{n+1}$ . The same is true when going from  $z_{n+1}$  to  $z_n$  for obtaining  $R_n(z_n)$ .

The auxiliary functions  $\Phi_s(z')$  and  $\Phi_{s-1}(z')$  at the singularity level  $z=z'$  can now be determined from the upper and lower stack response functions as propagated onto the singularity level. Combining (29) and (32) and differentiating with respect to  $z$ , the system of equations

$$\Phi_{s-1}(z') - \Phi_s(z') = 0 \quad (37a)$$

$$\left. \frac{\partial \Phi_{s-1}}{\partial z} \right|_{z'} - \left. \frac{\partial \Phi_s}{\partial z} \right|_{z'} = 2 \Theta_s \quad (37b)$$

$$R_{s-1}(z') \left. \frac{\partial \Phi_{s-1}}{\partial z} \right|_{z'} - \gamma_{s-1} \Phi_{s-1}(z') = 0 \quad (37c)$$

$$R_s(z') \left. \frac{\partial \Phi_s}{\partial z} \right|_{z'} - \gamma_s \Phi_s(z') = 0 \quad (37d)$$

is obtained with the solutions

$$\Phi_s(z') = \frac{2\Theta_s}{\gamma_s} \frac{R_s(z') R_{s-1}(z')}{R_s(z') - R_{s-1}(z')} \quad (38a)$$

$$\Phi_{s-1}(z') = \Phi_s(z') \quad (38b)$$

$$\left. \frac{\partial \Phi_s}{\partial z} \right|_{z'} = 2\Theta_s \frac{R_{s-1}(z')}{R_s(z') - R_{s-1}(z')} \quad (38c)$$

$$\left. \frac{\partial \Phi_{s-1}}{\partial z} \right|_{z'} = 2\Theta_s \frac{R_s(z')}{R_s(z') - R_{s-1}(z')} \quad (38d)$$

The recursions away from the singularity level as derived from (30), (32) and (35), (36),

$$\Phi_{n+1}(z_{n+1}) = \frac{\epsilon_{n+1}}{\epsilon_n} \Phi_n(z_n) \frac{1 - \frac{\gamma_n/\Theta_n}{R_n(z_n)}}{1 - \frac{\gamma_n/\Theta_n}{R_{n+1}(z_{n+1})}} e^{-\Theta_n d_n} \quad (39)$$

$$\Phi_n(z_n) = \frac{\epsilon_n}{\epsilon_{n+1}} \Phi_{n+1}(z_{n+1}) \frac{1 + \frac{\gamma_n/\Theta_n}{R_{n+1}(z_{n+1})}}{1 + \frac{\gamma_n/\Theta_n}{R_n(z_n)}} e^{-\Theta_n d_n} \quad (40)$$

allow the computation of  $\Phi$  anywhere in the stack when started with  $\Phi_s(z')$  according to (38a) and when artificial layer boundaries have been included. Similarly, the easily derived recursions

$$\left. \frac{\partial \Phi_{n+1}}{\partial z} \right|_{z_{n+1}} = \frac{\gamma_n \epsilon_{n+1}}{\gamma_{n+1} \epsilon_n} \left. \frac{\partial \Phi_n}{\partial z} \right|_{z_n} \frac{1 + \frac{\gamma_n/\Theta_n}{R_n(z_n)}}{1 + \frac{\gamma_n/\Theta_n}{R_{n+1}(z_{n+1})}} e^{-\Theta_n d_n} \quad (41)$$

$$\left. \frac{\partial \Phi_n}{\partial z} \right|_{z_n} = \frac{\gamma_{n+1} \epsilon_n}{\gamma_n \epsilon_{n+1}} \left. \frac{\partial \Phi_{n+1}}{\partial z} \right|_{z_{n+1}} \frac{1 - \frac{\gamma_n / \Theta_n}{R_{n+1}(z_{n+1})}}{1 - \frac{\gamma_n / \Theta_n}{R_n(z_n)}} e^{-\Theta_n d_n} \quad (42)$$

can be used in conjunction with (38c,d) to find the derivatives anywhere in the stack.

The use of only one auxiliary function  $\Phi$  and one response function  $R$  simplifies the algebra. In practice it is however necessary to evaluate two response functions for TM and TE modes, respectively, and three auxiliary functions as indicated by the choices (30b,c) of  $\gamma$  and  $\epsilon$  in (39) - (42). This becomes clear in the following conclusion:

After replacing  $e^{-\Theta|z-z'|}$  in (21) - (26) with the general solutions for  $\Phi(p,q,z,z')$  and substituting the resulting expressions into (9) the following general solutions for the elements of the Green dyadic in the  $q$  wavenumber domain  $G_{ij}^q(x,x',z,z',q)$  are obtained:

$$G_{xx}^q = \frac{1}{2} \int_{-\infty}^{\infty} \left( - \frac{p^2 \text{sign}(z-z')}{\alpha^2 \lambda^2} \frac{\partial \Phi_r^M}{\partial z} + \frac{q^2}{\lambda^2 \Theta} \Phi_r^E \right) e^{ip(x-x')} dp \quad (43a)$$

$$G_{xy}^q = \frac{1}{2} \int_{-\infty}^{\infty} \left( - \frac{pq \text{sign}(z-z')}{\alpha^2 \lambda^2} \frac{\partial \Phi_r^M}{\partial z} + \frac{pq}{\lambda^2 \Theta} \Phi_r^E \right) e^{ip(x-x')} dp \quad (43b)$$

$$G_{xz}^q = \frac{1}{2} \int_{-\infty}^{\infty} \left( \frac{ip \text{sign}(z-z')}{\alpha^2} \Phi_r^M \right) e^{ip(x-x')} dp \quad (43c)$$

$$G_{yx}^q = \frac{1}{2} \int_{-\infty}^{\infty} \left( - \frac{pq \text{sign}(z-z')}{\alpha^2 \lambda^2} \frac{\partial \Phi_r^M}{\partial z} + \frac{pq}{\lambda^2 \Theta} \Phi_r^E \right) e^{ip(x-x')} dp \quad (43d)$$

$$G_{yy}^q = \frac{1}{2} \int_{-\infty}^{\infty} \left( - \frac{q^2 \text{sign}(z-z')}{\alpha^2 \lambda^2} \frac{\partial \Phi_r^M}{\partial z} - \frac{p^2}{\lambda^2 \Theta} \Phi_r^E \right) e^{ip(x-x')} dp \quad (43e)$$

$$G_{yz}^q = \frac{1}{2} \int_{-\infty}^{\infty} \left( \frac{iq \text{sign}(z-z')}{\alpha^2} \Phi_r^M \right) e^{ip(x-x')} dp \quad (43f)$$

$$G_{zx} = \frac{1}{2} \int_{-\infty}^{\infty} \left( -\frac{ip}{\alpha^2 \Theta} \frac{\partial \Phi_z^M}{\partial z} \right) e^{ip(x-x')} dp \quad (43g)$$

$$G_{zy} = \frac{1}{2} \int_{-\infty}^{\infty} \left( -\frac{iq}{\alpha^2 \Theta} \frac{\partial \Phi_z^M}{\partial z} \right) e^{ip(x-x')} dp \quad (43h)$$

$$G_{zz} = \frac{1}{2} \int_{-\infty}^{\infty} \left( -\frac{\lambda^2}{\alpha^2 \Theta} \Phi_z^M \right) e^{ip(x-x')} dp \quad (43i)$$

where  $\Phi_r^M$ ,  $\Phi_z^M$ ,  $\Phi_r^E$  are the auxiliary functions that were determined in (39) - (42) in order to obtain the TM potentials  $\chi_x$ ,  $\chi_y$ ,  $\chi_z$  and the TE potentials  $\psi_x$ ,  $\psi_y$ . Three  $\Phi$ 's were sufficient because there is no distinction between the two horizontal components in (30b,c) as far as  $\Phi$  is concerned.

### B.3 ELECTRIC AND MAGNETIC FIELDS

The total electric field  $\underline{E}(\underline{r}')$  within the scatterer  $V_a$  will be known after solving the integral equation B.1(9). The same equation can now be used to evaluate  $\underline{E}(\underline{r})$  at any desired point  $\underline{r}$  when substituting the solution  $\underline{E}(\underline{r}')$  back into the integrand and evaluating  $\underline{G}(\underline{r}', \underline{r})$  at the additional points  $\underline{r}$ :

$$\underline{E}(\underline{r}) = \underline{E}_n(\underline{r}) - \iiint_{V_a} \underline{G}(\underline{r}', \underline{r}) \alpha_a^2(\underline{r}') \underline{E}(\underline{r}') d\underline{r}' \quad (1)$$

By the same argument and on using Faraday's law,  $\underline{B} = -\nabla \times \underline{E} / i\omega$ , the magnetic induction can be obtained:

$$\underline{B}(\underline{r}) = \underline{B}_n(\underline{r}) - \mu_0 \iiint_{V_a} \nabla \times \underline{G}(\underline{r}', \underline{r}) \sigma_a(\underline{r}') \underline{E}(\underline{r}') d\underline{r}' \quad (2)$$

where the curl operates on the unprimed coordinates and

$$\nabla \times \underline{G} = \hat{x} \left( \frac{\partial G_z}{\partial y} - \frac{\partial G_y}{\partial z} \right) + \hat{y} \left( \frac{\partial G_x}{\partial z} - \frac{\partial G_z}{\partial x} \right) + \hat{z} \left( \frac{\partial G_y}{\partial x} - \frac{\partial G_x}{\partial y} \right)$$

$$= \begin{pmatrix} \frac{\partial G_{zx}}{\partial y} - \frac{\partial G_{yx}}{\partial z} & \frac{\partial G_{zy}}{\partial y} - \frac{\partial G_{yy}}{\partial z} & \frac{\partial G_{zz}}{\partial y} - \frac{\partial G_{yz}}{\partial z} \\ \frac{\partial G_{xx}}{\partial z} - \frac{\partial G_{zx}}{\partial x} & \frac{\partial G_{xy}}{\partial z} - \frac{\partial G_{zy}}{\partial x} & \frac{\partial G_{xz}}{\partial z} - \frac{\partial G_{zz}}{\partial x} \\ \frac{\partial G_{yx}}{\partial x} - \frac{\partial G_{xx}}{\partial y} & \frac{\partial G_{yy}}{\partial x} - \frac{\partial G_{xy}}{\partial y} & \frac{\partial G_{yz}}{\partial x} - \frac{\partial G_{xz}}{\partial y} \end{pmatrix} \quad (3)$$

With B.2(43) the elements of  $\nabla \times \underline{G}$  in (3) can be written as inverse Fourier transforms:

$$(\nabla \times \underline{G})_{ij} = \frac{1}{2} \int_{-\infty}^{\infty} \tilde{C}_{ij}(x', x, z', z, q) e^{ip(x-x')} dp \quad (4)$$

with the integrands:

$$\tilde{C}_{xx} = \frac{p q}{\alpha^2 \Theta} \frac{\partial \Phi_z^M}{\partial z} + \frac{p q \Theta^2 \text{sign}(z-z')}{\alpha^2 \lambda^2} \Phi_r^M - \frac{p q}{\lambda^2 \Theta} \frac{\partial \Phi_r^E}{\partial z} \quad (4a)$$

$$\tilde{C}_{xy} = \frac{q^2}{\alpha^2 \Theta} \frac{\partial \Phi_z^M}{\partial z} + \frac{q^2 \Theta^2 \text{sign}(z-z')}{\alpha^2 \lambda^2} \Phi_r^M + \frac{p^2}{\lambda^2 \Theta} \frac{\partial \Phi_r^E}{\partial z} \quad (4b)$$

$$\tilde{C}_{xz} = -\frac{i q \lambda^2}{\alpha^2 \Theta} \Phi_z^M - \frac{i q \text{sign}(z-z')}{\alpha^2} \frac{\partial \Phi_r^M}{\partial z} \quad (4c)$$

$$\tilde{C}_{yx} = -\frac{p^2}{\alpha^2 \Theta} \frac{\partial \Phi_z^M}{\partial z} - \frac{p^2 \Theta^2 \text{sign}(z-z')}{\alpha^2 \lambda^2} \Phi_r^M + \frac{q^2}{\lambda^2 \Theta} \frac{\partial \Phi_r^E}{\partial z} \quad (4d)$$

$$\tilde{C}_{yy} = -\frac{p q}{\alpha^2 \Theta} \frac{\partial \Phi_z^M}{\partial z} - \frac{p q \Theta^2 \text{sign}(z-z')}{\alpha^2 \lambda^2} \Phi_r^M - \frac{p q}{\lambda^2 \Theta} \frac{\partial \Phi_r^E}{\partial z} \quad (4e)$$

$$\tilde{C}_{zx} = \frac{i p \lambda^2}{\alpha^2 \Theta} \Phi_z^M + \frac{i p \text{sign}(z-z')}{\alpha^2} \frac{\partial \Phi_r^M}{\partial z} \quad (4f)$$

$$\tilde{C}_{zx} = \frac{i q (p^2 - q^2)}{\lambda^2 \Theta} \Phi_r^E \quad (4g)$$

$$\tilde{C}_{zy} = -\frac{i p (p^2 - q^2)}{\lambda^2 \Theta} \Phi_r^E \quad (4h)$$

$$\tilde{C}_{zz} = 0 \quad (4i)$$